The development of petaled molybdenum disulfide as a versatile and sustainable electrocatalyst for alternative energy technologies.

By

Shane Thomas Finn

Dissertation

Submitted to the Faculty of the

Graduate School of Vanderbilt University

in partial fulfillment of the requirements

for the degree of

DOCTOR OF PHILOSOPHY

in

Chemistry

May, 2017

Nashville, Tennessee

Approved:

Janet E. Macdonald, Ph.D.

David E. Cliffel, Ph.D.

Nathan D. Schley, Ph.D.

Kirill I. Bolotin, Ph.D.

For my son, Elijah Thomas Finn.

You're my greatest achievement, and I can't even take full credit for you.

TABLE OF CONTENTS

Appendix

LIST OF TABLES

LIST OF FIGURES

CHAPTER I

Introduction

Figure 1. Global map of deviation from 1951-1980 average temperatures for the year 2015.[1]

The Problems

Our world is plagued by problems such as global climate change and poverty. Although global poverty

has been on the decline for the past two centuries due to increasing economic growth and despite a growing

population,[2] there are still roughly 750 million people living in extreme poverty (on <1.90 international-$/day).[3]

Thus, further progress needs to be made on this front, as The World Bank has declared a goal of ending extreme

poverty by 2030.[4]

Global climate change is a result of using fossil (*e.g.* crude oil, coal, natural gas) and other hydrocarbon-based (*e.g.* biomass) fuels as an energy source. Beside the finite supply of fossil fuels, burning hydrocarbons produces carbon dioxide (CO_2) and nitrous oxide (N_2O), among others, which are greenhouse gases that contribute to increasing global temperatures (2015 is the hottest year to date, as seen in Figures 1 & 2).[1] This warming affects and disrupts natural environments, fauna, and agriculture. Also, the release of hazardous byproducts such as perfluorocarbons and particulate matter puts a significant strain on human health, resulting in increased healthcare costs and infant mortality, to name two metrics.[5]
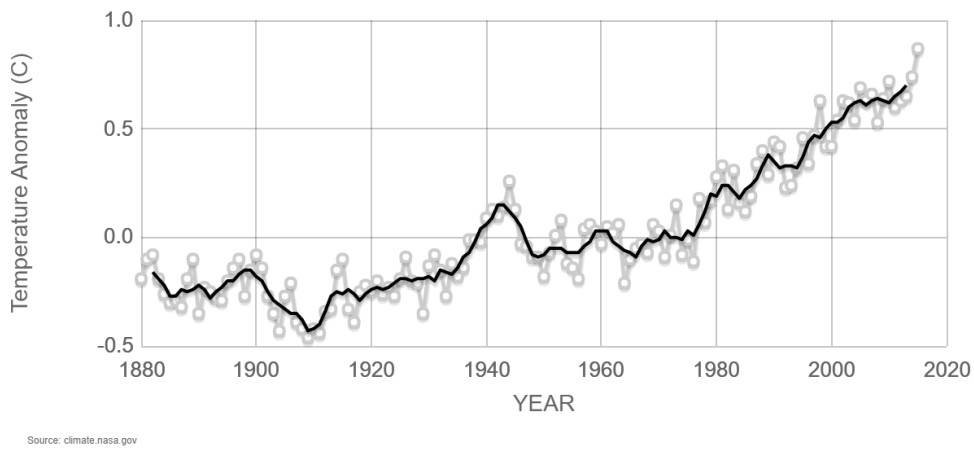
Figure 2. Deviation from 1951-1980 average temperatures (in °C) from 1884-2015: annual mean (grey points) and 5-year mean (black line).[1]

Oil has been a major source of global conflict for over a century, leading to wars between governments in developing as well as developed countries.[6] War destroys lives, infrastructure, and businesses and leads to poverty as a result of homelessness and emigration. Using abundant, renewable resources and thus decreasing scarcity will incite less conflict, cause less destruction, and support more stable economies. Beyond the roles that war, economy, mental illness, and governmental policy play in poverty, access to clean energy, or "energy poverty," is a significant metric for evaluating the progress of developing countries.[7] The largest current source of energy poverty is a lack of access to clean cooking facilities that do not require the use of biomass as fuel.[7]

Sustainable and inexpensive alternative energy technologies must be developed to reverse and diminish the effects of burning fossil fuels as well as increase the availability of clean energy options for impoverished people worldwide.

The Solution?

The Role of Science

The burden to alleviate the global energy crisis is placed on Science, our society's chief means of solving problems, to produce new technology, which is a particular solution to a specific problem. To effectively solve this energy crisis, the final product technologies must maximize efficiency to justify their existence and increase benefit over cost. Sustainability, the rule-of-thumb approach to environmental health problems, must also be maximiz. Environmental health encompasses everything on the earth and affects future generations. This means that the cost, waste, and the effect of the waste on the environment (toxicity) must also be minimized. Concordantly, as scientists observe, hypothesize, and experiment, they should incorporate sustainability at every step so that the final product will meet those standards of efficiency and sustainability. One caveat to this is that sometimes it is important to perform a more expensive or less sustainable experiment for the sake of increasing fundamental knowledge, which – when disseminated – is timeless, priceless and will benefit future generations.

The U.S. Department of Energy (DOE) has set a goal for renewable hydrogen fuels to be produced at a monetary cost less than or equal to the gas gallon equivalent (gge), specifically \$4/gge.[8] Because one gallon of gas contains a finite amount of energy, 32.9 kWh,[9] this figure can be converted to set a reasonable goal of 12 ¢/(kWh) (Figure 3) for not just hydrogen fuel, but any other alternative energy source as well.

Featured in Figure 3 is the levelized cost of energy (LCOE) for several major energy generation sources in the past six years (2014 is the latest available data).[10–28] LCOE is a calculation which compares the cost of varying energy technologies. For the calculated data in Figure 3, real data are used from reports and outlooks published by various energy organizations including the Office of Energy Efficiency & Renewable Energy (DOE) and the International Energy Agency (IEA), among many others.[29] LCOE values are normalized using one discount rate and lifetime of the technology across the board, while the other normalization factors (default capacity factor and value of depreciation) vary by generation source.
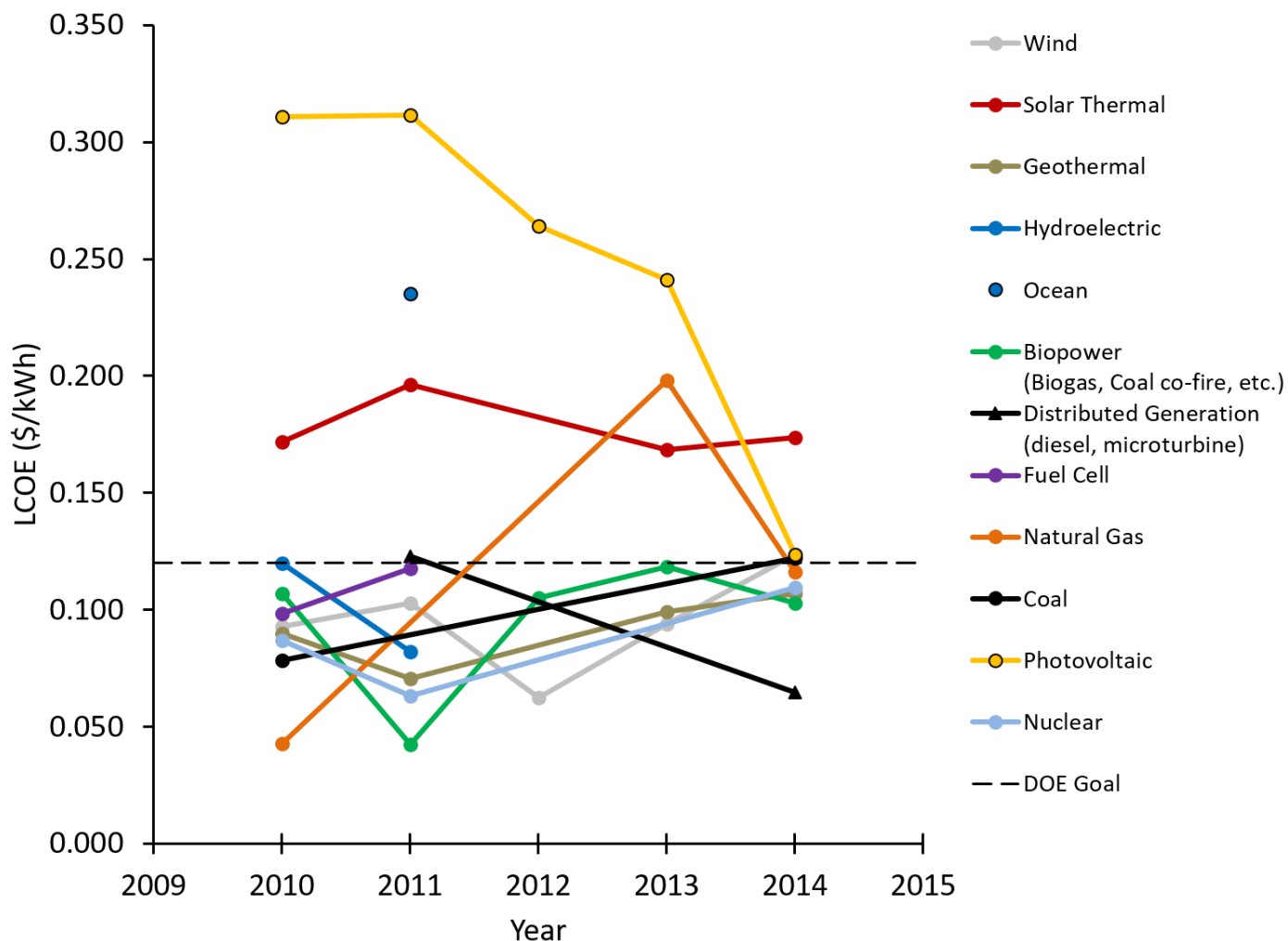
Figure 3. Levelized Cost of Energy (LCOE) for several major energy sources from 2010 - 2014.[12] Parameters: 7% discount rate, 30 years lifetime.

The LCOE of solar photovoltaic generation has decreased since 2011 and fell sharply from 2013 – 2014 to right above the 12 c/(kWh) viability goal. Interestingly, most generation sources in this calculation fall into a tight group in 2014 from 10-12 c/(kWh), showing that alternative energy technologies are indeed competitive with carbon combustion technologies. Even fuel cells, which represent a real-world application of water splitting, are just below the viability threshold as of 2011. Current fuel cell research efforts are directed towards decreasing operating temperature,[30–32] which is expected the drive the LCOE even lower.

What is not shown here is the capacity factor, which is the ratio of average power output to peak power output. Due to the inherent intermittency of the sun (day and night, winter, cloud cover, etc.), solar power conversion technologies are somewhat limited in their capacity factor (currently, 16%)[12] even if their power conversion efficiencies can be increased to unity. On the other hand, nearly every other generation source has a higher capacity factor, with geothermal and fuel cells leading at 95%.

Justification for Approach of the Present Work

Introducing Nanomaterials Chemistry

Solving energy problems with science requires the use of many materials (both well-known and yet-to-be-discovered) as well as consideration of their interactions with other materials. This requirement leads naturally to the field of chemistry. Chemistry offers unique insight into periodic properties of elements, bonding, compatibility, phases (solid, liquid, gas), phase structure (crystal structure in solids), epitaxy, absolute energy positions of highest-occupied and lowest-unoccupied molecular orbitals (HOMO/LUMO) as well as conduction and valence bands of bulk materials with optimal alignment. Therefore, chemistry is a very useful approach to the energy problem. In this dissertation, I focus on inorganic materials: mostly transition metals and chalcogenides.[33]

Beyond fundamental chemical characteristics, developing new technologies requires consideration of the dynamic interaction of higher-order (bulk) materials with atoms, molecules, and ions and across different phases (heterogeneous catalysis). Thus, this marriage of chemistry with larger-scale interactions yields the field of catalytic nanomaterials chemistry.

Now, considering the field of catalytic nanomaterials chemistry, the selection of elements must be narrowed down to the most earth-abundant and non-toxic materials for the sake of maximizing sustainability. Then, the effect and need of nanostructuring must be evaluated. Most commonly, nanostructuring of a material is used to increase the surface area-to-volume ratio, which ultimately minimizes the weight and volume of material needed while maximizing the area available for catalytic reactions. Since the 1980s, nanostructuring has used to confine materials, in at least one dimension, below the Bohr exciton radius to exploit its quantum confinement effects.[34,35] Furthermore, nanostructuring allows for isolating the specific facet(s) of a crystal structure which are ideal for the desired application.

Enter MoS$_2$

Briefly, MoS$_2$ (the subject of this dissertation) has greatly benefitted from the birth of nanoscience. MoS$_2$ is an abundant and inexpensive material that is interesting due to its layered crystal structure which yields anisotropic conductivity[36] and facile exfoliation of single layers,[37] and functionality as a solid-state lubricant.[38] The electronic structure of MoS$_2$ provides electrochemical stability as a cathode because the valence and conduction bands are seated in relatively non-bonding orbitals, dominated by Mo 4d character.[36] When a current is passed through MoS$_2$, its bonding character is not expected to be greatly altered.[39] As a testament to the electronic structure, MoS$_2$ has shown remarkable stability under both photooxidative[40] and electrochemically reductive conditions.[41]

The unique crystal structure of MoS$_2$ can be exploited to optimize its catalytic properties. MoS$_2$ has a layered, hexagonal crystalline structure (**Figure 4**). Sulfurs form pairs of close-packed layers with Mo atoms sandwiched between them, forming a trilayer, and each MoS$_2$ trilayer is separated by a van der Waals gap. It has been found that coordinately unsaturated crystallite edge sites of MoS$_2$, where Mo is exposed – not the S-

terminated faces – are the catalytic sites for HDS[42,43] and electrochemical HER.[44] Thus, maximizing the relative number of edge sites to facial sites has been shown to improve activity in electrochemical cells[45,46] and HDS catalyst designs.[42]
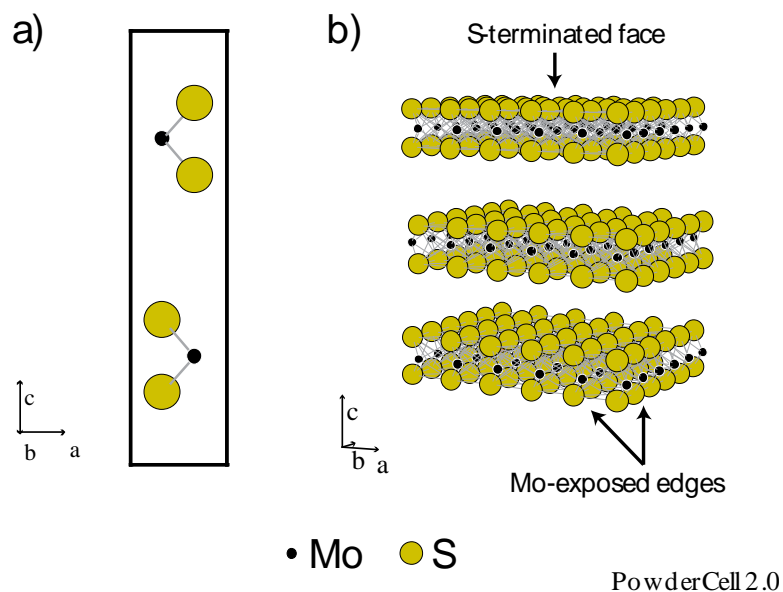
Figure 4. Crystal structure of MoS_2: a) unit cell observed along the <010> axis; b) several MoS_2 layers with Mo-exposed edges and S-terminated faces labeled.

Electrons preferentially conduct in-plane (a-, b-direction) and not through-plane (c-direction) in MoS_2.[47] Grain boundaries are also conducting,[44] and energy states arising from surface defects (such as edges, corners, and steps) positively influence catalysis.[48] MoS_2 was investigated in the 1990s as a cathode material for polysulfide reduction but gave disappointingly low activity. This was most likely due to the material being produced in a planar fashion.[41] Thus, an ideal electrocatalyst should also incorporate a directionality of the MoS_2 crystallites normal to a surface to promote conduction.

MoS_2 is still very intriguing to researchers around the world, and it is not likely to attract any fewer researchers in years to come. Figure 5 shows the results of a Web of Science™ search for MoS_2, and the results are plotted as number of records and corresponding percentage of records as a function of publication year. The number of reports on MoS_2 has been on a steep increase since 2010 (2 years prior to the beginning of my work

on this dissertation). This increase in the annual number of MoS_2 reports may have waned slightly in 2015, but apparently has not plateaued yet.
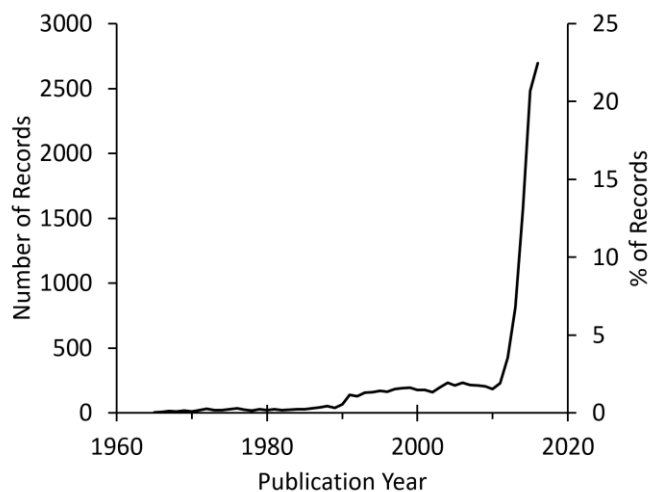
Figure 5. Thompson Reuters™ Web of Science™ search results for topic: MoS_2 OR topic: molybdenum disulfide OR topic: molybdenum(IV) sulfide. Top 500 results, minimum record count: 1. As of 11/21/2016.

Techniques

Beyond optimizing the aforementioned design parameters (material choice and nanostructure) to achieve harmony for the desired applications, the development of nanomaterials for alternative energy applications requires synthesis, characterization, and testing. Each of these three steps require a host of tools and techniques, which will be introduced below. With most techniques, there is often a tradeoff between frugality of deposition conditions (vacuum, inert atmosphere, voltage, temperature) and level of control.

Synthesis and processing types utilized in this dissertation include solvothermal, which essentially is heating a solvent, and hydrothermal, where the solvent is specifically water. The solvothermal approach has been used in high-temperature preparations of nanoparticles in organic solvents, which support the controlled nucleation and growth of crystals in the nanometer regime using coordinating ligands.[34,49–52] However, hydrothermal syntheses are favorable to organic solvothermal approaches, as water is more abundant and less costly than organic solvents (e.g., octadecene, oleylamine). While hydrothermal syntheses require no more than heating water with reagents to precipitate a product, sealed reaction vessels are typically used to heat the solution above the boiling point of water, creating a high-pressure environment which often produces unique, hierarchical structures and is very accommodating to the design of nanomaterials.[33,53–58] One tradeoff of hydrothermal synthesis is a generally decreased amount of control over final product crystal structure.

Deposition is another very useful tool in nanomaterials synthesis, especially in the preparation of electrode films. There are three major methods of deposition used in this work: electrodeposition, evaporation-assisted deposition, and chemical deposition. These deposition techniques offer varying degrees of control, from conformal coatings to atomically smooth deposits of a desired material. Electrodeposition includes electroplating and electrophoretic deposition, and is simply applying a controlled potential or electrical current to a conductive substrate of interest. This application of current or potential results in reduction (most common) or oxidation of solvated species, immobilizing them on the electrode surface. Electrophoretic deposition (EPD) is often used to deposit nanoparticles onto a TiO_2 or ZnO electrode and is a somewhat more complicated matter; the polarity (+ or -) and magnitude of potential used will depend on the particles to be deposited. Evaporation-assisted deposition requires vacuum conditions and the target material is evaporated either by heat (thermal) or by electrons (e-beam). Evaporation yields a very high degree of control, often to less than a nanometer. Lastly, chemical deposition operates on the principles of known chemical reactions. Chemical bath deposition involves

cooling reactants down considerably in order to slow the reaction and provide a moderate level of control over the resulting film thickness. Successive ionic layer adsorption and reaction (SILAR) consists of sequentially precipitating a desired material onto a substrate by dipping it in a solution of the desired cation, then the anion, and repeating.

Characterization

A few characterization techniques are indispensable to the nanomaterials chemist in the following general areas: electron microscopy, absorbance/fluorescence/Raman spectroscopy, and X-ray characterization techniques. Electron microscopy primarily includes scanning and transmission electron microscopy (SEM and TEM, respectively), with some intermediate and special modes such as backscattering (sub-surface information), scanning transmission electron microscopy (STEM), and the very useful energy-dispersive X-ray spectroscopy (EDS), which provides compositional information by measuring characteristic elemental X-rays emitted from the sample. SEM provides surface morphology and tends to be used in larger size regimes while TEM generally provides images of "translucent" particles (depending on size and MW) yielding crystalline lattice spacing and is used for few-nanometer size particles. UV-Visible absorbance and fluorescence spectroscopies, along with Raman spectroscopy, can offer a quick check as to the size of certain nanoparticles, their band gap, purity, size dispersity,[34] and identity. X-ray diffraction (XRD) is a complementary or substitutional technique to TEM (when particle sizes are much larger) and provides information about crystallinity, specific crystal structure, average grain size, and preferred orientation of materials. X-ray Photoelectron Spectroscopy (XPS) is a surface-sensitive technique which uses X-rays to excite electrons and emit them from the sample; the energy of the emitted photon is element- and oxidation state-dependent.

Electrochemistry stands in the gap between characterization and performance testing. Most often, it is used to measure the effectiveness and stability of a material to transfer electrons to or from an electrolyte solution of interest, as in cyclic voltammetry (CV), linear sweep voltammetry (LSV), and chrono-amperometry or -potentiometry. Also, electrochemistry can be used to measure electronic properties of the electrode itself utilizing alternating-current (AC) impedance techniques.

Perhaps performance testing in the academic laboratory is not as extensive as in the industrial laboratory, which is closer to the production of commercial devices. However, a high degree of engineering and optimization is required for testing of novel materials incorporated into devices, such that it can dominate or become the rate-limiting step in the completion of a Ph.D., among other things. Also, new device architectures which do not exist commercially are often attempted by researchers and this makes for lengthy, repeated experimentation.
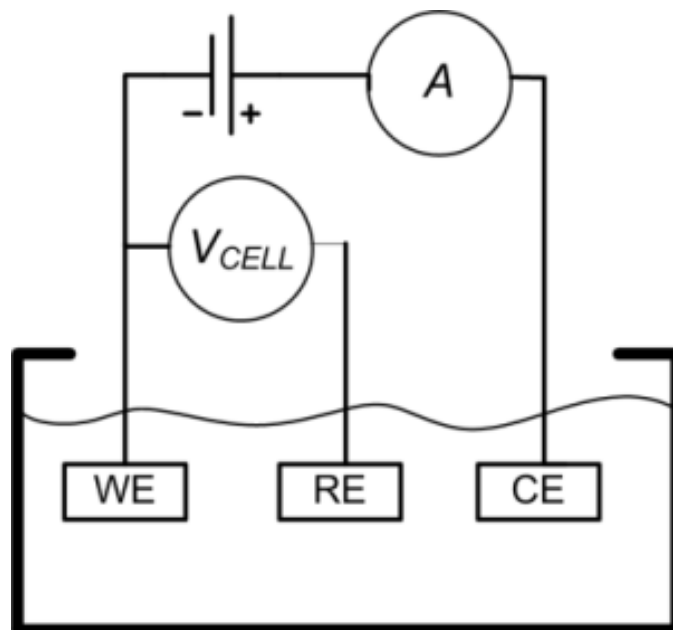
Figure 6. Diagram of a 3-electrode cell, including a working electrode (WE), reference electrode (RE), and a counter electrode (CE) submerged in an electrolyte solution. This image is used with permission from Punter, J.; Colomer-Farrarons, J.; Ll., P. Bioelectronics for Amperometric Biosensors. In *State of the Art in Biosensors - General Aspects*; InTech, 2013.[59]

Using the example of a solar cell, the electrochemical properties of a single electrode in question can be isolated using a 3-electrode cell, as depicted in Figure 5. This isolation of the desired electrode (used as WE) is possible because the potential is set or measured with respect to a standard RE, while the CE is excluded, and provides additional current as needed to support the WE-RE potential. For the photo-anode or -cathode, a photoelectrochemical cell may be employed, which consists of an illuminated 3-electrode cell. Once the photoelectrode is optimized, it can be incorporated into a discrete, sealed device with a counter electrode and electrolyte (liquid- or solid-state) and tested as such, similar to a commercial device (see Chapter II, Figure 1). This holds true for studies in energy storage, *e.g.* lithium-ion batteries (LIBs), as well.

A final measure of performance is stability, as mentioned above, and consists of measuring a material or device for long periods of time. Extended cycling of novel materials and devices enables the researcher to make inferences about the commercial application of the invention. Good stability studies involve materials

characterization post-measurement to evaluate failure or degradation mechanisms, and can provide insight as to what improvements would be needed to produce longer-lasting materials.

Scope of Dissertation

The following chapters present not only the development of novel, MoS_2-based electrodes, but their application in three alternative energy technologies: quantum dot sensitized solar cells (QDSSCs), the hydrogen evolution reaction (HER) for hydrogen fuels, and lithium-ion batteries (LIBs). Fundamental synthetic and electrochemical studies, comprehensive characterization, and real-world testing of these electrodes is performed. For each of these technologies, petaled MoS_2 electrodes have inherent advantages and disadvantages, which I attempt to describe and understand so that the material (and technologies) may be further improved.

In Chapter II, I demonstrate the preparation of a novel, self-supported, nanostructured MoS_2 material. We have coined this material "petaled MoS_2" or P. MoS_2 for short. P. MoS_2 is found to be an excellent polysulfide reduction catalyst which naturally lends itself to liquid-junction QDSSC technology. Thus, I tested it as a counter electrode in these devices.

In Chapter III, we discovered that during growth, P. MoS_2 electrodes go through an intermediate MoS_xO_y phase which is present in the final electrodes and serves as a conductive contact between the Mo substrate and the surface MoS_2 petals. This layer is shown to be beneficial to electrocatalytic HER for the production of hydrogen fuels. Also, P. MoS_2 was grown from an alternate, Au substrate using a new synthetic approach. This was done to limit the formation of the MoS_xO_y layer and act as a control, but it boasts greater instrinsic HER activity than the Mo substrate.

In Chapter IV, the applicability of P. MoS_2 in LIBs for energy storage is evaluated. It is found that the MoS_xO_y layer contributes greatly to the capacity of the electrode, while other typical Li-S cycling reactions are not as prevalent. *Ex situ* characterization is utilized to understand the primary chemical species and reactions involved in the charge/discharge processes.

In Chapter V, P. MoS_2 is again used as a counter electrode in QDSSCs employing novel, $Cu_2S@SnS$ core@shell nanocubes, prepared by Dr. Suresh Sarkar, as photoabsorbers. While the role of P. MoS_2 is not highlighted in this work, I developed a protocol for electrophoretically depositing this material onto TiO_2 photoanode. The $Cu_2S@SnS$, $SnS@Cu_2S$, and SnS nanocubes performed well for the selected application, and the differences in performance were discussed considering the type II band alignment of SnS and Cu_2S.

References

(1)   NASA Scientific Visualization Studio; NASA's Goddard Institute for Space Studies. Global Climate Change: Vital Signs http://climate.nasa.gov/vital-signs/global-temperature/ (accessed Nov 21, 2016).

(2)   World Population Growth https://ourworldindata.org/world-population-growth/ (accessed Nov 21, 2016).

(3)   PovcalNet iresearch.worldbank.org/PovcalNet/ (accessed May 23, 2016).

(4)   Kim, J. Y. Prosperity for All: Ending Extreme Poverty http://www.worldbank.org/en/news/feature/2014/04/10/prosperity-for-all-ending-extreme-poverty (accessed Jan 1, 2016).

(5)   Khan, S. A. R.; Zaman, K.; Zhang, Y. The Relationship between Energy-Resource Depletion, Climate Change, Health Resources and the Environmental Kuznets Curve: Evidence from the Panel of Selected Developed Countries. *Renew. Sustain. Energy Rev.* **2016**, *62*, 468–477.

(6)   Winegard, T. C. *The First World Oil War*; University of Toronto Press: Toronto.

(7)   Energy Poverty http://www.iea.org/topics/energypoverty/ (accessed Jan 1, 2016).

(8)   Office of Energy Efficiency & Renewable Energy. Hydrogen Production
        http://energy.gov/eere/fuelcells/hydrogen-production (accessed Jan 1, 2016).

(9)   Office of Energy Efficiency & Renewable Energy. Fuel Properties Comparison
        http://www.afdc.energy.gov/fuels/fuel_comparison_chart.pdf (accessed Jan 1, 2016).

(10)   Energy Information Administration. *Annual Energy Outlook 2009: With Projections to 2030*; 2009.

(11)   Energy Information Administration. *Annual Energy Outlook 2010: With Projections to 2035*; 2010.

(12)   Transparent Cost Database http://en.openei.org/wiki/Transparent_Cost_Database (accessed Jan 1, 2016).

(13)   *Cost Report: Cost and Performance Data for Power Generation Technologies*; 2012.

(14)   Feldman, D.; Barbose, G.; Margolis, R.; Darghouth, N.; James, T.; Weaver, S.; Goodrich, A.; Wiser, R.
        Photovoltaic System Pricing Trends: Historical, Recent, and Near-Term Projections 2013 Edition; 2013.

(15)   Hubbell, R.; Lowder, T.; Mendelsohn, M.; Cory, K. Renewable Energy Finance Tracking Initiative
        (REFTI) Solar Trend Analysis. **2009**.

(16)   Hasler, D. *New Coal-Fired Power Plant Performance and Cost Estimates*; 2009.

(17)   *Energy Technology Perspectives 2012: Pathways to a Clean Energy System*; 2012.

(18)   *Biomass for Power Generation*; Renewable Energy Technologies: Cost Analysis Series; 2012; Vol. 1.

(19)   Turchi, C. *Parabolic Trough Reference Plant for Cost Modeling with the Solar Advisor Model (SAM)*;
        2010.

(20)   Mai, T.; Wiser, R.; Sandor, D.; Brinkman, G.; Heath, G.; Denholm, P.; Hostick, D. J.; Darghouth, N.;

Schlosser, A.; Strzepek, K. *Exploration of High-Penetration Renewable Electricity Futures*; Golden, CO, 2012; Vol. 1.

(21) Tegen, S.; Hand, M.; Maples, B.; Lantz, E.; Schwabe, P.; Smith, A. *2010 Cost of Wind Energy Review*; Golden, CO, 2010.

(22) Mai, T.; Mulcahy, D.; Hand, M. M.; Baldwin, S. F. Envisioning a Renewable Electricity Future for the United States. *Energy* **2014**, *65*, 374–386.

(23) Wiser, R.; Bolinger, M. *2013 Wind Technologies Market Report*; 2013.

(24) McCann, R.; Walters, W. *Cost of Generation Workshop: Natural Gas Technologies*; 2013.

(25) McCann, R. *Cost of Generation Workshop: Non-Solar Renewables*; 2013.

(26) NREL. Annual Technology Baseline and Standard Scenarios http://www.nrel.gov/analysis/data_tech_baseline.html (accessed Jan 1, 2016).

(27) *SunShot Vision Study*; 2012.

(28) AMPEREDB Database Webmaster. AMPERE Public Database https://secure.iiasa.ac.at/web-apps/ene/AMPEREDB/dsd?Action=htmlpage&page=welcome (accessed Jan 1, 2016).

(29) OpenEI International Sponsors and Partners http://en.openei.org/wiki/OpenEI_International_Sponsors_and_Partners (accessed Jan 1, 2016).

(30) Wang, Y.-J.; Fang, B.; Li, H.; Bi, X. T.; Wang, H. Progress in Modified Carbon Support Materials for Pt and Pt-Alloy Cathode Catalysts in Polymer Electrolyte Membrane Fuel Cells. *Prog. Mater. Sci.* **2016**, *82*, 445–498.

(31) Wachsman, E. D.; Lee, K. T. Lowering the Temperature of Solid Oxide Fuel Cells. *Science (80-.).* **2011**, *334* (6058).

(32)　Holladay, J. D.; Hu, J.; King, D. L.; Wang, Y. An Overview of Hydrogen Production Technologies. *Catal. Today* **2009**, *139* (4), 244–260.

(33)　Faber, M. S.; Jin, S. Earth-Abundant Inorganic Electrocatalysts and Their Nanostructures for Energy Conversion Applications. *Energy Environ. Sci.* **2014**, *7* (11), 3519–3542.

(34)　Yu, W. W.; Qu, L.; Guo, W.; Peng, X. Experimental Determination of the Extinction Coefficient of CdTe, CdSe, and CdS Nanocrystals. *Chem. Mater.* **2003**, *15* (14), 2854–2860.

(35)　Brus, L. Electronic Wave Functions in Semiconductor Clusters: Experiment and Theory. *J. Phys. Chem* **1986**, *90*, 2555–2560.

(36)　Enyashin, A.; Gemming, S.; Seifert, G. Nanosized Allotropes of Molybdenum Disulfide. *Eur. Phys. J. Spec. Top.* **2007**, *149*, 103–125.

(37)　Cotton, F. A.; Wilkinson, G.; Murillo, C. A.; Bochman, M. *Advanced Inorganic Chemistry*, 6th ed.; John Wiley & Sons (Asia) Pt. Ltd.: Singapore, 2004.

(38)　Rapoport, L.; Moshkovich, a.; Perfilyev, V.; Laikhtman, a.; Lapsker, I.; Yadgarov, L.; Rosentsveig, R.; Tenne, R. High Lubricity of Re-Doped Fullerene-Like MoS2 Nanoparticles. *Tribol. Lett.* **2012**, *45* (2), 257–264.

(39)　Wilcoxon, J. P.; Newcomer, P. P.; Samara, G. a. Synthesis and Optical Properties of MoS$_2$ and Isomorphous Nanoclusters in the Quantum Confinement Regime. *J. Appl. Phys.* **1997**, *81* (1997), 7934.

(40)　Schneemeyer, L. F.; Wrighton, M. S. Flat-Band Potential of N-Type Semiconducting Molybdenum Disulfide by Cyclic Voltammetry of Two-Electron Reductants: Interface Energetics and the Sustained Photooxidation of Chloride. *J. Am. Chem. Soc.* **1979**, *101*, 6496–6500.

(41)　Lessner, P. M.; McLarnon, F. R.; Winnick, J.; Cairns, E. J. Aqueous Polysulphide Flow-through Electrodes: Effects of Electrocatalyst and Electrolyte Composition on Performance. *J. Appl.*

Electrochem. **1992**, *22* (10), 927–934.

(42)   Topsøe, H.; Clausen, B. S.; Massoth, F. E. Hydrotreating Catalysis. In *Catalysis*; Springer: Berlin,

Heidelberg, 1996; pp 1–269.

(43)   Daage, M.; Chianelli, R. R. Structure-Function Relations in Molybdenum Sulfide Catalysts: The "Rim-

Edge" Model. *J. Catal.* **1994**, *149* (2), 414–427.

(44)   Jaramillo, T. F.; Jørgensen, K. P.; Bonde, J.; Nielsen, J. H.; Horch, S.; Chorkendorff, I. Identification of

Active Edge Sites for Electrochemical H_2 Evolution from MoS_2 Nanocatalysts. *Science* **2007**, *317* (July),

100–102.

(45)   Kibsgaard, J.; Chen, Z.; Reinecke, B. N.; Jaramillo, T. F. Engineering the Surface Structure of MoS_2 to

Preferentially Expose Active Edge Sites for Electrocatalysis. *Nat. Mater.* **2012**, *11* (11), 963–969.

(46)   Kong, D.; Wang, H.; Cha, J. J.; Pasta, M.; Koski, K. J.; Yao, J.; Cui, Y. Synthesis of MoS_2 and $MoSe_2$

Films with Vertically Aligned Layers. *Nano Lett.* **2013**, *13* (3), 1341–1347.

(47)   Bouroushian, M. *Electrochemistry of the Metal Chalcogenides*, 1st ed.; Scholz, F., Ed.; Springer: Berlin,

2010.

(48)   Chen, Z.; Forman, A. J.; Jaramillo, T. F. Bridging the Gap between Bulk and Nanostructured

Photoelectrodes: The Impact of Surface States on the Electrocatalytic and Photoelectrochemical

Properties of MoS_2. *J. Phys. Chem. C* **2013**, *117* (19), 9713–9722.

(49)   Turo, M. J.; Shen, X.; Brandon, N. K.; Castillo, S.; Fall, A. M.; Pantelides, S. T.; Macdonald, J. E. Dual-

Mode Crystal-Bound and X-Type Passivation of Quantum Dots. *Chem. Commun.* **2016**, *52* (82), 12214–

12217.

(50)   Sarkar, S.; Leach, A. D. P.; Macdonald, J. E. Folded Nanosheets: A New Mechanism for Nanodisk

Formation. *Chem. Mater.* **2016**, *28* (12), 4324–4330.

(51) Alivisatos, A. P. Semiconductor Clusters, Nanocrystals, and Quantum Dots. *Science (80-.).* **1996**, *271* (5251), 933–937.

(52) Bowers, M. J.; McBride, J. R.; Rosenthal, S. J. White-Light Emission from Magic-Sized Cadmium Selenide Nanocrystals. **2005**.

(53) Li, W.-J.; Shi, E.-W.; Ko, J.-M.; Chen, Z.; Ogino, H.; Fukuda, T. Hydrothermal Synthesis of MoS_2 Nanowires. *J. Cryst. Growth* **2003**, *250* (3–4), 418–422.

(54) Ma, L.; Chen, W.-X.; Li, H.; Zheng, Y.-F.; Xu, Z.-D. Ionic Liquid-Assisted Hydrothermal Synthesis of MoS_2 Microspheres. *Mater. Lett.* **2008**, *62* (6–7), 797–799.

(55) Peng, Y.; Meng, Z.; Zhong, C.; Lu, J.; Yu, W.; Jia, Y.; Qian, Y. Hydrothermal Synthesis and Characterization of Single-Molecular-Layer MoS_2 and $MoSe_2$. *Chem. Lett.* **2001**, *30* (8), 772–773.

(56) Liang, H.; Meng, F.; Cabán-Acevedo, M.; Li, L.; Forticaux, A.; Xiu, L.; Wang, Z.; Jin, S. Hydrothermal Continuous Flow Synthesis and Exfoliation of NiCo Layered Double Hydroxide Nanosheets for Enhanced Oxygen Evolution Catalysis. *Nano Lett.* **2015**, *15* (2), 1421–1427.

(57) Ye, L.; Guo, W.; Yang, Y.; Du, Y.; Xie, Y. Directing the Architecture of Various MoS_2 Hierarchical Hollow Cages through the Controllable Synthesis of Surfactant/molybdate Composite Precursors. *Chem. Mater.* **2007**, *19*, 6331–6337.

(58) Ye, L.; Wu, C.; Guo, W.; Xie, Y. MoS2 Hierarchical Hollow Cubic Cages Assembled by Bilayers: One-Step Synthesis and Their Electrochemical Hydrogen Storage Properties. *Chem. Commun. (Camb).* **2006**, *2*, 4738–4740.

(59) Punter, J.; Colomer-Farrarons, J.; Ll., P. Bioelectronics for Amperometric Biosensors. In *State of the Art in Biosensors - General Aspects*; InTech, 2013.

Petaled Molybdenum Disulfide Surfaces: Facile Synthesis of a Superior Cathode for QDSSCs.[1]
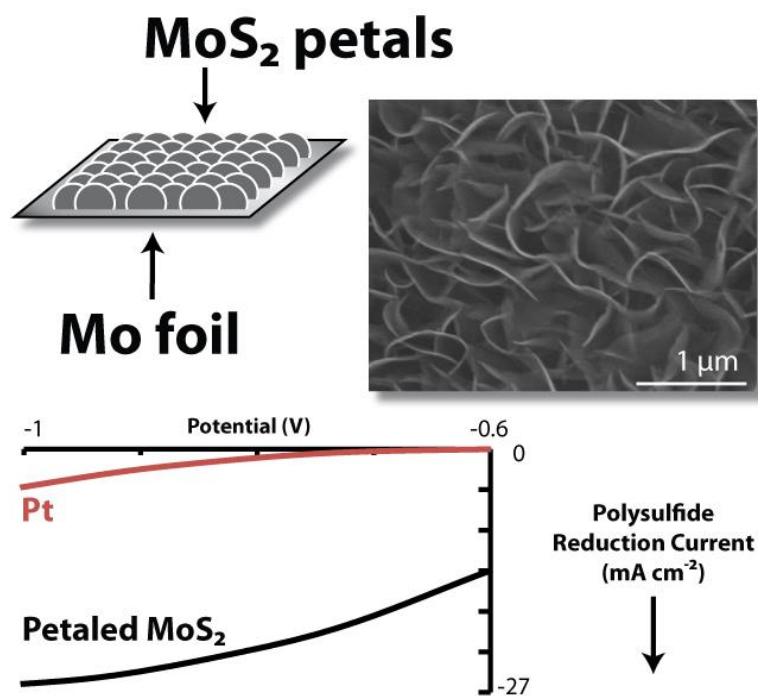
Introduction

Quantum dot sensitized solar cells (QDSSCs) have the potential to revolutionize solar energy conversion due to the large extinction coefficients and tunable band gaps of quantum dots;[1] efficiencies of over 5% have been achieved using this design.[2] Great strides are being made into developing new, more efficient absorber

---

layers on the photoanode;[3] however, instability and poisoning of standard cathode materials limit champion cell performances and make it challenging to identify important characteristics of experimental photoanodes. Ultimately, poor cathode performance will hinder a commercially viable QDSSC technology.[4,5] While QDSSC photoanodes are and have been extensively studied,[3] cathodes designed to improve cell characteristics have only just recently come under renewed investigation.[5–11]

The distinguishing quality of QDSSCs is that quantum dots (QDs) – typically metal chalcogenides such as CdSe or PbS – function as the light-absorbing component rather than dyes or silicon. QDs are an attractive photoabsorber material because they have large absorption coefficients and their absorption onset in the visible region can be tuned based on their size and composition. In a QDSSC (**Figure 1**), light is absorbed by QDs on the photoanode, and the accompanying excited electron is shuttled through the transparent conducting oxide(s) while the remaining hole on the QD is reduced by the electrolyte. While many electrolytes have been attempted, the S_n^{2-}/S^{2-} (polysulfide) redox system has proven the most effective so far because of its optimal redox potential, efficient hole extraction from the QDs, and ability to chemically stabilize QDs such as CdS, PbS, and Ag_2S.[4]
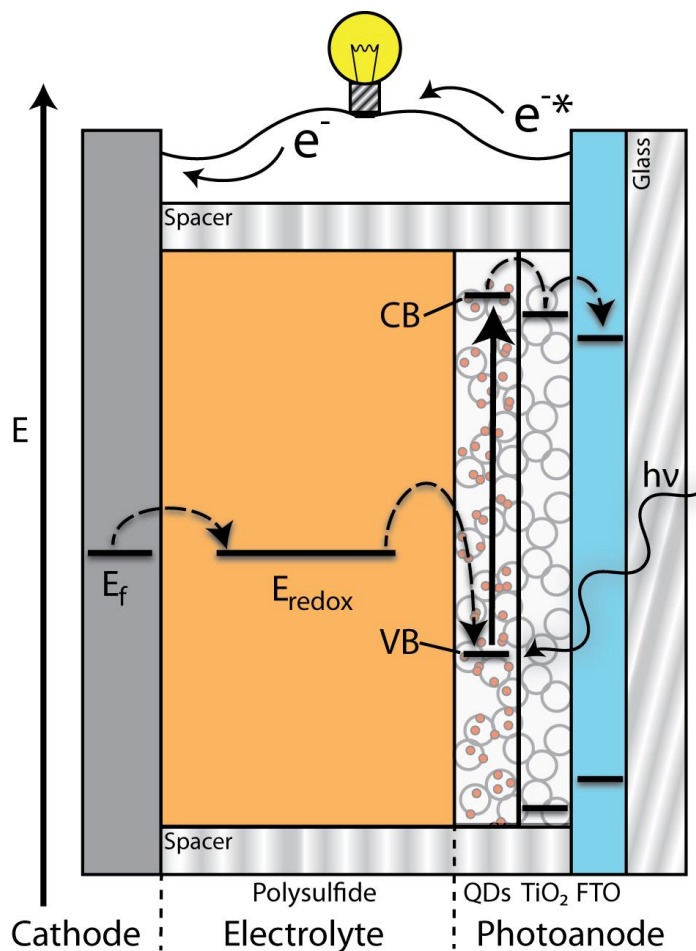
Figure 1. Typical QDSSC overlaid with relative electron energetics (not to scale). At the photoanode, photons with sufficient energy (hv) will strike the QD, exciting an electron (e⁻) from the valence band (VB) to the conduction band (CB). The excited electron (e⁻*) will conduct by traveling to TiO_2 then the fluorine-doped tin(IV) oxide (FTO) CBs. Electrons travel out of the photoanode, do work, and return to the cell via the cathode. The cathode Fermi level (E_f), to which the redox potential (E_{redox}) of the electrolyte ($E^0_{polysulfide} = -0.5$ V *vs.* NHE) equalizes, reduces the electrolyte, which carries negative charge to the photo-generated hole in the QD.

The cathode must be able to reduce the electrolyte to complete the circuit. The most common cathode used for evaluating QDSSCs is platinum, followed by gold and glassy carbon; however, all are quickly poisoned by the polysulfide, resulting in significant drops in current. Thus, these materials require large overpotentials to operate, lowering solar cell efficiencies and making them unsuitable for long-term use in a device. Also, platinum is rare and expensive, so replacing it with an inexpensive, earth-abundant material is an necessary goal.

Semiconducting metal sulfides such as Cu_2S, PbS and CoS are highly catalytically active for polysulfide reduction, but early studies of these materials showed that they were not stable under operating conditions. Specifically, the PbS device dropped to 10% of its initial current density after two weeks and both Cu_2S and CoS dissolved and migrated to deposit on the photoanode, causing the power conversion efficiency to drop significantly.[12] Very recently, cathode preparations based on supported nanoparticles of PbS and Cu_2S have shown improved stability.[6,9,11]

Another potential candidate material for highly stable and catalytically active cathodes for polysulfide reduction is molybdenum(IV) sulfide (MoS_2). Lately, MoS_2 has been the subject of a flurry of research (see Chapter I, Fig. 4) due to its layered structure and interesting properties as a two-dimensional material, similar to graphene.[13] MoS_2 is a potential component in field-effect transistors[14] and dye sensitized solar cells[15] as well as an intercalation host for lithium ion batteries.[16] However, its known catalytic activity is most relevant here as it has long been used as an industrial hydrodesulfurization (HDS) catalyst[17] and has been shown to be an electrocatalyst for the hydrogen evolution reaction (HER),[13] both of which showcase its potential as a stable catalyst for sulfur electrochemistry.

The electronic structure of MoS_2 provides electrochemical stability as a cathode because the valence and conduction bands are seated in relatively non-bonding orbitals, dominated by Mo 4d character.[18] This is in contrast to late transition metal sulfides such as the electrochemically unstable PbS, CoS and Cu_2S where the valence and conduction bands are in strongly bonding and antibonding orbitals, respectively.

The research groups of Jaramillo and Cui have recently developed novel, highly controlled ways to expose the active edges of MoS_2 for HER cathodes, but these methods require several steps, expensive equipment, vacuum-assisted or inert atmosphere techniques, and hazardous chemicals.[19,20] Previously, a hydrothermal route produced flower-like MoS_2 spheres presenting a large number of freestanding edge sites, which has been reproduced by our group as featured in the scanning electron microscopy (SEM) images in **Figure 2**.[21] Thus, modifications of this type of reaction and material became our focus. Generally, hydrothermal syntheses are attractive synthetic routes, as high surface area, hierarchical crystal structures of the first row

transition metal sulfides are common products.[22–25] Hydrothermal syntheses are typically experimentally facile, one-pot reactions which employ common, stable reagents.
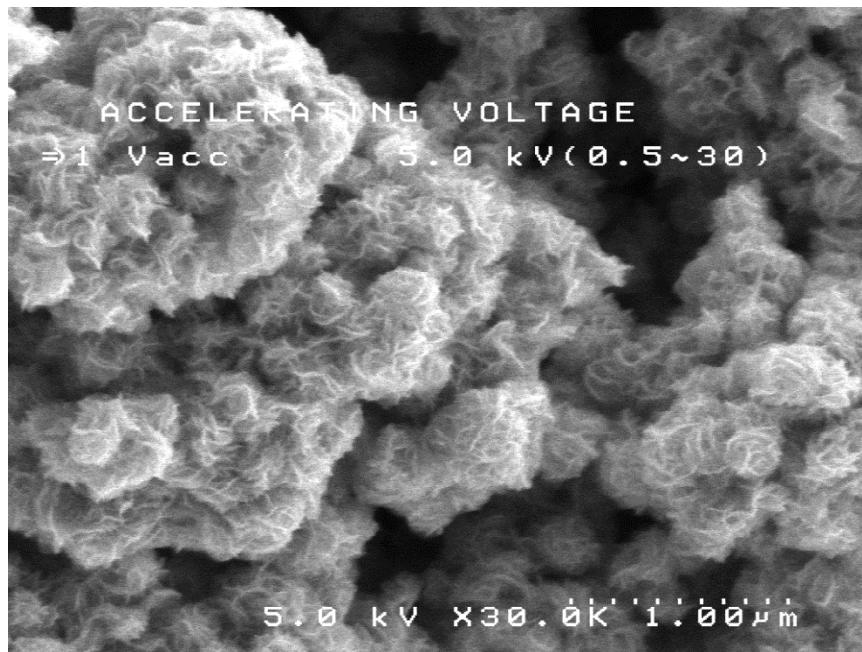
Figure 2. SEM image of loose, flower-like MoS_2 spheres.

Here, we have developed a one-step, scalable, hydrothermal synthesis of a MoS_2 electrode that preferentially exposes MoS_2 active edges, incorporates a vertical directionality of the crystallites that promotes electron conduction, and can be used as a cathode for QDSSC and HER without further modification.

Experimental

All chemicals were obtained from Sigma-Aldrich unless otherwise noted and all water was purified using Millipore® Direct-Q3 System to 18.2 MΩ•cm resistivity.

Petaled MoS$_2$ and MoSe$_2$ Syntheses

Petaled MoS$_2$ was grown from Mo foil via a hydrothermal synthesis technique. Thiourea (1.847 mmol), 1.5 x 1.5 cm^2 Mo foil (99.95%, Strem) and 15.0 mL water were added to 23 mL PTFE cup with lid, assembled into a stainless steel autoclave (Parr Instrument Company) and suspended in a silicone oil bath. The bath was heated to 180°C and maintained at this temperature for 18 hours. After cooling to room temperature, the autoclave was removed from the oil bath, disassembled and the product removed. The product was soaked in three separate rinses of water for at least 1 minute per soak. Petaled MoSe$_2$ was also prepared by following the P. MoS$_2$ procedure, but with the following changes. An equimolar amount of Se powder was used instead of S, and the autoclave was heated at 230°C for 24 h.

Characterization

Petaled MoS$_2$ electrodes were characterized using Raman spectroscopy (Thermo Scientific DXR Raman Microscope) to confirm presence of MoS$_2$. Electrodes were imaged using scanning electron microscopy (Hitachi S-4200).

FTO Preparation

All SnO$_2$:F (FTO) on glass pieces (TCO22-7, Solaronix) were cut to ~2 x 2 cm^2 and cleaned via sonication in an ultrasonic bath (VWR Symphony) for 10 minutes in each of the following solvents, consecutively: acetone, ethanol, water. FTO pieces used for photoanodes were cleaned by sonicating in a solution of Versa Clean™ (Fisherbrand®) in water for 30 min, scrubbing with a lab tissue soaked in soapy water, rinsed with water, then sonicated for 15 min in ethanol, rinsed with ethanol and dried with an air stream.

High Surface Area Pt Electrodes

Platinum electrodes were prepared by the electron beam evaporation (Angstrom Engineering Ǻmod) of a 5-nm Cr adhesion layer followed by a ~100 nm Pt layer onto clean FTO/glass pieces. To increase the Pt surface area to make the electrodes more comparable to the high surface area petaled MoS_2 electrodes, a 5 mM K_2PtCl_6 suspension in isopropanol was dropped onto the surface of the e-beam evaporated Pt electrodes and allowed to dry, then annealed at 380°C for 15 minutes.

Other Electrodes

Other electrodes used for comparison were Au evaporated on Si (with Cr adhesion layer), Mo foil, FTO and glassy carbon (CH Instruments, Inc.). All electrodes except glassy carbon were cleaned before use according to FTO cleaning procedure described above. Glassy carbon electrodes were cleaned by polishing with moistened 0.05 µm alumina powder on a felt pad (CH Instruments, Inc.).

Electrolyte

Polysulfide electrolyte solution (1M Na_2S, 0.1M S, 0.1M KOH) was prepared by combining $Na_2S\bullet 9H_2O$ (Strem), S, and KOH with water, heating to 60°C under N_2 atmosphere until S dissolved and cooling to room temperature. 0.1M KOH control solution was made by dissolving KOH in H_2O. In QDSSCs, a 2M S^{2-}, 2M S polysulfide solution was prepared by combining desired amounts of $Na_2S\bullet 9H_2O$ and S in ~5 mL water, sonicating 1 h, and diluting to desired final volume. This solution was not kept under inert atmosphere.

Electrochemical Measurements

Electrochemistry (Gamry Series G 300 with PHE200 Software Package) was used to determine electrode characteristics. Electrochemical techniques employed were linear sweep voltammetry and

chronoamperometry. Electrodes were evaluated individually by submerging in polysulfide solution along with a 1 M Ag/AgCl reference electrode and Pt mesh counter electrode, then measured using linear sweep voltammetry from -0.6 to -1 V vs. Ag/AgCl (1 M) at a scan rate of 0.1 V s^{-1} and 2 mV voltage step. Cathodes were measured without respect to illumination. Control measurements of petaled MoS_2 and high surface area Pt cathodes were carried out in 0.1 M KOH solution. Loose flower-like MoS_2 spheres were electrochemically evaluated by drop-casting a suspension of the spheres in toluene onto a glassy carbon electrode and measuring current from -0.4 V to -1 V in polysulfide (1 M Na_2S, 1M S, 1 M KOH) and 1 M KOH control solutions.

Photoanode Preparation

Photoanodes were prepared by treating cleaned FTO/glass pieces with $TiCl_4$ (Strem) before and after a doctor blade application of TiO_2 paste by placing pieces in the bottom of a dish, covering the pieces with 40 mM $TiCl_4$ in water and placing the dish in a 70°C oven for 30 minutes. The FTO pieces were then removed and rinsed with water and ethanol, and then dried. TiO_2 paste was applied to FTO/glass pieces via doctor blade technique: a 6x9 cm^2 FTO piece was placed over a template and tape pieces of appropriate width were placed over the template in a grid to mark off the active areas. Then, a small amount of active layer paste (Ti-Nanoxide T/SP, Solaronix) was placed in front of every other active area lengthwise. A Ti doctor blade was then pressed at a ~45° angle and dragged down the length of the FTO piece enough times to apply the paste evenly. The TiO_2 paste was allowed to rest, covered ~15 min then dried in an 80°C oven 1h. Then, the FTO piece was annealed in a tube furnace: pieces were placed in at <350°C, ramped to 350°C for 5 min, soaked at 350°C for 10 min, and so on at 400°C, 450°C, and 500°C, then allowed to cool to room temp. The process of applying a tape grid, then TiO_2 paste, resting, drying, and annealing was repeated for the scattering layer, but the paste used was PST-400C (JGC Catalysts & Chemicals) and the tape template resulted in areas slightly larger than the active layer area. Finally, the electrodes were treated again with 40mM $TiCl_4$ and annealed at 500°C for 30 min.

Successive ionic layer adsorption and reaction (SILAR) was then performed on TiCl$_4$-treated TiO$_2$/FTO/glass pieces to form a CdS layer. Pieces were submerged in 0.1 M Cd(NO$_3$)$_2$ (Strem) in methanol for 1 minute, rinsed with methanol, dried with air stream, submerged in 0.1M Na$_2$S in 1:1 methanol:water for 1 minute, then rinsed, and dried; 10 of these cycles were repeated per photoanode. After CdS deposition, a protective ZnS layer was applied via SILAR: photoanodes were dipped as before, but in 0.1M Zn(NO$_3$)$_2$ (Strem) in methanol instead of Cd(NO$_3$)$_2$; 2 of these cycles were repeated per photoanode, then photoanodes were stored in the dark.

QDSSC Construction and Testing

Solar devices were constructed by cutting a ~1.5 x 1.1 cm^2 piece of Parafilm® with a 0.7 x 0.7 cm^2 square cut out of the center. This was applied to the cathode, and then placed on a 100°C hot plate until the parafilm began to melt; the cathode was quickly removed and parafilm pressed to the cathode to remove air bubbles. Then, the cathode was placed face-up. Excess polysulfide solution (~4 drops) was added to the square, and then the photoanode was placed face-down over it and clamped down using binder clips. Then the device was rinsed with water and dried in a N$_2$ stream.

Devices were tested by positioning them in the center of and perpendicular to the light beam from the 500W Hg(Xe) arc lamp (Newport Corporation) at a predetermined distance such that the light reaching the device was equal to 1 Sun intensity (1000 W m^{-2}). Then, the working electrode was attached to the photoanode FTO, and the counter and reference electrode leads were attached to the cathode. Linear sweep voltammetry scans from 0.1 – (-0.6) V at 2 mV s^{-1} scan rate were taken in the dark and under illumination. Device stability was assessed using chronoamperometry, where 0 V was applied for 5 minutes (dark) and 24 hours (illuminated).

Petaled MoS$_2$ Synthesis

Flower-like MoS$_2$ spheres were prepared by a modified hydrothermal synthesis from the literature[21,26] in which the spheres exhibited preferential edge growth perpendicular to the core (**Scheme 1**a). Simply, sodium molybdate, thiourea, hydrochloric acid, and water were combined in a PTFE cup, assembled into a stainless steel autoclave and heated at 180°C for 24h (Scheme 1a). When drop-cast onto a glassy carbon (GC) electrode, these loose spheres improved the current density achieved by glassy carbon alone for polysulfide reduction (**Figure 3**a) but did not show significant HER activity over GC in basic solution (Figure 3b).
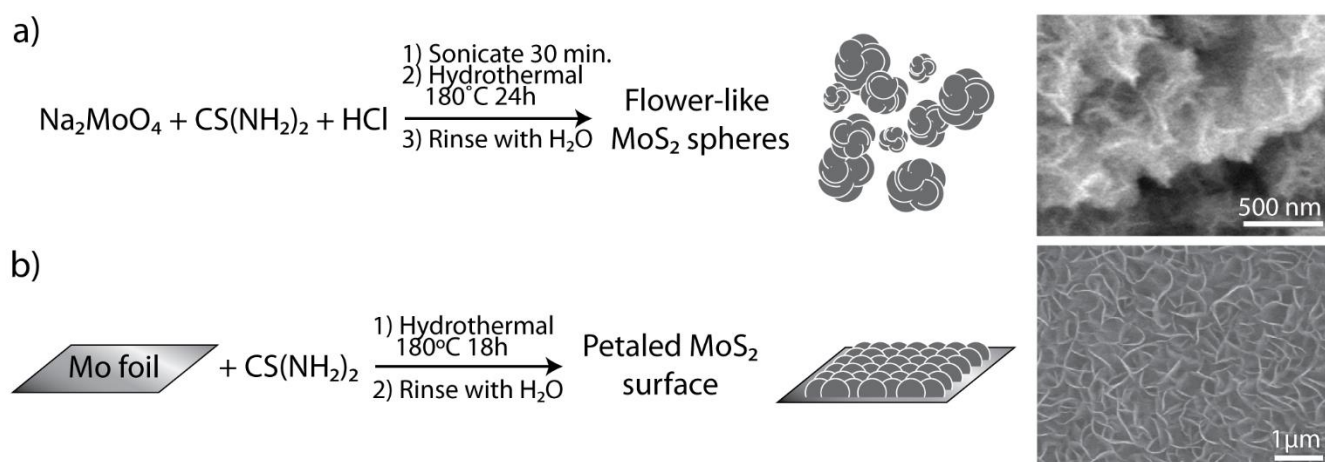
Scheme 1. Hydrothermal syntheses to produce nanostructured MoS$_2$: a) flower-like spheres and b) petaled MoS$_2$.
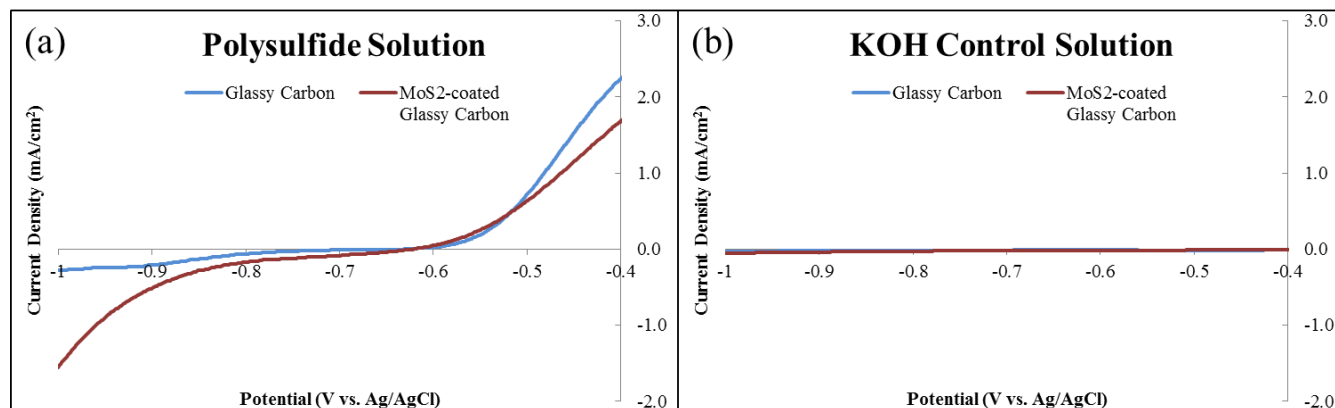
Figure 3. Linear sweep voltammograms of glassy carbon electrodes with and without MoS₂ flowers drop-cast onto them in a) polysulfide and b) KOH solution.

In order to adapt this material for applications requiring flat electrodes and improve conductivity to a metallic contact, the MoS₂ flower structures needed to be grown uniformly from a conducting surface. The Xie group demonstrated that hollow cubes of MoS₂ petals could be hydrothermally grown from a Mo-containing insoluble intermediate template structure.[21,27,28] We adapted this methodology by using molybdenum foil as the insoluble Mo-containing template material in the hydrothermal reaction (Scheme 1b). SEM (Scheme 1b and **Figure 4**a) showed the product to be a uniform layer of MoS₂ petals aligned normal to the Mo foil with a high number of edges exposed – a nearly ideal result. We have coined the term "petaled MoS₂" (P. MoS₂) to describe this material.
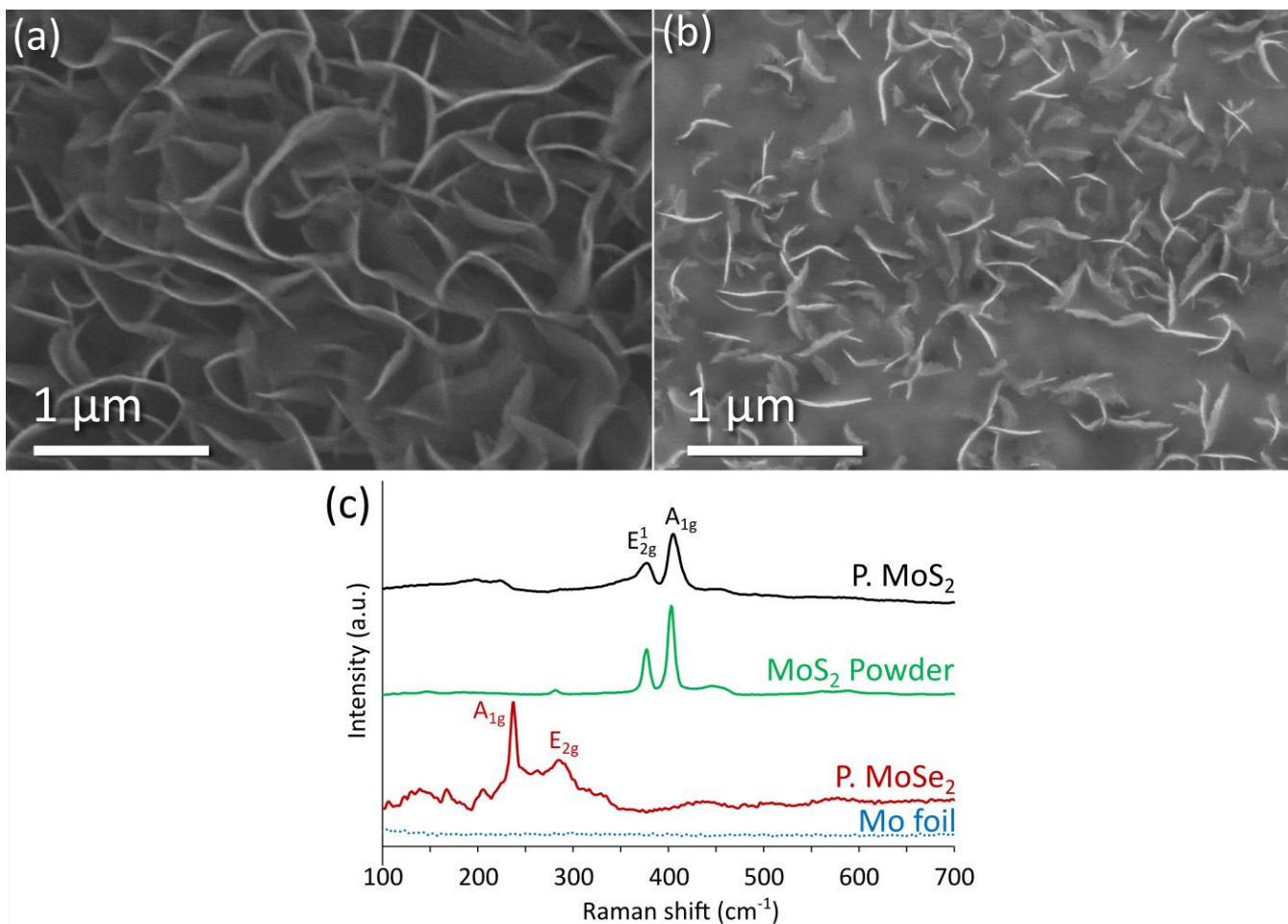
Figure 4. SEM image of a typical (a) P. MoS$_2$ and (b) P. MoSe$_2$ electrode; (c) Raman spectra of a P. MoS$_2$ electrode, MoS$_2$ powder, P. MoSe$_2$ and a Mo foil control.

Raman spectroscopy was used to confirm the presence of MoS$_2$ (Figure 4c) which exhibits two large characteristic peaks at 376 and 403 cm^{-1}, corresponding to the E_{2g}^1 symmetric in-plane and A_{1g} out-of-plane S-Mo-S stretching, respectively.[29] The Raman peaks of the P. MoS$_2$ electrode align well with MoS$_2$ powder (Aldrich), but are slightly offset, especially in the case of the A_{1g} mode, which is most likely because fewer bundled MoS$_2$ trilayers are being excited by the laser.[30–32] A Raman spectrum of the Mo foil shows that it does not contribute to the Raman signal of MoS$_2$ at these wavenumbers.

It has been shown that MoS$_{2(1-x)}$Se$_{2x}$ alloys, where S:Se is 1:1, have improved HER activity compared to MoS$_2$ or MoSe$_2$.[33] So, as a step towards preparing these catalysts and demonstrating the versatility of the synthetic approach, P. MoSe$_2$ was also prepared by using an equimolar amount of Se powder in place of S and

heating at 230°C for 24 h. This synthesis formed a more diffuse arrangement of petals (Figure 4b). Like MoS_2, $MoSe_2$ features characteristic A_{1g} (240 cm^{-1}) and E_{2g} (290 cm^{-1}) modes due to out-of-plane and in-plane stretching, respectively, of its Se-Mo-Se trilayers.[34,35] The $MoSe_2$ petals appear to grow from a MoO_2 intermediate phase, as evidenced by the 205 cm^{-1} Raman peak;[36] however, further studies would be needed to confirm this. A very slight peak at 205 cm^{-1} is also observed in P. MoS_2, which might suggest the presence of MoO_2 in this material, but we instead find that it arises due to the single-layer nature of the MoS_2 petal edges, which will be discussed further in the next chapter.

Electrochemical Characterization

Evaluation of the petaled MoS_2 electrochemical performance was carried out via linear sweep voltammetry (LSV) in 1M Na_2S, 0.1M S, 0.1M KOH polysulfide solution (**Figure 5**a). LSV scans from -0.6 to -1 V show that much higher current densities can be achieved using petaled MoS_2 electrodes than many other common materials such as Pt, Au, glassy carbon, and FTO. Mo foil did not perform nearly as well as petaled MoS_2 electrodes for reducing polysulfide, so it can be concluded that the high performance of petaled MoS_2 does not originate from Mo foil. The petaled MoS_2 achieved current densities at least six times higher than other common electrode materials.
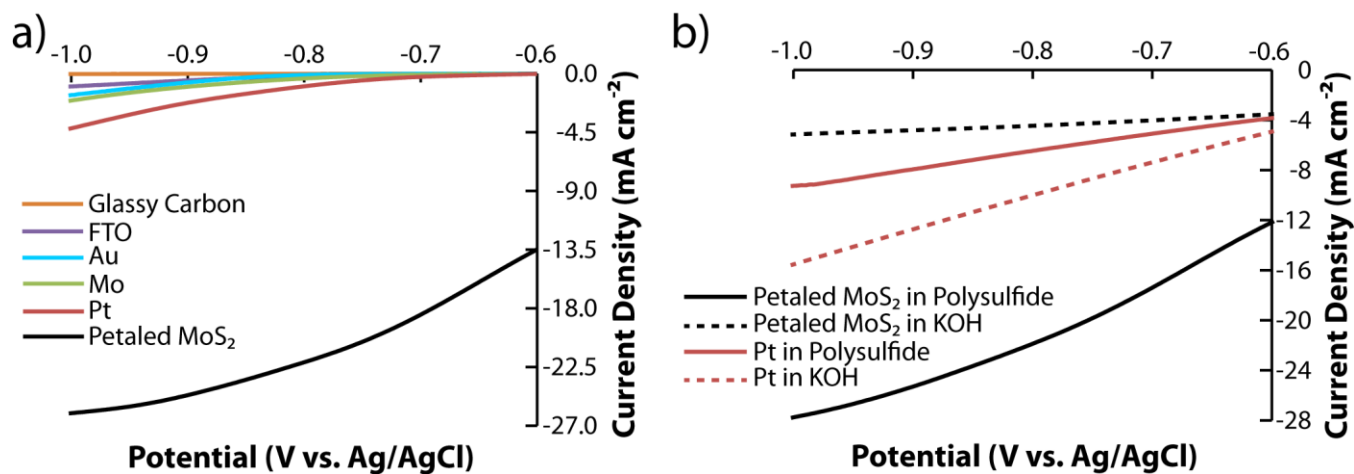
Figure 5. a) Linear sweep voltammetry of various electrode materials in polysulfide solution: petaled MoS$_2$ electrode, high surface area Pt, Mo, Au, FTO, and glassy carbon. b) Linear sweep voltammetry of petaled MoS$_2$ and Pt electrode materials in polysulfide and KOH control solutions.

Also, the known catalytic reduction of water on MoS$_2$ is not a large contributor to the current density of petaled MoS$_2$ in polysulfide. When the control measurement was taken in 0.1 M KOH solution (Figure 5b), where only water reduction will contribute to the measured current, the current density on the petaled MoS$_2$ electrode was much smaller than in polysulfide. Indeed, Pt outperformed petaled MoS$_2$ for water reduction. Furthermore, it was noted that the current density on high surface area Pt was smaller in polysulfide than in KOH. It is inferred from these observations that the high performance of petaled MoS$_2$ electrode toward polysulfide is not only the result of large surface area. The petaled MoS$_2$ *catalytically* reduces polysulfide, whereas Pt is not catalytic for this reaction but is instead poisoned in the polysulfide environment.
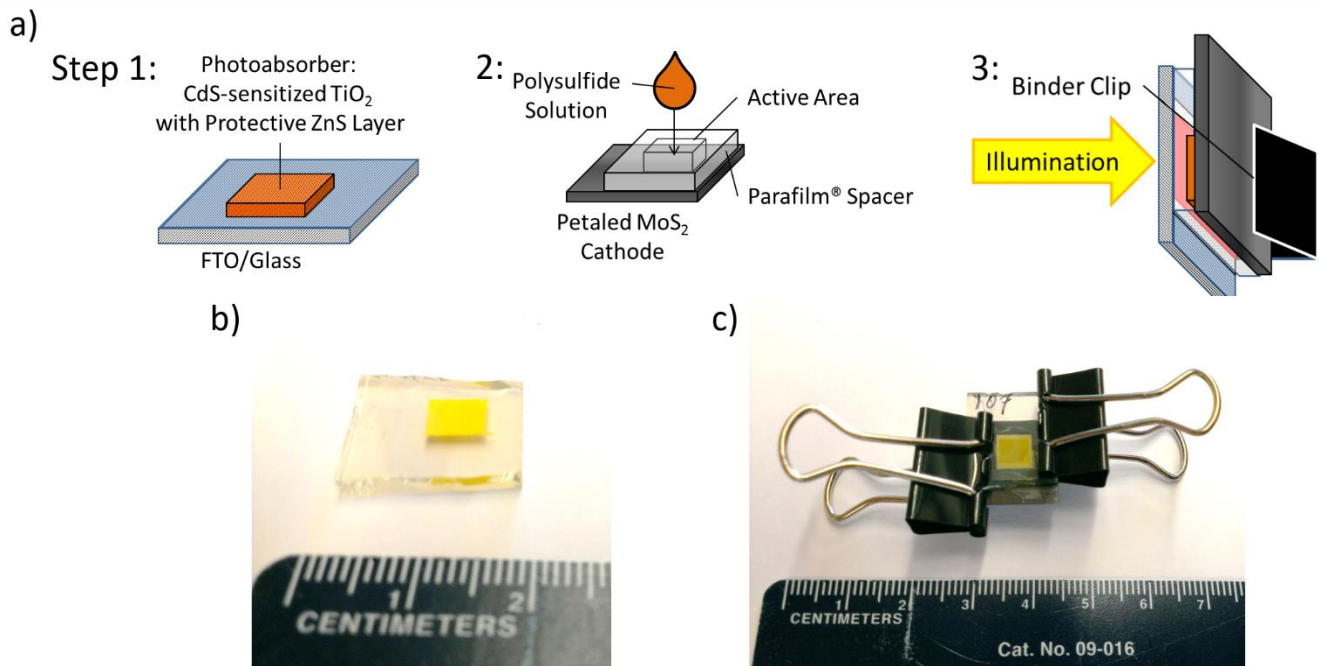
Figure 6. (a) Scheme representing preparation of photoanode (Step 1), cathode with spacer and electrolyte (Step 2) and cell assembly configuration (Step 3). (b, c) images of photoanode and assembled device, respectively.

Experimental QDSSCs

Experimental QDSSCs were prepared (as summarized in **Figure 6**) and tested to compare petaled MoS_2 and high surface area Pt as cathode materials. Photoanodes were prepared by applying TiO_2 paste (Ti-Nanoxide T/SP, Solaronix) to a $TiCl_4$-treated[37,38] FTO electrode via doctor blade technique, followed by annealing. CdS and ZnS QD layers were then deposited onto the TiO_2 via successive ionic layer adsorption and reaction (SILAR).[6,9] A representative photoanode is depicted in Figure 6a (Step 1) and b. Devices were constructed by applying Parafilm® as a spacer to petaled MoS_2, Pt, or Au cathode, filling the active area with polysulfide electrolyte (2M Na_2S, 2M S; Figure 6a, Step 2) and clamping a QD-sensitized TiO_2/FTO photoanode to the cathode with binder clips (Figure 6a, Step 3, and c). These devices were evaluated by attaching the working electrode clip to the photoanode and the counter and reference electrode clips to the cathode, then sweeping the potential from 0.1 to -0.6 V in the dark and under illumination (**Figure 7**). The numeric values for cell

characteristics including short-circuit current density (J_{sc}), open-circuit voltage (V_{oc}), and the calculated values

for fill factor (*FF*) and efficiency (η) are listed in **Table 1**.
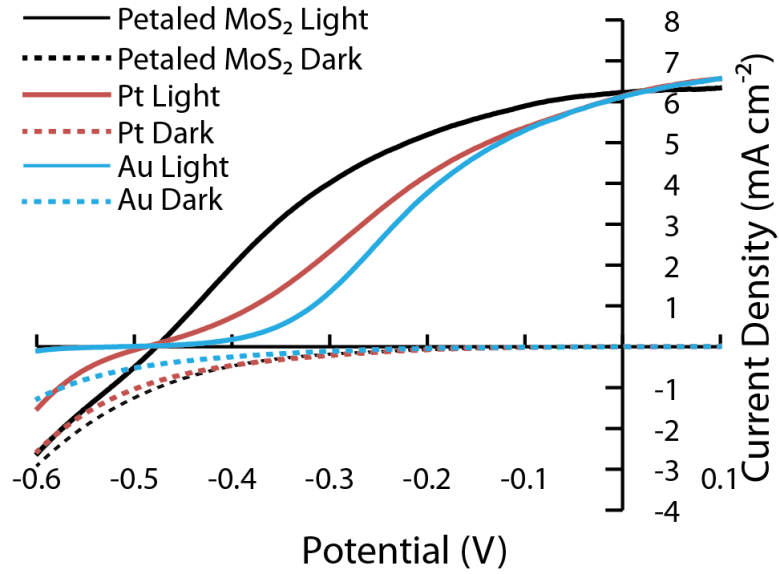
Figure 7. Current-potential curves in the dark and under illumination of devices using Pt or petaled MoS$_2$ cathode.

Table 1. Solar Cell Characteristics

Cathode	J_{sc} (mA cm^{-2})	V_{oc} (V)	*FF*	η
Petaled MoS$_2$	6.22	0.477	0.41	1.21%
Pt	6.13	0.489	0.29	0.85%
Au	6.12	0.517	0.24	0.75%

Comparing experimental QDSSC results, petaled MoS$_2$ outperforms both Pt and Au as a cathode

material. In Figure 8, when either device is not illuminated, the current becomes increasingly cathodic as the

potential is swept to negative values. Under illumination, however, the curve is shifted up on the current axis so

that a photovoltaic current is being produced. The device employing petaled MoS$_2$ as a cathode produces more

photovoltaic current and has overall superior cell characteristics to the devices employing a Pt or Au cathodes.

The primary improvement of petaled MoS$_2$ over Pt and Au is in the fill factor (*FF*), arising from decreased

series resistance in petaled MoS_2 which indicates more ideal behavior of the overall device as a DC power source.[39] This provides further evidence that petaled MoS_2 can act catalytically in the electroreduction of polysulfide. A low fill factor severely limits the maximum power that can be produced by solar devices. Specifically, *FF* values of ~0.25 (0.29 and 0.24 for Pt and Au, respectively) indicate that the device is behaving like a resistor; this is improved by switching to a petaled MoS_2 electrode.
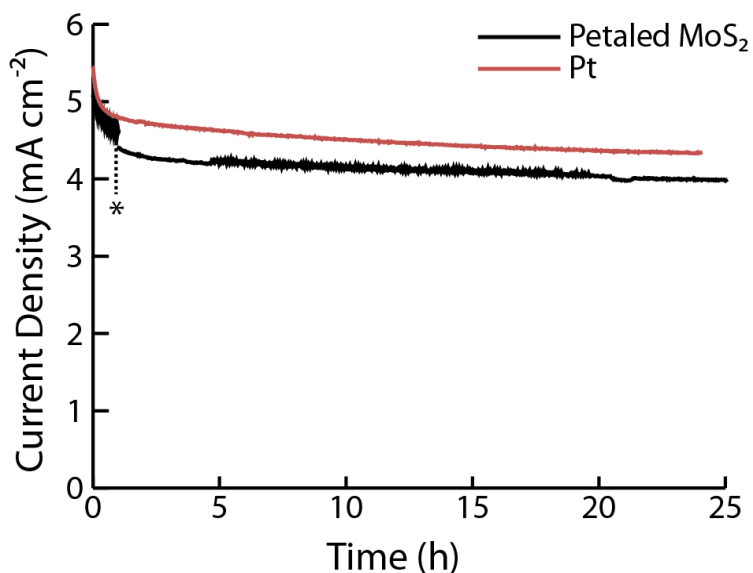
Figure 8. Chronoamperometric study of an illuminated QDSSC device using Pt (red line) or petaled MoS_2 (black line) as a cathode. *At this point, the device was removed from the measurement apparatus and rested 1 h while another measurement was being taken, then illuminated for an additional 24h.

Table 2. Solar Cell Characteristics before and after long illumination.

Cathode	J_{sc} (mA cm^{-2})	V_{oc} (V)	*FF*	η
Petaled MoS_2	5.71	0.491	0.39	1.08%
Post 25h illum.	4.29	0.475	0.26	0.53%
Pt	6.13	0.489	0.29	0.85%
Post 24h illum.	4.17	0.471	0.28	0.54%

When studying the cell photocurrent over 24 h, after an initial decay in the first 2h, the photocurrent became steady indicating both that the cathode was stable and that at long periods, other series resistances

become dominant in the working cell (Figure 8 and Table 2). There is also some improvement in J_{sc}, which is significant because cathode improvement is expected to increase current flowing through the device, since there would be less resistance as a result of cathode poisoning. V_{oc} is not enhanced by petaled MoS$_2$, which indicates improved interaction of the Pt or Au cathode Fermi level and electrolyte redox potential with the photoanode. Finally, petaled MoS$_2$ achieves at least 140% the cell efficiency of cells prepared with either Pt or Au cathodes, which is very promising for the utilization of this material in commercial solar cells.

Conclusions

In conclusion, we have developed a facile hydrothermal synthesis to prepare petaled MoS$_2$, a highly active and inexpensive cathode material for polysulfide reduction in QDSSCs and HER. The synthesis produced a uniform layer of catalytically active edges grown perpendicular to the Mo precursor and substrate, which would be beneficial for a variety of applications requiring the catalytic capability of MoS$_2$, including HER and HDS. Electrochemical studies showed that petaled MoS$_2$ electrodes are active for HER and are more catalytically active for polysulfide reduction than Pt, far surpassing the current densities achieved with commonly used Pt electrodes. Quantum dot sensitized solar cells were constructed and tested, increasing greatly in efficiency simply by switching from a Pt cathode to a petaled MoS$_2$ cathode.

References

(1)   Yu, W. W.; Qu, L.; Guo, W.; Peng, X. Experimental Determination of the Extinction Coefficient of CdTe, CdSe, and CdS Nanocrystals. *Chem. Mater.* **2003**, *15* (14), 2854–2860.

(2)   Etgar, L. Semiconductor Nanocrystals as Light Harvesters in Solar Cells. *Materials (Basel).* **2013**, *6* (2), 445–459.

(3)   Jun, H. K.; Careem, M. A.; Arof, A. K. Quantum Dot-Sensitized Solar Cells-Perspective and Recent Developments: A Review of Cd Chalcogenide Quantum Dots as Sensitizers. *Renew. Sustain. Energy Rev.* **2013**, *22*, 148–167.

(4)   Rühle, S.; Shalom, M.; Zaban, A. Quantum-Dot-Sensitized Solar Cells. *ChemPhysChem* **2010**, *11* (11), 2290–2304.

(5)   Faber, M. S.; Park, K.; Cabán-Acevedo, M.; Santra, P. K.; Jin, S. Earth-Abundant Cobalt Pyrite (CoS_2) Thin Film on Glass as a Robust, High-Performance Counter Electrode for Quantum Dot-Sensitized Solar Cells. *J. Phys. Chem. Lett.* **2013**, *4* (11), 1843–1849.

(6)   Radich, J. G.; Dwyer, R. P.; Kamat, P. V. Cu_2S Reduced Graphene Oxide Composite for High-Efficiency Quantum Dot Solar Cells. Overcoming the Redox Limitations of S^{2-}/S_n^{2-} at the Counter Electrode. *J. Phys. Chem. Lett.* **2011**, *2* (19), 2453–2460.

(7)   Zhu, G.; Pan, L.; Sun, H.; Liu, X.; Lv, T.; Lu, T.; Yang, J.; Sun, Z. Electrophoretic Deposition of a Reduced Graphene-Au Nanoparticle Composite Film as Counter Electrode for Cds Quantum Dot-Sensitized Solar Cells. *ChemPhysChem* **2012**, *13* (3), 769–773.

(8)   Yeh, M. H.; Lee, C. P.; Chou, C. Y.; Lin, L. Y.; Wei, H. Y.; Chu, C. W.; Vittal, R.; Ho, K. C. Conducting Polymer-Based Counter Electrode for a Quantum-Dot-Sensitized Solar Cell (QDSSC) with a Polysulfide Electrolyte. *Electrochim. Acta* **2011**, *57* (1), 277–284.

(9)   Tachan, Z.; Shalom, M.; Hod, I.; Rühle, S.; Tirosh, S.; Zaban, A. PbS as a Highly Catalytic Counter Electrode for Polysulfide-Based Quantum Dot Solar Cells. *J. Phys. Chem. C* **2011**, *115* (13), 6162–6166.

(10)   Deng, M.; Zhang, Q.; Huang, S.; Li, D.; Luo, Y.; Shen, Q.; Toyoda, T.; Meng, Q. Low-Cost Flexible Nano-Sulfide/Carbon Composite Counter Electrode for Quantum-Dot-Sensitized Solar Cell. *Nanoscale Res. Lett.* **2010**, *5* (6), 986–990.

(11)   Pan, Z.; Zhao, K.; Wang, J.; Zhang, H.; Feng, Y.; Zhong, X. Near Infrared Absorption of CdSe X Te 1-X Alloyed Quantum Dot Sensitized Solar Cells with More than 6% Efficiency and High Stability. *ACS Nano* **2013**, *7* (6), 5215–5222.

(12) Hodes, G.; Manassen, J. Electrocatalytic Electrodes for the Polysulfide Redox System. *J. Electrochem. Soc.* **1980**, *127* (3), 544.

(13) Chhowalla, M.; Shin, H. S.; Eda, G.; Li, L.-J.; Loh, K. P.; Zhang, H. The Chemistry of Two-Dimensional Layered Transition Metal Dichalcogenide Nanosheets. *Nat. Chem.* **2013**, *5* (4), 263–275.

(14) Newaz, A. K. M.; Prasai, D.; Ziegler, J. I.; Caudel, D.; Robinson, S.; Haglund Jr., R. F.; Bolotin, K. I. *Electrical Control of Optical Properties of Monolayer MoS$_2$*; 2013; Vol. 155.

(15) Liu, C.-J.; Tai, S.-Y.; Chou, S.-W.; Yu, Y.-C.; Chang, K.-D.; Wang, S.; Chien, F. S.-S.; Lin, J.-Y.; Lin, T.-W. Facile Synthesis of MoS$_2$/graphene Nanocomposite with High Catalytic Activity toward Triiodide Reduction in Dye-Sensitized Solar Cells. *J. Mater. Chem.* **2012**, *22* (39), 21057.

(16) Sekine, T.; Julien, C.; Samaras, I.; Jouanne, M.; Balkanski, M. Vibrational Modifications on Lithium Intercalation in MoS$_2$. *Mater. Sci. Eng. B* **1989**, *3* (1), 153–158.

(17) Topsøe, H.; Clausen, B. S.; Massoth, F. E. Hydrotreating Catalysis. In *Catalysis*; Springer: Berlin, Heidelberg, 1996; pp 1–269.

(18) Enyashin, A.; Gemming, S.; Seifert, G. Nanosized Allotropes of Molybdenum Disulfide. *Eur. Phys. J. Spec. Top.* **2007**, *149*, 103–125.

(19) Kibsgaard, J.; Chen, Z.; Reinecke, B. N.; Jaramillo, T. F. Engineering the Surface Structure of MoS$_2$ to Preferentially Expose Active Edge Sites for Electrocatalysis. *Nat. Mater.* **2012**, *11* (11), 963–969.

(20) Kong, D.; Wang, H.; Cha, J. J.; Pasta, M.; Koski, K. J.; Yao, J.; Cui, Y. Synthesis of MoS$_2$ and MoSe$_2$ Films with Vertically Aligned Layers. *Nano Lett.* **2013**, *13* (3), 1341–1347.

(21) Huang, W.; Xu, Z.; Liu, R.; Ye, X.; Zheng, Y. Tungstenic Acid Induced Assembly of Hierarchical Flower-like MoS$_2$ Spheres. *Mater. Res. Bull.* **2008**, *43* (10), 2799–2805.

(22) Cao, F.; Hu, W.; Zhou, L.; Shi, W.; Song, S.; Lei, Y.; Wang, S.; Zhang, H. 3D Fe$_3$S$_4$ Flower-like Microspheres: High-Yield Synthesis via a Biomolecule-Assisted Solution Approach, Their Electrical, Magnetic and Electrochemical Hydrogen Storage Properties. *Dalt. Trans.* **2009**, *105* (42), 9246.

(23) Zhigang, T.; Qian, Z.; Xunzhi, G.; Jin-Fu, Z.; Wen-Yong, W.; Ai-Ping, L. Synthesis of Flower-Shaped

CuS Microsphere Superstructures by a Solvothermal Route and Its Photocatalytic Properties. *Acta Chim. Sin.* **2011**, *69* (23), 2812–2820.

(24)   Wang, Q.; Jiao, L.; Du, H.; Peng, W.; Han, Y.; Song, D.; Si, Y.; Wang, Y.; Yuan, H. Novel Flower-like CoS Hierarchitectures: One-Pot Synthesis and Electrochemical Properties. *J. Mater. Chem.* **2011**, *21* (2), 327–329.

(25)   Liang, H.; Meng, F.; Cabán-Acevedo, M.; Li, L.; Forticaux, A.; Xiu, L.; Wang, Z.; Jin, S. Hydrothermal Continuous Flow Synthesis and Exfoliation of NiCo Layered Double Hydroxide Nanosheets for Enhanced Oxygen Evolution Catalysis. *Nano Lett.* **2015**, *15* (2), 1421–1427.

(26)   Chen, X.; Li, H.; Wang, S.; Yang, M.; Qi, Y. Biomolecule-Assisted Hydrothermal Synthesis of Molybdenum Disulfide Microspheres with Nanorods. *Mater. Lett.* **2012**, *66* (1), 22–24.

(27)   Wu, C.; Xie, Y. A New Synergic-Assembly Strategy Towards Three-Dimensional (3D) Hollow Nanoarchitectures. *J. Nanosci. Nanotechnol.* **2008**, *8* (12), 6208–6222.

(28)   Ye, L.; Guo, W.; Yang, Y.; Du, Y.; Xie, Y. Directing the Architecture of Various MoS_2 Hierarchical Hollow Cages through the Controllable Synthesis of Surfactant/molybdate Composite Precursors. *Chem. Mater.* **2007**, *19*, 6331–6337.

(29)   Bertrand, P. A. Surface-Phonon Dispersion of MoS_2. *Phys. Rev. B* **1991**, *44* (11), 5745–5749.

(30)   Li, H.; Zhang, Q.; Yap, C. C. R.; Tay, B. K.; Edwin, T. H. T.; Olivier, A.; Baillargeat, D. From Bulk to Monolayer MoS_2: Evolution of Raman Scattering. *Adv. Funct. Mater.* **2012**, *22* (7), 1385–1390.

(31)   Wang, Q. H.; Kalantar-Zadeh, K.; Kis, A.; Coleman, J. N.; Strano, M. S. Electronics and Optoelectronics of Two-Dimensional Transition Metal Dichalcogenides. *Nat. Nanotechnol.* **2012**, *7* (11), 699–712.

(32)   Lee, C.; Yan, H.; Brus, L. E.; Heinz, T. F.; Hone, J.; Ryu, S. Anomalous Lattice Vibrations of Single- and Few-Layer MoS_2. *ACS Nano* **2010**, *4* (5), 2695–2700.

(33)   Gong, Q.; Cheng, L.; Liu, C.; Zhang, M.; Feng, Q.; Ye, H.; Zeng, M.; Xie, L.; Liu, Z.; Li, Y. Ultrathin $MoS_{2(1-x)}Se_{2x}$ Alloy Nanoflakes For Electrocatalytic Hydrogen Evolution Reaction. *ACS Catal.* **2015**, *5*, 2213–2219.

(34) Sun, D.; Feng, S.; Terrones, M.; Schaak, R. E. Formation and Interlayer Decoupling of Colloidal $MoSe_2$ Nanoflowers. *Chem. Mater.* **2015**, *27*, 3167–3175.

(35) Tonndorf, P.; Schmidt, R.; Böttger, P.; Zhang, X.; Börner, J.; Liebig, A.; Albrecht, M.; Kloc, C.; Gordan, O.; Zahn, D. R. T.; Michaelis De Vasconcellos, S.; Bratschitsch, R. Photoluminescence Emission and Raman Response of Monolayer MoS_2, $MoSe_2$, and WSe_2. *Opt. Express* **2013**, *21* (4), 4908–4916.

(36) Lafuente, B.; Downs, R. T.; Yang, H.; Stone, N. The Power of Databases: The RRUFF Project. In *Highlights in Mineralogical Crystallography*; Armbruster, T., Danisi, R. M., Eds.; W. De Gruyter: Berlin, 2015; pp 1–30.

(37) Kim, J.; Choi, H.; Nahm, C.; Kim, C.; Nam, S.; Kang, S.; Jung, D.-R.; Kim, J. I.; Kang, J.; Park, B. The Role of a $TiCl_4$ Treatment on the Performance of CdS Quantum-Dot-Sensitized Solar Cells. *J. Power Sources* **2012**, *220*, 108–113.

(38) Vesce, L.; Riccitelli, R.; Soscia, G.; Brown, T. M.; Di Carlo, A.; Reale, A. Optimization of Nanostructured Titania Photoanodes for Dye-Sensitized Solar Cells: Study and Experimentation of $TiCl_4$ Treatment. *J. Non. Cryst. Solids* **2010**, *356* (37–40), 1958–1961.

(39) Ashok, S.; Pande, K. P. Photovoltaic Measurements. *Sol. Cells* **1985**, *14*, 61–81.

Contact and support considerations in the HER activity of petaled MoS$_2$ electrodes.[*]
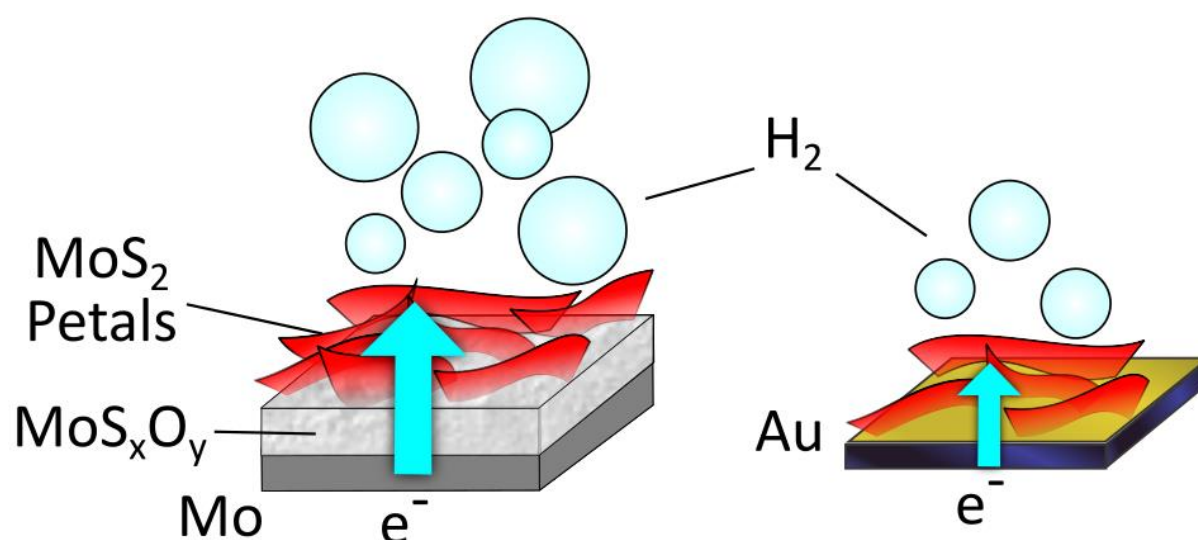
Introduction

      The high activity and earth-abundant elemental composition of molybdenum disulfide (MoS$_2$) makes it an attractive replacement for platinum and other precious metals in electrocatalytic applications. MoS$_2$ has been identified as a highly active electrocatalyst for the hydrogen evolution reaction (HER)[1] and polysulfide reduction in quantum dot sensitized solar cells (QDSSCs), as shown in the previous chapter.[2] Exposed edges of the layers and defect terrace sites have been identified as the active sites for the HER[3,4] and, as a result,

---

significant research efforts have been devoted to preparing MoS_2 architectures on electrode surfaces which expose these edges as well as inducing defect sites on the S-terminated faces.[4–6]

As described in Chapter II, I developed a synthesis for nanostructured MoS_2 electrodes in one step, directly from a Mo foil support, which exposes a high number of catalytic edge sites. As a result, the planar foils can be immediately employed as an electrode without the use of binders or other support materials. These "petaled" MoS_2 (P. MoS_2) (**Figure 1**a, b and **Scheme 1**a) foils performed excellently as an inexpensive and highly active electrode material towards polysulfide reduction in liquid-junction QDSSCs.[2] Other groups have developed synthetic methodologies where metallic Mo is converted to MoS_2 and supported onto electrodes of carbon fibers, fluorine-doped SnO_2 (FTO), etc., but additional steps are required in these syntheses.[5,7,8] These preparations are very exciting low-cost methods for preparing highly active MoS_2 catalysts.
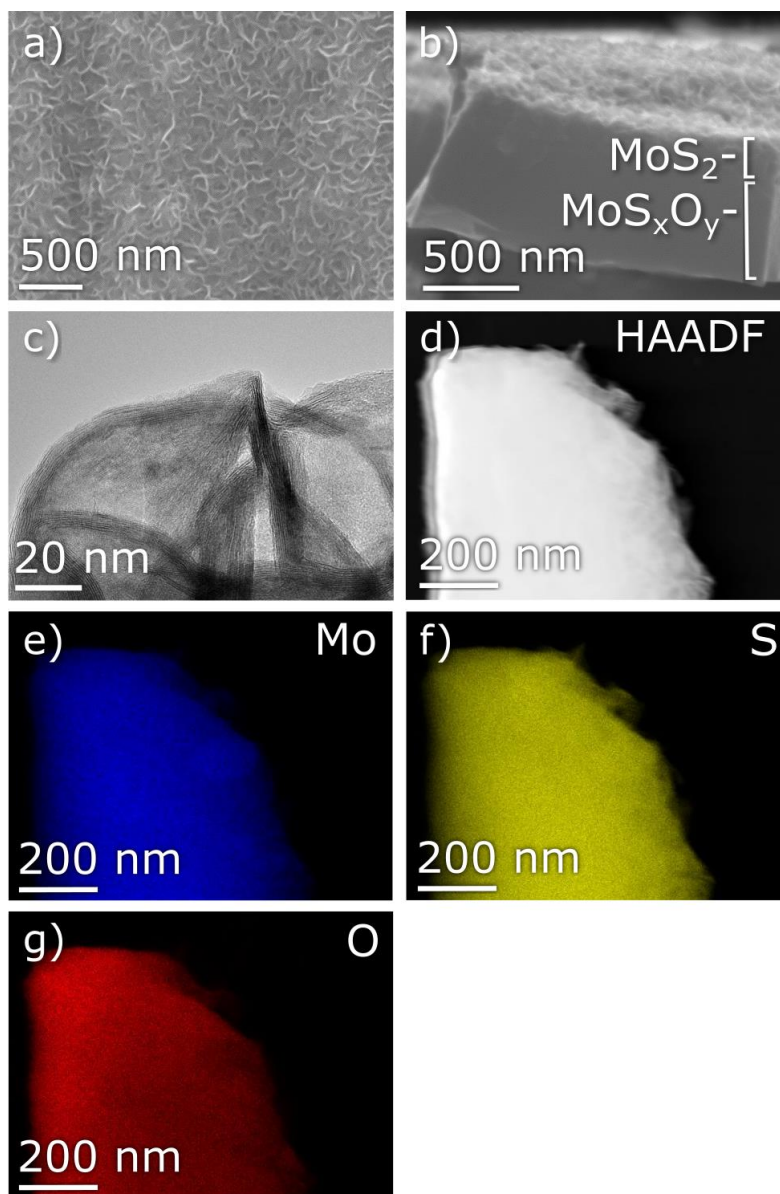
Figure 1. Characterization of petaled MoS_2/Mo. a) Top-down and b) cross-sectional SEM images of exfoliated (b only) P. MoS_2/Mo revealing the intermediate MoS_xO_y layer. The interface occurs at the transition between the high-texture MoS_2 and low-texture MoS_xO_y regions. c) TEM image of P. MoS_2 synthesized on Mo aperture grid. d) High-angle annular dark field (HAADF) TEM image of exfoliated P. MoS_2/Mo cross-section (the flat bottom of the MoS_xO_y layer is on the left and the top of the MoS_2 petals are on the right) with corresponding EDS maps of e) Mo (blue), f) S (yellow), and g) O (red). Each elemental map is normalized to its respective maximum signal.

45

Scheme 1. Synthesis of P. MoS$_2$ electrodes using a) Mo foil or b) Au/Si as a substrate.
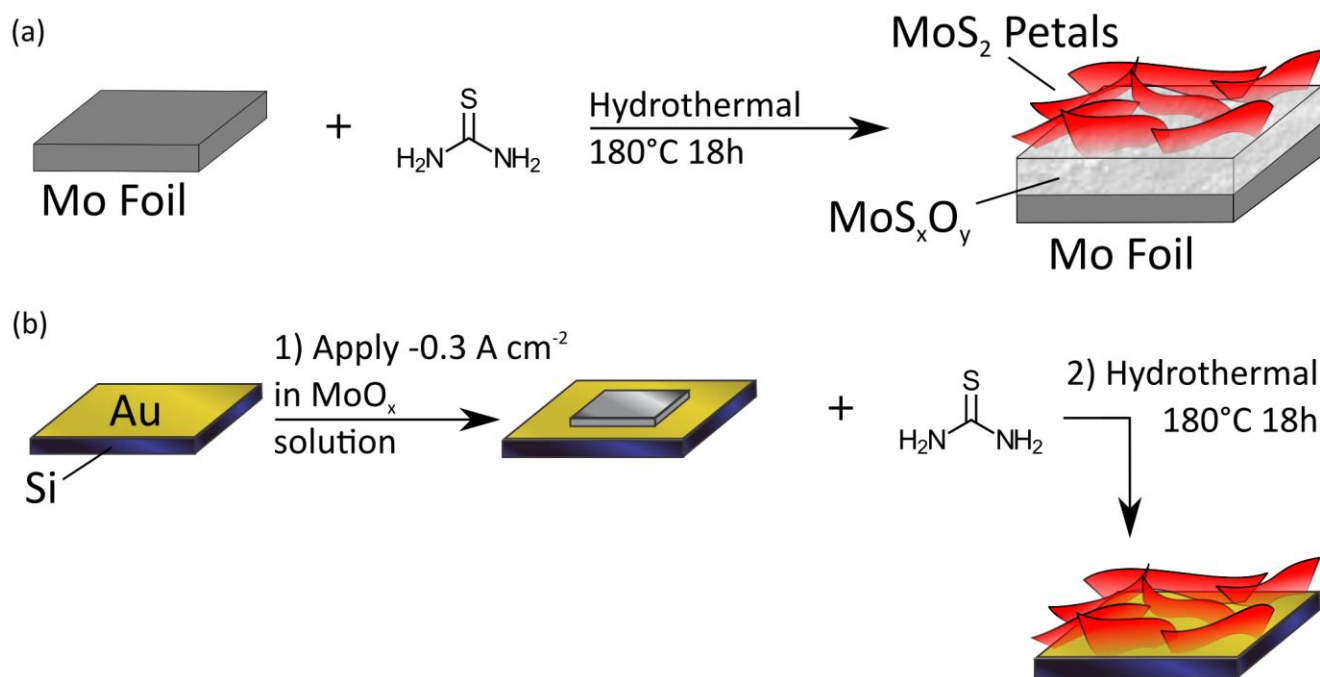
The role of the contact between the MoS$_2$ and its support material towards the function of the electrode has yet to be fully characterized, but previous work in other areas has shown that the support is integral to activity. The effect of the support for hydrodesulfurization on MoS$_2$ has been well-studied, and has shown that strong Mo-O- bonds to metal oxide supports hinder the inherent activity of the material.[9] Both computational and experimental work with single- or few-layer MoS$_2$ in transistor designs, which highlight the fundamental roles of interfacial band-bending phenomena and in-plane conductivity of layered MoS$_2$,[10–12] imply that the material choice and directionality of the MoS$_2$-support contact are important to function. Such experimental work has not been carried out for MoS$_2$ electrodes, where refining the design of the MoS$_2$ to expose catalytic edge sites has been a main focus, but perfecting the support material has not yet been considered.

We will describe here that an intermediate MoS$_x$O$_y$ layer forms between the Mo Foil and the P. MoS$_2$ in our hydrothermal preparation of electrodes (Figure 1b) and may be formed in other hydrothermal preparations of MoS$_2$. Intermediate oxides of Al$_2$O$_3$ and TiO$_2$ (~1 nm thick)[13] have been shown to ameliorate contacts between metals and MoS$_2$ by preventing Fermi level pinning, and MoO$_x$ has been shown to be an ideal contact material for hole injection.[14,15] It is yet unclear whether the very thick (~800 nm), intermediate MoS$_x$O$_y$ layer is

a barrier to electron conduction for a pure catalytic reaction on P. MoS$_2$ or similarly if other support materials may provide junctions that hinder the free flow of electrons to the MoS$_2$ surface.

To this end, we present a first experimental study on the role of the support contact and intermediate layers on the function of MoS$_2$ electrodes in catalytic HER. Because catalysis is presumed to occur solely at the edges of the MoS$_2$ petals, the study of the HER reaction isolates electronic effects such as barrier resistances from reactivity. We developed a synthesis to prepare P. MoS$_2$ directly on an Au contact (P. MoS$_2$/Au), which does not have the intermediate MoS$_x$O$_y$ layer. We compare the two electrode designs – P. MoS$_2$/Mo and P. MoS$_2$/Au - to understand the role of the contact on electrode function.

Experimental

All chemicals were obtained from Sigma-Aldrich unless otherwise noted and all water was purified using Millipore Direct-Q3 System to 18.2 MΩ·cm resistivity. "OAc" = "acetate."

Electrode Synthesis

P. MoS$_2$/Au electrodes were prepared by electroplating Mo onto Au/Si (100 nm Au evaporated onto 5 nm Cr, evaporated onto intrinsic Si) substrates, then exposing them to the same reaction conditions as P. MoS$_2$/Mo. The Mo deposition solution was prepared by combining Na$_2$MoO$_4$ (0.075 mmol), KOAc (365 mmol), NH$_4$OAc (365 mmol), and water (1.39 mol) in a beaker, stirred and heated until dissolved. The solution pH was then adjusted to 6.6 using acetic acid and ammonium hydroxide, while carefully adding small amounts of water to maintain solubility. The Au/Si substrate was prepared for Mo deposition by marking off an active area using Surlyn® (McMaster-Carr) adhesive tape. The electrode was then clipped to a double alligator clip apparatus (made in-house) along with a Pt Mesh electrode; the electrodes were separated by ~6 mm. The deposition solution was heated to 30°C with stirring at a rate low enough that the surface was not disturbed by

the vortex, but high enough that any bubbles formed could quickly escape the working electrode surface. The double alligator clip apparatus was connected to the appropriate electrode leads, suspended in the stirring deposition solution, and -300 mA cm^{-2} was applied for 30 min The electrode was rinsed and cut to fit in the bottom of the autoclave (~1.5 x 1.5 cm^2 or 1 x 2 cm^2), then subjected to the same reaction conditions as P. MoS_2/Mo.

Characterization

P. MoS_2 electrodes were characterized using Raman spectroscopy (Thermo Scientific DXR Raman Microscope) to confirm presence of MoS_2 and XPS (Physical Electronics (PHI) VersaProbe 5000) to analyze the chemical nature of the surface.

XPS data were collected using Al Kα X-rays (1486 eV), a takeoff angle of 45, and a spot size of 100 μm. Peaks were fitted using CasaXPS software, with the adventitious C 1s peak calibrated to 284.8 eV. In the Mo 3d and S 2p spectra, the separation of the spin-orbit couples were set to 3.2 and 1.15 eV, respectively; the peak areas were constrained to ratios of 3:2 and 2:1, respectively. The full-width at half maximum of each peak was constrained to between 0.6 and 2.4 eV, according to the band-pass of the instrument. In order to measure the underside of P. MoS_2 films, electrodes were scored using a diamond scribe into a grid pattern, then exfoliated using adhesive tape.

Electrodes were imaged using SEM (Zeiss® Merlin Gemini II) and TEM (FEI™ Tecnai Osiris). SEM and TEM images were analyzed for petal edge length density and width using ImageJ (NIH) software.

The height of Mo electrodeposited onto Au, as well as surface roughness of various electrodes, were measured with a Stylus Profilometer (Veeco® Dektak 150).

Electrochemical Measurements

Linear sweep voltammetry (LSV) and potentiostatic electrochemical impedance spectroscopy (EIS) were used to measure the HER activity of electrodes (Gamry Series G 300 with PHE200 & EIS300 Software Packages). 0.5 M H_2SO_4 solution was prepared and purged with N_2 for at least 20 min. Electrodes were submerged into 0.5M H_2SO_4 along with an Ag/AgCl reference electrode (saturated KCl) and Pt mesh counter electrode. The solution was stirred rapidly with the working electrode close in proximity to the magnetic stir bar, to remove bubbles from electrode surface, and with a nitrogen needle suspended over the surface of the solution. LSVs were measured from 0 – (-0.75) V vs. Ag/AgCl at a scan rate of 50 mV s^{-1} and 1 mV voltage step, then immediately measured with EIS. Open-circuit voltage was measured until it reached a stability of 2 mV min^{-1}, then EIS spectra taken from 100 kHz - 100 mHz at -250 mV vs. RHE DC voltage, 5 mV AC Voltage. Once the uncompensated resistance (R_u) was obtained from EIS measurement and modeling, it was used to compensate ("iR compensation") the measured voltage at every data point for the potential drop (Ohm's Law: $V = IR$) across the solution according to

$$E_{Ag/AgCl} = E_{meas} - I_{meas} * R_u,$$

where $E_{Ag/AgCl}$ is the iR-compensated potential vs. Ag/AgCl, E_{meas} is the measured potential vs. Ag/AgCl, and I_{meas} is the measured cell current (A). $E_{Ag/AgCl}$ values were converted to the reversible hydrogen electrode (RHE) using the relation:

$$E_{RHE} = E_{Ag/AgCl} + 0.059 * pH + E^0_{Ag/AgCl},$$

where E_{RHE} is the calculated potential vs. RHE, respectively, pH is the measured pH value (typically ~0.3), and $E^0_{Ag/AgCl}$ is the formal reduction potential of Ag/AgCl (sat'd KCl), +0.197 V vs. NHE.[16]

Geometric electrode areas used for normalization of current density, exchange current density, resistivity, and double layer capacitance are as follows: Pt – 0.0314 cm^2, P. MoS_2/Mo – 2.25 cm^2, P. MoS_2/Au – 0.71 cm^2, Au – 0.994 cm^2, Mo – 2.25 cm^2.

Results & Discussion

Materials Synthesis and Characterization

P. MoS_2 on Mo foil (Figure 1) was prepared as described in Chapter II.[2] The surface of the Mo grows "petals" of multilayer sheets of MoS_2 standing perpendicular to the plane of the support. Cutting or bending the substrate exposes a ~800 nm thick intermediate layer between the Mo substrate and the MoS_2 petal structures (Figure 1b). X-ray photoelectron spectroscopic (XPS) surveys have revealed that this layer contains significant amounts of Mo, S, and O (**Figure 2**). High resolution (HR)-XPS analysis indicates that this layer exhibits mostly MoO_2 character and to a lesser extent, MoO_3 character (**Figure 3**b, d). The S 2p region of the MoS_xO_y measurement show the S signal is similar to that of the MoS_2 petals (Figure 3c). TEM-EDS mapping (Figure 1d-g) shows that the concentration of oxygen is larger deeper into the intermediate layer, and there is a gradient to sulfur-rich closer to the petaled MoS_2 surface. Glancing-angle X-ray diffraction (GAXRD, Figure 3a) shows that the intermediate layer is amorphous, as the diffractogram is dominated by the Mo support with only weak, broad reflections from the crystalline MoS_2 petals (Figure 3a, inset).
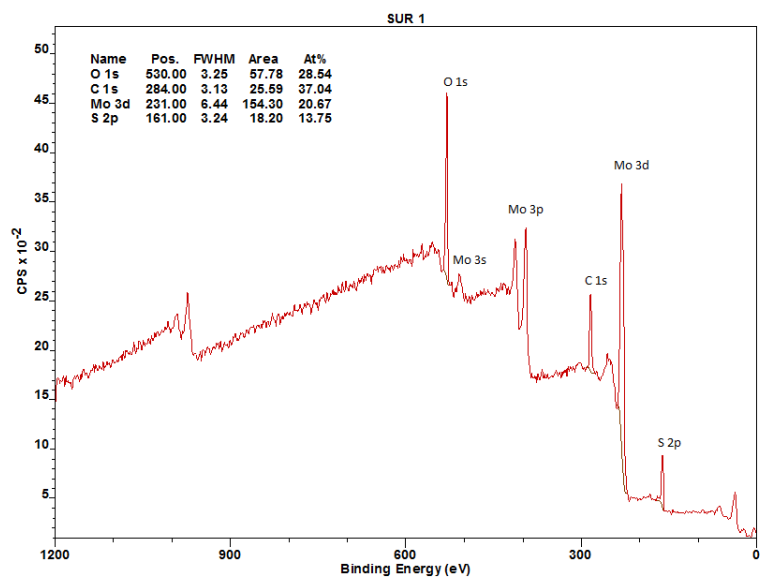
Figure 2. X-ray Photoelectron Spectroscopy (XPS) quantified survey region of the underside of exfoliated petaled MoS_2 material, revealing a mixture of Mo, O, and S.
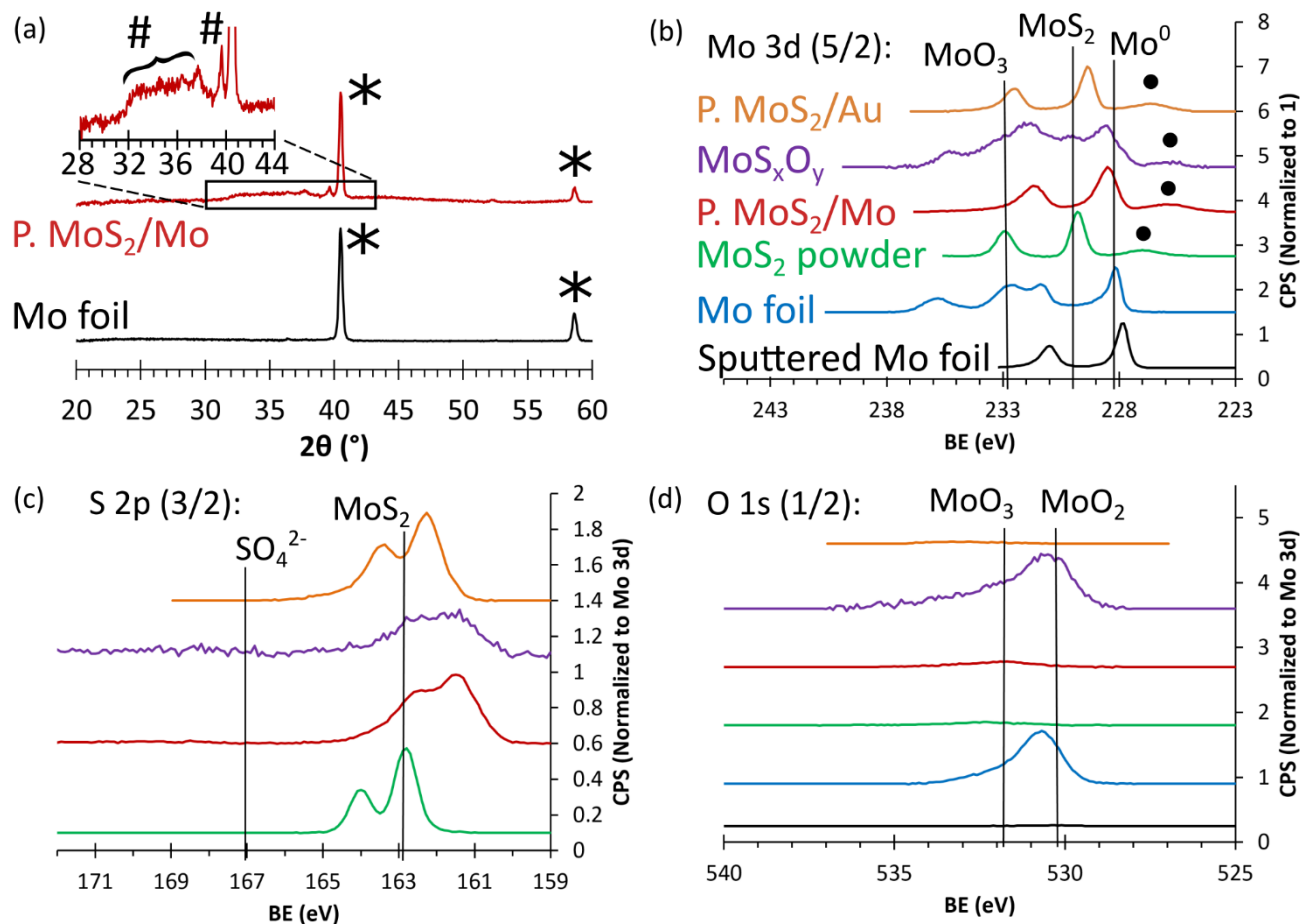
Figure 3. a) Glancing-angle X-ray diffractogram of P. MoS$_2$/Mo, where * denotes Mo (JCPDS Card No. 42-1120) reflections and # denotes 2H-MoS$_2$ (JCPDS Card No. 37-1492) reflections; inset: zoomed-in diffractogram of 2H-MoS$_2$ region. XPS spectra of P. MoS$_2$/Mo top and underside (MoS$_x$O$_y$), P. MoS$_2$/Au, MoS$_2$ powder, cleaned Mo foil (with native oxides present), and Sputtered Mo foil (sputtered for 10 min with Ar gas to remove oxides) in b) Mo 3d (● indicates S 2s peaks), c) S 2p, and d) O 1s regions. The color legend in b) also applies to c) and d). Vertical lines are included to show typical peak locations for selected species. Binding energies were corrected by matching the adventitious C 1s peak to 284.8 eV.

Other syntheses of nanostructured MoS$_2$, hydrothermal and otherwise, are known to go through an amorphous and/or Cn$_x$MoO$_y$X$_z$ (Cn = cation; X = halide) intermediate phase, depending on the precursors and synthesis conditions.[17–20] Therefore, we hypothesized that the formation of the P. MoS$_2$ film and intermediate layer proceed in the following manner: first, the Mo foil reacts with water to form amorphous surface oxides of mixed valence (MoO$_x$). The decomposition of thiourea at 177°C[21] then allows S to react with the Mo oxides to form both MoS$_x$O$_y$ and the P. MoS$_2$ structure on the surface. Since the petals are limited to ~200-300 nm in height, and there is an effectively infinite thickness of Mo in the Mo foil, we hypothesized that limiting the

thickness of Mo available to react to less than 300 nm would ensure complete conversion to MoS_2 petals and exclude the presence of the MoS_xO_y intermediate layer. In order to investigate the role that this intermediate layer plays on charge transfer in the electrodes, we developed a synthesis that would yield a product without this layer.

Therefore, a thin layer of metallic Mo was reductively electrodeposited[22] on support materials of Au/Si, Pt/Si and FTO/glass as these substrates are not affected by the hydrothermal conditions (Scheme 1b). Mo did not deposit on Pt due to HER competition during electrodeposition.[22] However, Mo was successfully electrodeposited on FTO and Au/Si (~225 nm, **Figure 4**) and subjected to a similar hydrothermal reaction to give P. MoS_2. Little to no P. MoS_2 was found on the FTO after the hydrothermal step, indicating poor adhesion of the product to the FTO. In contrast, ~250 nm-thick P. MoS_2 was successfully grown on Au/Si, as confirmed by scanning electron microscopy (SEM), Raman spectroscopy (**Figure 5**a-c) and XPS (**Figure 3**b-d). The petal density of P. MoS_2/Au (Figure 5a) is visibly less than that of P. MoS_2/Mo (Figure 1a). The root mean squared surface roughness (R_q) of P. MoS_2/Au was 220 nm (over 6 mm as measured by profilometry), whereas it was over three times larger (760 nm over 2 mm) for P. MoS_2/Mo. The electrodeposited films of Mo have a low R_q of 14.5 nm (over 6 mm) compared to the 742 nm (over 2 mm) R_q of Mo foil, which likely adversely affects the nucleation density in the hydrothermal synthesis to MoS_2 as well, providing much less real surface area for petal formation. The electrodes were cut and the cross section analyzed by SEM-EDS to compare the concentration of O (**Figure 6**). We found that no significant O signal was measured in P. MoS_2/Au as compared with P. MoS_2/Mo, confirming the absence of an intermediate MoS_xO_y layer in P. MoS_2/Au electrodes.
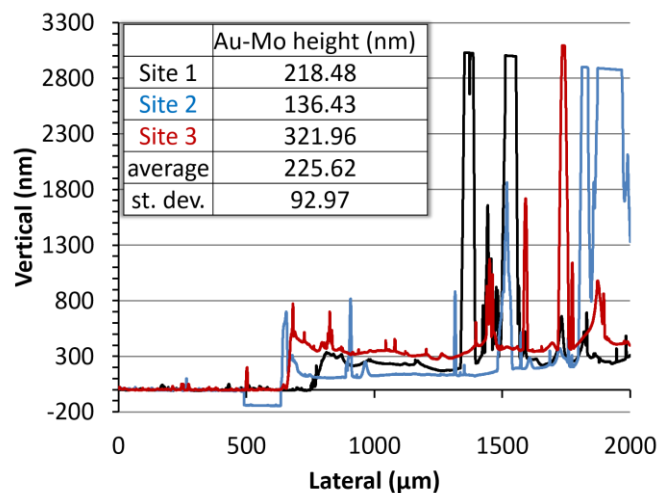
Figure 4. Profilometric scans of a typical Mo electrodeposition on Au, starting on Au, then scanning towards the Mo deposit. The dip below zero in the blue scan corresponds to a pit in the Au, exposing the Si substrate.
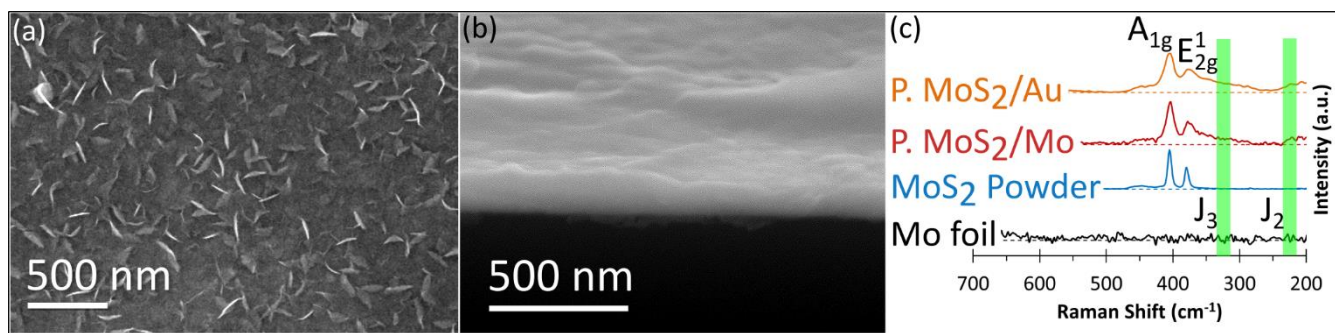
Figure 5. a) Top-down and b) cross-sectional SEM images of P. MoS_2/Au. c) Raman spectra of P. MoS_2/Au, P. MoS_2/Mo, MoS_2 Powder, and Mo foil; dashed lines represent the baseline for each respective measurement; green areas indicate expected 1T-MoS_2 frequencies.
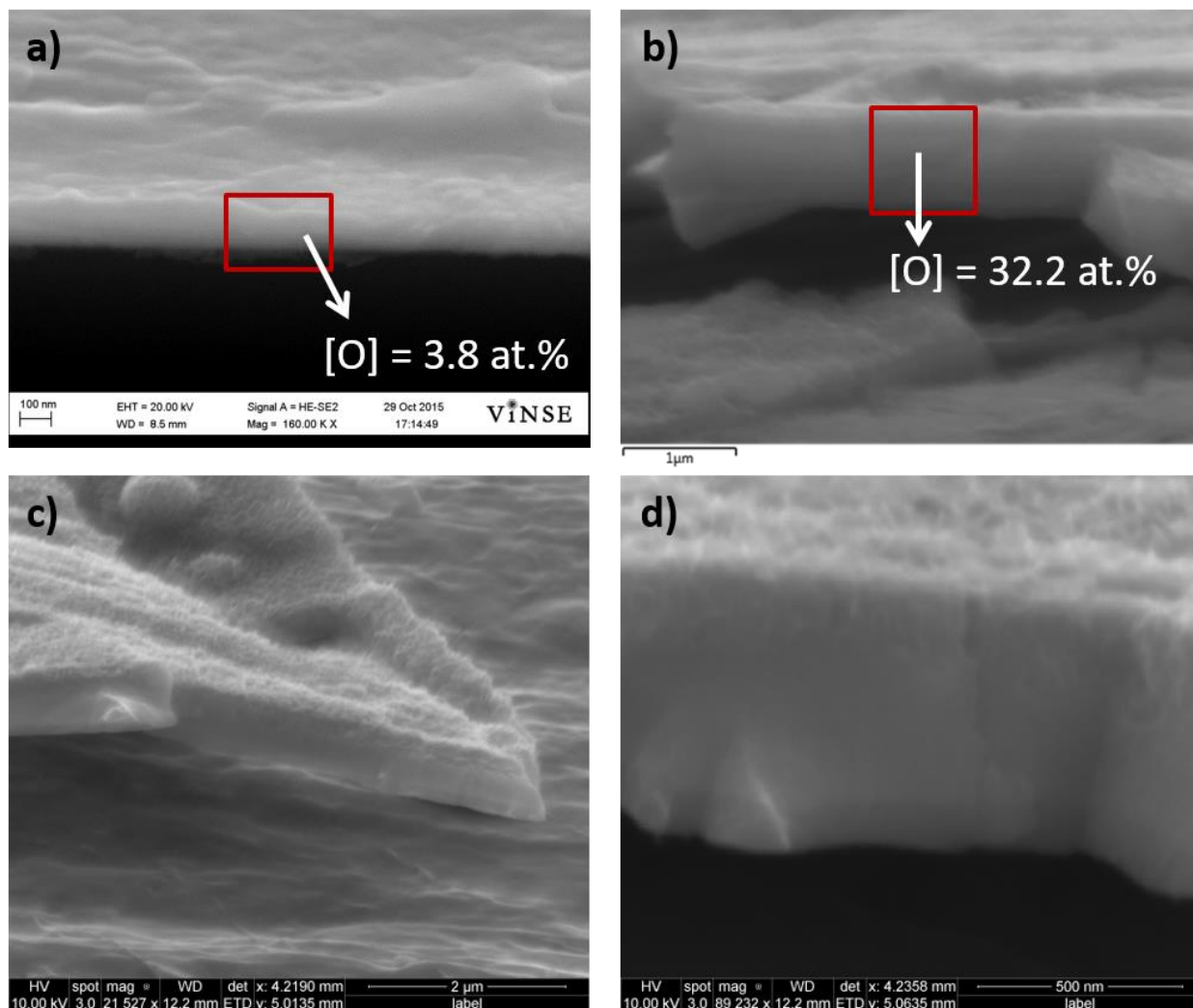
Figure 6. Cross-sectional images of a) P. MoS_2/Au and b-d) P. MoS_2/Mo. [O] corresponds to EDS oxygen content in the areas enclosed by red boxes. Additional images c) and d) included to highlight distinction between MoS_2 petals and intermediate MoS_xO_y layer.

Several materials characterization techniques reveal the single-layer nature of P. MoS_2. Both P. MoS_2/Mo and P. MoS_2/Au were found to exhibit non-zero Raman signals in regions associated with single-layer, $1T$-MoS_2.[23,24] Specifically, in the J_2 and J_3 regions at ~225 cm^{-1} and ~330 cm^{-1}, the spectra rise above the baseline, whereas the MoS_2 powder spectrum does not. The single-layer nature of the surface is also confirmed by XPS in Figure 3b-d, where the primary Mo 3d and S 2p peak pairs of P. MoS_2/Mo and P. MoS_2/Au are shifted to much lower binding energies (228.5 and 161.4 eV; 229.3 and 162.3 eV, respectively), compared with MoS_2 powder (229.8 eV and 162.8 eV, respectively).[25,26]. Such low binding energies of the Mo 3d and S2p peaks have been reported for metallic, $1T$-MoS_2.[23,27] Peak deconvolution of the XPS spectra (**Figure 7**) for P.

MoS$_2$/Mo reveals additional higher binding energy components in the Mo 3d and S 2p regions, which is more consistent with bulk MoS$_2$. XPS is a highly surface-sensitive technique, thus these results reflect the chemistry of the very edges of the petals. The TEM images (Figure 1c and **Figures 8** and **9**) of the petals show regions of multilayer MoS$_2$, but also regions of frayed single-layer MoS$_2$. The interlayer spacings (6.20-6.38 Å) are larger than the bulk (002) spacings (6.15Å) of 2H-MoS$_2$, indicating the chemistry is not entirely bulk-like, even in the multilayer regions. We collectively interpret these results to mean that the exposed edges of the petals tend to behave like single-layer MoS$_2$, possibly due to strain or fraying of the petal edges, whereas the deeper regions of the MoS$_2$ petals are more similar to bulk, multi-layer MoS$_2$.
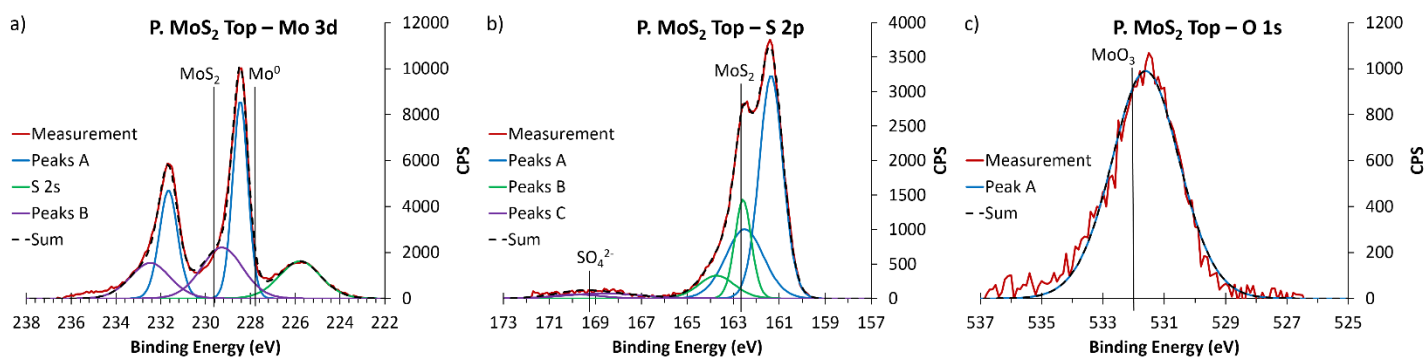
Figure 7. HR-XPS spectra of P. MoS$_2$/Mo with peak deconvolution using CasaXPS software. Reference peak positions (Mo 3d 5/2, S 2p 3/2, and O 1s 1/2) for relevant compounds are indicated by vertical lines (NIST XPS Database) for comparison to experimental data. For instance, the primary experimental Mo 3d 5/2 peak lies between the values for typical MoS$_2$ and Mo.
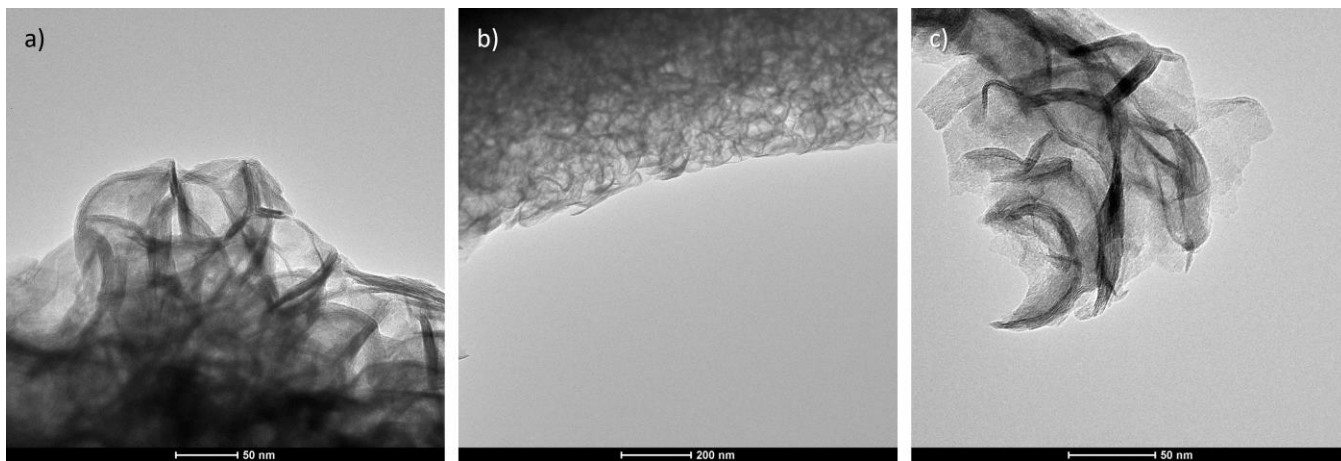
Figure 8. TEM images of P. MoS$_2$ grown from a Mo aperture grid used for measuring petal thickness: 6.7 nm $\pm$ 2.6 nm, n = 139. This corresponds to 11 S-Mo-S trilayers.
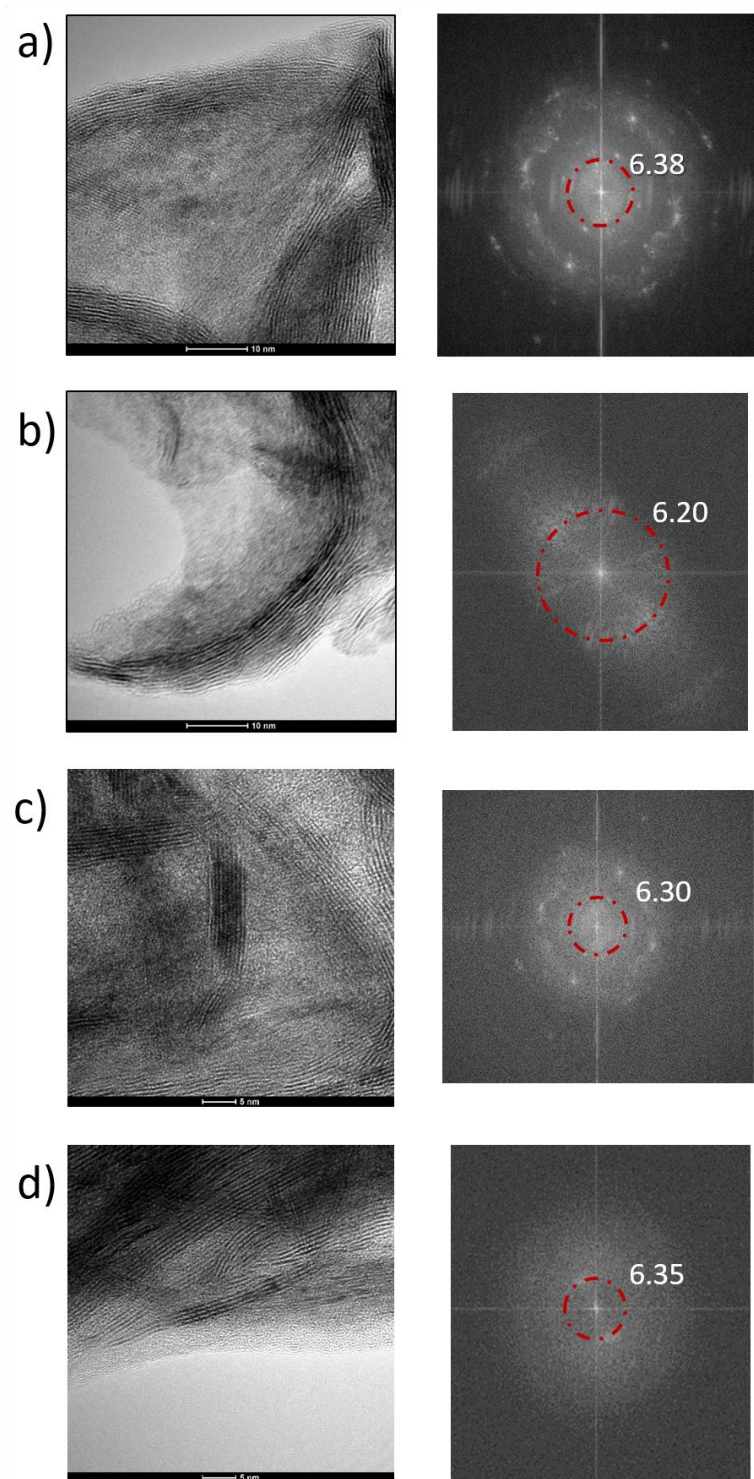
Figure 9. TEM images with corresponding FFT of P. MoS$_2$ synthesized on a Mo aperture grid. The red circles indicate the d-spacing assigned to the (002) reflection of 2H-MoS$_2$ (d = 6.15 Å, JCPDS Card No. 37-1492), with noticeably larger values than the card, likely due to fraying of the petal edges. TEM scale bars are 10 nm for a) and b), and 5 nm for c) and d).

Electrochemical Performance

P. MoS$_2$/Mo and P. MoS$_2$/Au were evaluated for HER activity using linear sweep voltammetry (LSV) and electrochemical impedance spectroscopy (EIS) in 0.5M H$_2$SO$_4$, as shown in **Figure 10**. Control measurements of Pt (the best known HER catalyst), Au, and Mo electrodes were also included. By comparing the overpotential (η) required to achieve -10 mA cm^{-2} with respect to geometric electrode area (see **Table 1**), the excellent catalytic activity of P. MoS$_2$ is highlighted, independent of its substrate. P. MoS$_2$/Mo exhibits an η of 242 mV and P. MoS$_2$/Au exhibits a larger value of 279 mV, which are comparable to those reported for other MoS$_2$ nanocatalysts.[28] LSV scans of P. MoS$_2$/Mo and P. MoS$_2$/Au show good HER activity as compared with their respective substrates: Au requires high η, indicating low HER activity, and Mo shows even lower HER activity as expected from the well-known volcano plots first published by Nørskov et al.[29]
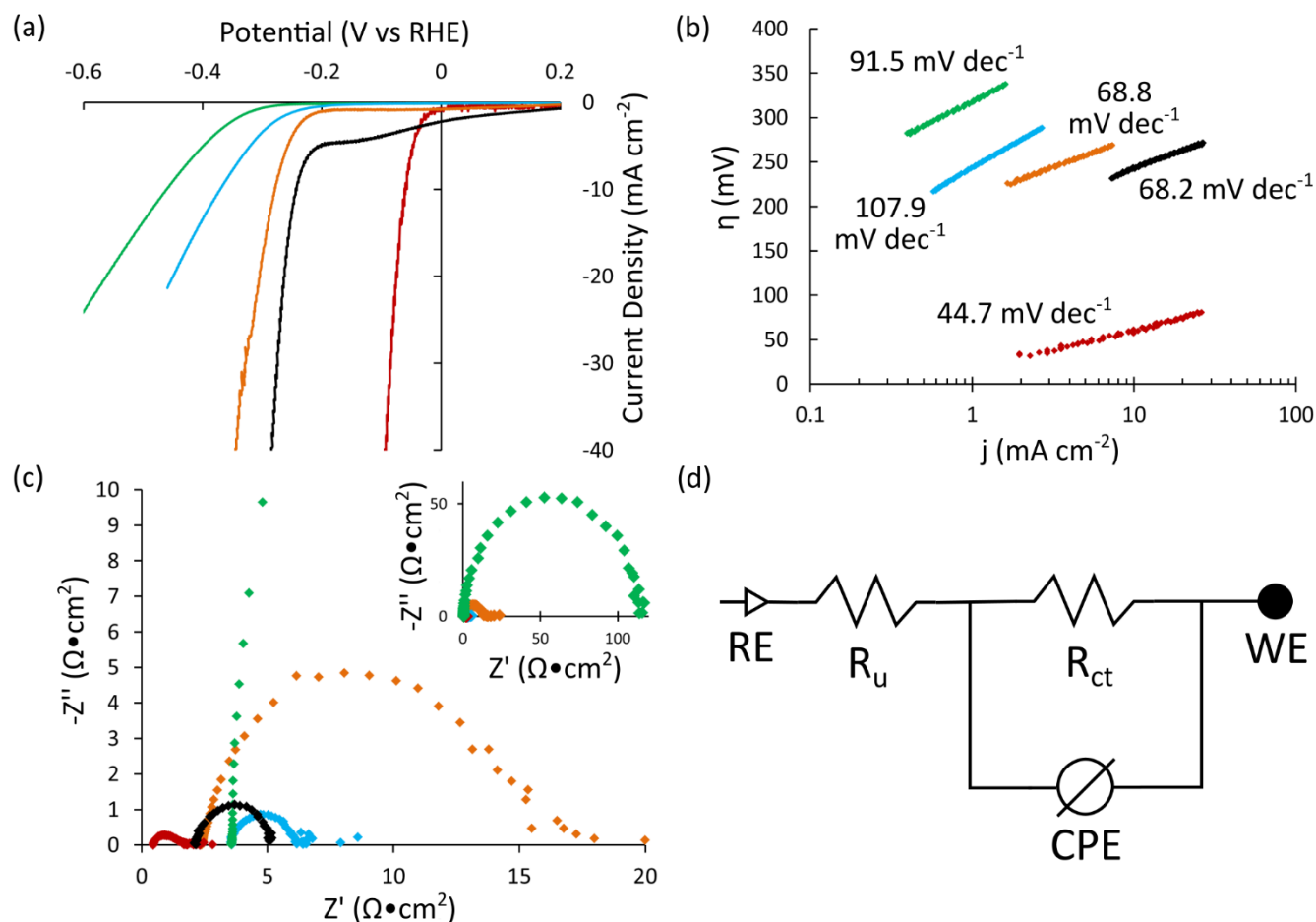
Figure 10. a) iR-corrected LSV measurements of electrodes: Pt (red), P. MoS$_2$/Mo (black), P. MoS$_2$/Au (orange), Au (blue), Mo (green). b) Tafel analysis of scans in (a) with Tafel slopes. c) Nyquist plots of electrodes at -250 mV vs. RHE, 5 mV amplitude; inset: large impedance regime of Mo foil. d) Equivalent circuit diagram of Randles cell used to fit EIS data, which was modified by removing the commonly used Warburg impedance component (diffusion in quiet solutions) and using a constant phase element (CPE) to account for non-ideal capacitive behavior.

Table 1. Comparison of relevant electrochemical values for electrodes tested.

Electrode	η to 10 mA cm^{-2} (mV vs. RHE)	$j_{0,geo}$ (mA cm^{-2})	$j_{0,real}$ (mA cm^{-2})	R_u (Ω·cm^2)	R_{ct} (Ω·cm^2)	C_{dl} (μF cm^{-2})
Pt	61.4	0.447	0.13	0.45	1.0	70.
P. MoS$_2$/Mo	242	0.00290	1.7×10^{-6}	2.2	3.4	1.7×10^4
P. MoS$_2$/Au	279	0.000921	5.9×10^{-6}	2.4	13	1.6×10^3
Au	371	0.00563	0.0021	3.6	3.0	54
Mo	459	0.000339	2.1×10^{-5}	3.6	110	330

The presence of Mo oxides in the P. MoS$_2$/Mo intermediate layer is evidenced in LSVs. In **Figure 10**a, both P. MoS$_2$ electrodes have similar HER onsets of ~200 mV vs. RHE. The P. MoS$_2$/Mo shows a significant

additional reductive current at potentials below +0.2 V vs. RHE, leading down to a plateau at -0.136 V. This additional reductive current is likely due to reduction in the MoS_xO_y intermediate layer, as the standard electrochemical potentials of several Mo oxides fall in this region:[21]

$$H_3Mo_7O_{24}{}^{3-} + 45\ H^+ + 42e^- \rightleftarrows 7\ Mo + 24\ H_2O \qquad\qquad E° = +0.082\ V \qquad\qquad \textbf{(1)}$$

$$MoO_3 + 6\ H^+ + 6\ e^- \rightleftarrows Mo + 3\ H_2O \qquad\qquad E° = +0.075\ V \qquad\qquad \textbf{(2)}$$

$$MoO_2 + 4\ H^+ + 4\ e^- \rightleftarrows Mo + 4\ H_2O \qquad\qquad E° = -0.152\ V \qquad\qquad \textbf{(3)}$$

The electrochemical evidence agrees with the HR-XPS results that the interfacial layer is mostly comprised of MoO_2, with small amounts of higher oxides that, from the XRD analysis, are amorphous.

The similar Tafel slopes of ~68 mV dec^{-1} for the two P. MoS$_2$ electrodes in Figure 10b demonstrate that P. MoS$_2$ catalyzes HER via the same mechanism independent of its substrate. The Tafel relationship is as follows:

$$slope = \frac{2.3RT}{(n' + \alpha)F} \qquad\qquad \textbf{(4)}$$

where R is the ideal gas constant, T is temperature, F is the Faraday constant, n' is the number of electrons transferred before the rate-determining step (RDS), and α is the charge transfer coefficient. The slope is an indicator of the RDS in the HER mechanism (Table 2).

Table 2. Component steps of the Hydrogen Evolution Reaction with characteristic Tafel Slopes.

Step	Reaction	Tafel slope if RDS	
Volmer	$H_3O^+ + e^- \rightarrow H_{ads}{}^* + H_2O$	120 mV dec^{-1}	**(5)**
Chemical Rearrangement	$H_{ads}{}^* \rightarrow H_{ads}$	60 mV dec^{-1}	**(6)**
Heyrovsky	$H_{ads} + H_3O^+ + e^- \rightarrow H_2$	42 mV dec^{-1}	**(7)**
Tafel	$H_{ads} + H_{ads} \rightarrow H_2 + H_2O$	30 mV dec^{-1}	**(8)**

There are several reports of MoS$_2$ electrodes that show Heyrovsky-limited HER.[30–34] Incomplete cubane clusters ([Mo$_3$S$_4$]$^{4+}$) showed Volmer-limited behavior with a Tafel slope of 120 mV dec^{-1}.[35] However, the slope of ~68 mV dec^{-1} observed here for P. MoS$_2$ lies between the characteristic Tafel slopes of 40 mV dec^{-1} and 120

mV dec^{-1} indicating that neither the Heyrovsky nor the Volmer steps, respectively, are rate-determining.[36] Several other nanostructured MoS$_2$ electrodes have shown intermediate Tafel slopes.[3,31,37–39] A Tafel slope of 60 mV dec^{-1} is an indicator instead that the RDS does not involve electron transfer (α =0) and it occurs after one electron has transferred (n'=1) in the overall mechanism. For HER, a Tafel slope near 60 mV dec^{-1} has been ascribed to a necessary rate-limiting chemical rearrangement of H on the surface before the second electron transfer.[40] Thus, bond strength to H and proximity of the active sites[30] are important to impeding this step. For P. MoS$_2$, this rate-determining step indicates that there are H trap sites and poor H mobility on the petals, which is not uncommon for MoS$_2$ catalysts.[3,31,38,39,41] The high electron density on the surface Mo atoms of P. MoS$_2$ electrodes (as indicated by the low binding energies in XPS, Figure 3b) likely increases the strength of the H adsorption, rendering the chemical rearrangement of H$_{ads}$ the rate-limiting reaction. The TEM, XPS, and Raman studies suggest that the petals are frayed at the surface and behave as single-layer MoS$_2$. This separates the active sites from one another along the c-axis of the crystal structure.

Of note, the exchange current density with respect to geometric electrode area ($j_{0,geo}$, **Tables 1 & 3**) was very high for P. MoS$_2$/Mo (0.00290 mA cm^{-2}) and was similar to that seen by the Cui group for electrodes with a plane of densely-packed vertically-aligned MoS$_2$ layers on Si (0.0022 mA cm^{-2}).[42] Despite the comparatively low geometric packing of the MoS$_2$ petals on our electrodes, the high $j_{0,geo}$ indicates that the protruding shape of the petals provides a large number of active catalytic sites. The $j_{0,geo}$ for P. MoS$_2$/Au was lower at 0.000921 mA cm^{-2}. We ascribe this to the lower petal density of P. MoS$_2$/Au, which provides a lower number of catalytic sites (*vide supra*).

The EIS results are presented as Nyquist plots in Figure 4c and were modeled using a simple Randles circuit (Figure 10d). R$_{CT}$ is characteristic of the kinetics of the electron-transfer chemical reactions occurring at the petal edges. The absence of multiple semicircles in the Nyquist plots confirms that the MoS$_2$ petals completely cover the surface, and no underlying MoS$_x$O$_y$ is exposed to solution.[43] As expected from the increased surface roughness and $j_{0,geo}$, the R$_{CT}$ is correspondingly lower (and C$_{dl}$ is higher) for the P. MoS$_2$/Mo (3 Ω•cm^2) than for P. MoS$_2$/Au (13 Ω•cm^2).

Since C_{dl} is proportional to the real surface area, it was used to obtain the exchange current density normalized to the real surface area of each electrode, $j_{0,real}$ (See Table 1 above). The impedance of a CPE is given by:

$$Z_{CPE} = \frac{1}{(j\omega)^\alpha Y_0}$$

where j is the imaginary number, ω is the angular frequency, α is a constant equaling 1 for an ideal capacitor, and Y_0 is the capacitance. From fitting the EIS data using Randles circuit with CPE in place of a capacitor, Y_0 and α are obtained which can be used with ω_c (at $Z_{real} = R_u + \frac{R_{ct}}{2}$) to calculate C_{dl} as follows:

$$C_{dl} = Y_0(\omega_c)^{a-1}.$$

C_{dl} scales with electrochemical surface area.[44] Since atomically smooth metallic electrodes typically have C_{dl} of 20 μF cm^{-2},[45–47] the electrochemical roughness factor (RF) can be estimated as:

$$RF = \frac{C_{dl}}{20\ \mu F\ cm^{-2}}$$

For MoS_2 electrodes, C_{dl} is normalized to 10 μF cm^{-2}.[48] RF was used to calculate $j_{0,real}$ and j_{real} at -200 mV vs. RHE as such, the values of which are included in Table 3:

$$j_{real} = \frac{j_{geo}}{RF}.$$

The $j_{0,real}$ is on the same order for both P. MoS_2/Au and P. MoS_2/Mo, but indeed is larger for P. MoS_2/Au. While this may suggest that the Au support increases the inherent catalytic activity of the MoS_2 petals, we hesitate to speculate on the reason for this difference without deeper study.

63

Table 3. Measured and calculated values from EIS and LSV.

Electrode	Y_0 (μF cm^{-2})	ω (Hz)	α	C_{dl} (μF cm^{-2})	$j_{0,geo}$ (mA cm^{-2})	RF	$j_{0,real}$ (mA cm^{-2})
Pt	550	3776.258	0.75	70	0.447	3.5	0.13
P. MoS_2/Mo	24500	4.760921	0.7741	17200	0.00290	1700	$1.7*10^{-6}$
P. MoS_2/Au	2152	12.00102	0.8678	1549	0.000921	150	$5.9*10^{-6}$
Au	404.4	1503.907	0.725	54.1	0.00563	2.7	0.0021
Mo	341.5	4.760921	0.9781	330.03	0.000339	17	$2.1*10^{-5}$

A figure of merit for intrinsic HER activity is turnover frequency (TOF) per active site, which can be calculated using the equation:

$$TOF = \frac{jA}{nFN},$$

where j is the current density in A cm^{-2}, A is Avogadro's number, n is the number of electrons transferred (2 for HER), F is Faraday's constant, and N is the density of active sites.[34] For MoS_2 HER catalysts, TOF is usually calculated per surface Mo[28] which allows a comparison to other MoS_2 HER catalysts. N for the active edges was calculated using the crystallographic information for MoS_2. N was calculated by assuming that the real area was composed entirely of edges. Therefore, using the lattice parameters of 2H-MoS_2 from (JCPDS Card No. 37-1492) of a, b = 3.1612 Å and c = 12.2985 Å:

$$N = \frac{2\ Mo}{(3.1612*12.2985)\text{Å}^2} * \frac{10^{16}\text{Å}^2}{cm^2} = 5.14 * 10^{14} Mo\ cm^{-2}.$$

Then the TOF was calculated for P. MoS_2/Mo electrodes using $j_{real} = 2.8*10^{-6}$ A cm^{-2} at -200 mV vs. RHE:

$$TOF_{all\ SA} = \frac{2.8\times10^{-6}\ A\ cm^{-2} * 6.02\times10^{23}\ H_2\ mol^{-1}}{2 * 96485\ C\ mol^{-1} * 5.14 \cdot 10^{14}\ Mo\ cm^{-2}} = 0.017\ H_2\ Mo^{-1}\ s^{-1}$$

The TOF$_{\text{all SA}}$ was calculated for P. MoS$_2$/Mo at 0.017 H$_2$ Mo^{-1} s^{-1} and for P. MoS$_2$/Au at 0.042 H$_2$ Mo^{-1} s^{-1} (summarized in Table 4). This assumption provides a low estimate of TOF since the petaled MoS$_2$ presents a large portion of inactive, sulfur-terminated faces.

Table 4. Values used in TOF calculation for MoS$_2$ electrodes.

Electrode:	P. MoS$_2$/Au	P. MoS$_2$/Mo
$\lvert j_{geo} \rvert$ @ -200 mV (A cm^{-2})	0.00107	0.00475
*N (Mo atoms cm^{-2})	5.1443*10^{14}	5.1443*10^{14}
$\lvert j_{real} \rvert$ @ -200 mV (A cm^{-2})	6.9*10^{-6}	2.8*10^{-6}
*TOF$_{\text{all SA}}$ (H$_2$ Mo^{-1} s^{-1})	0.042	0.017

*Assuming real surface area is all edges

TOF was also calculated with a more realistic approximation (assuming petals are rectangular prisms) by multiplying by a factor to account for the limited portion of surface area that is actually comprised of active edge sites. For simplicity, the petals are approximated as rectangular prisms attached to the surface (only one long side exposed) with a height of 200 nm. SEM measurements (**Table 5**) were used to approximate the dimensions of the petals and obtain the ratio of exposed edges to total surface area of MoS$_2$. Thus, the petal edge surface area (SA) is:

$$SA_{edge} = width * (length + 2 * height),$$

the petal face SA is:

$$SA_{face} = 2 * length * height,$$

and the edge SA : total SA is:

$$SA_{edge:total} = \frac{SA_{edge}}{SA_{edge}+SA_{face}}.$$

Thus, the TOF, excluding faces from the active site density, with the understanding that only edges are HER-active is:

$$TOF_{edges\;only} = \frac{TOF_{all\;SA}}{SA_{edge:total}} = \frac{0.017\;H_2\;Mo^{-1}\;s^{-1}}{0.0679} = 0.25\;H_2\;Mo^{-1}\;s^{-1}.$$

Table 5. Measured and calculated values used to calculate TOF.

Electrode:	P. MoS₂/Mo			P. MoS₂/Au		
	average	st. dev.	n	average	st. dev.	n
Petal length (nm)	117	93	296	118	90	205
Petal width (nm)	6.7	2.6	139	8.6	3.5	91
† Petal height (nm)	200			200		
**SA_{edge} (nm²)	3419			4468		
**SA_{face} (nm²)	46930			47280		
**$SA_{edge:total}$	0.0679			0.0864		
**$TOF_{edges,only}$ (H_2 Mo^{-1} s^{-1})	0.25			0.48		

† Estimated from SEM images.

**Assuming petals are rectangular prisms.

$TOF_{edges\ only}$ was also calculated for P. MoS₂/Au and found to be 0.48 H_2 Mo^{-1} s^{-1}, approximately double that of P. MoS₂/Mo. These values are similar to other MoS_x electrodes which have TOFs between 0.2 – 1 H_2 Mo^{-1} s^{-1} at -200 mV vs RHE.[28] Combined, the high $j_{0,geo}$ but unremarkable TOF highlight that it is the shape of the MoS₂ petals that lend these electrodes their impressive HER activity.

The uncompensated resistance R_u, contains, in series, the solution resistance and the resistance at the interface between the layers such as the Mo-MoS_xO_y-MoS₂ interfaces and Au-MoS₂ interface. In the electrolyte, the solution resistance should be similar for all electrodes, so changes in R_u reflect the resistance of the layer interfaces alone. The R_u for the P. MoS₂/Mo (2.2 Ω•cm²) electrodes is quite low, and sits between that of Pt (0.5 Ω•cm²) and the Mo and Au metallic electrodes (both 3.6 Ω•cm²). This indicates that the contact between the P. MoS₂ and the Mo support is nearly ohmic and most importantly, the MoS_xO_y intermediate layer is not resistive as previously feared but instead provides an optimal electronic interface between the support Mo and catalytic petaled MoS₂ surface, although it may inhibit the intrinsic activity, as suggested by the decreased TOF compared to P. MoS₂/Au.

The contact for P. MoS₂/Au is also highly conductive (R_u= 2.4 Ω•cm²). The Au-MoS₂ interface, in particular, has been predicted to suffer from a large tunnel barrier, high Schottky barrier, and weak orbital overlap due to the lattice mismatch between Au and MoS₂ when the MoS₂ lies coplanar to the surface.[12] This has been found to be experimentally true for top metal-MoS₂ contacts in transistor designs.[49–51] In contrast,

arranging single MoS_2 sheets perpendicularly to Au contacts has been computationally shown to improve electronic connections[12] and experimentally shown to form ohmic contacts.[52] The low R_u of P. MoS_2/Au is likely a result of the arrangement of the petals perpendicular to the Au surface, which optimizes the electronic contact.

Conclusions

In this work, the support material for P. MoS_2 electrodes was found to be crucial to their performance. P. MoS_2, when grown on Mo foil, was found to have a MoS_xO_y intermediate layer with unknown electrochemical properties. Thus we sought a synthesis where the Mo film thickness was limited to prevent the formation of this layer. Mo could not be electrodeposited on Pt, precluding the synthesis of P. MoS_2/Pt. The synthetic technique identified that FTO has poor surface adhesion to MoS_2 petals. However, P. MoS_2 was grown from Au for the first time in this work by electrodepositing a controlled amount of Mo on an Au support, then carrying out a hydrothermal reaction with thiourea and water. In this manner the MoS_xO_y layer was excluded. This inexpensive and easily scalable synthesis shows promise as an alternate method of producing this material on a wider variety of substrates.

The material properties and HER activity of P. MoS_2/Mo were compared to P. MoS_2/Au using a variety of techniques. Raman, TEM and XPS demonstrate that the multilayer petals are frayed at the edges, showing metallic, $1T-MoS_2$ character, and are chemically identical whether grown from Mo or Au substrates.

In general, both P. MoS_2/Mo and P. MoS_2/Au showed excellent electrode characteristics for HER. P. MoS_2/Mo required a 242 mV overpotential to achieve 10 mA cm^{-2}, which was 35 mV lower when compared to P. MoS_2/Au. Also, P. MoS_2/Mo gave an exchange current density of 0.00290 mA/ cm^{-2} which was ~3x higher than that of P. MoS_2/Au. We ascribe these differences to a higher petal density on P. MoS_2/Mo than P. MoS_2/Au. In turn, the petal density is a result of the surface roughness of the Mo surface from which the MoS_2 was synthesized. The effect of petal density was also reflected in the charge-transfer resistance (3.4 $\Omega \cdot cm^2$ vs.

13 $\Omega \cdot cm^2$) and double layer capacitance (17.2 mF cm^{-2} vs. 1.55 mF cm^{-2}) from EIS studies. Conservative estimates of turnover frequency were calculated, revealing similar TOFs for petaled MoS$_2$ independent of Mo or Au substrate (0.25 H$_2$ Mo^{-1} s^{-1} vs. 0.48 H$_2$ Mo^{-1} s^{-1}, respectively) and similar to that of other MoS$_2$ electrodes seen in the literature.

Both P. MoS$_2$/Mo and P. MoS$_2$/Au showed ohmic contacts with very low R$_u$ of less than 2.4 $\Omega \cdot cm^2$. It is likely the vertical arrangement of the petals on Au contributes to the excellent contact, which has been shown elsewhere to be resistive when MoS$_2$ lies coplanar to Au. The results also show that the MoS$_x$O$_y$ intermediate layer seen in P. MoS$_2$/Mo is not resistive, and instead provides a near ideal electrical contact between the two layers.

In the future, scientific efforts should be dedicated to developing synthetic techniques to increase the petal density and therefore the density of active sites in this self-supported, nanostructured material. Additionally, further exploration of methods to increase the adhesion of the precursors, intermediates, and product MoS$_2$ to the substrate should be undertaken. Exploration of additional substrates which have similar lattice spacing to MoS$_2$ will yield advances toward practical P. MoS$_2$ electrodes.

References

(1)   Sobczynski, A. Molybdenum Disulfide as a Hydrogen Evolution Catalyst for Water Photodecomposition on Semiconductors. *J. Catal.* **1991**, *131* (1), 156–166.

(2)   Finn, S. T.; Macdonald, J. E. Petaled Molybdenum Disulfide Surfaces: Facile Synthesis of a Superior Cathode for QDSSCs. *Adv. Energy Mater.* **2014**, *4*.

(3)   Jaramillo, T. F.; Jørgensen, K. P.; Bonde, J.; Nielsen, J. H.; Horch, S.; Chorkendorff, I. Identification of Active Edge Sites for Electrochemical H$_2$ Evolution from MoS$_2$ Nanocatalysts. *Science* **2007**, *317* (July), 100–102.

(4)   Chen, Z.; Forman, A. J.; Jaramillo, T. F. Bridging the Gap between Bulk and Nanostructured Photoelectrodes: The Impact of Surface States on the Electrocatalytic and Photoelectrochemical Properties of MoS$_2$. *J. Phys. Chem. C* **2013**, *117* (19), 9713–9722.

(5)   Kong, D.; Wang, H.; Cha, J. J.; Pasta, M.; Koski, K. J.; Yao, J.; Cui, Y. Synthesis of MoS2 and MoSe2 Films with Vertically Aligned Layers. *Nano Lett.* **2013**, *13* (3), 1341–1347.

(6)   Faber, M. S.; Jin, S. Earth-Abundant Inorganic Electrocatalysts and Their Nanostructures for Energy Conversion Applications. *Energy Environ. Sci.* **2014**, *7* (11), 3519–3542.

(7)   Nikam, R. D.; Lu, A. Y.; Sonawane, P. A.; Kumar, U. R.; Yadav, K.; Li, L.-J.; Chen, Y.-T. Three-Dimensional Heterostructures of MoS2 Nanosheets on Conducting MoO2 as an Efficient Electrocatalyst to Enhance Hydrogen Evolution Reaction. *ACS Appl. Mater. Interfaces* **2015**, *7* (41), 23328–23335.

(8)   Yan, Y.; Xia, B.; Li, N.; Xu, Z.; Fisher, A.; Wang, X. Vertically Oriented MoS2 and WS2 Nanosheets Directly Grown on Carbon Cloth as Efficient and Stable 3-Dimensional Hydrogen-Evolving Cathodes. *J. Mater. Chem. A* **2015**, *3* (1), 131–135.

(9)   Hinnemann, B.; Nørskov, J. K.; Topsøe, H. A Density Functional Study of the Chemical Differences between Type I and Type II MoS2-Based Structures in Hydrotreating Catalysts. *J. Phys. Chem. B* **2005**, *109* (6), 2245–2253.

(10)   Bouroushian, M. *Electrochemistry of the Metal Chalcogenides*, 1st ed.; Scholz, F., Ed.; Springer: Berlin, 2010.

(11)   Kang, J.; Liu, W.; Banerjee, K. High-Performance MoS2 Transistors with Low-Resistance Molybdenum Contacts. *Appl. Phys. Lett.* **2014**, *104* (9), 93106.

(12)   Kang, J.; Liu, W.; Sarkar, D.; Jena, D.; Banerjee, K. Computational Study of Metal Contacts to Monolayer Transition-Metal Dichalcogenide Semiconductors. *Phys. Rev. X* **2014**, *4* (3), 31005-1-

031005–031014.

(13)   Park, W.; Kim, Y.; Lee, S. K. Contact Resistance Reduction Using Fermi Level de-Pinning Layer for MoS2 FETs. *Electron Dev. Meet.* **2014**, *8*, 5.1.1-5.1.4.

(14)   Allain, A.; Kang, J.; Banerjee, K.; Kis, A. Electrical Contacts to Two-Dimensional Semiconductors. *Nat. Mater.* **2015**, *14* (12), 1195–1205.

(15)   Chuang, S.; Battaglia, C.; Azcatl, A.; McDonnell, S.; Kang, J. S.; Yin, X.; Tosun, M.; Kapadia, R.; Fang, H.; Wallace, R. M.; Javey, A. MoS2 P-Type Transistors and Diodes Enabled by High Work Function MoOx Contacts. *Nano Lett.* **2014**, *14* (3), 1337–1342.

(16)   *Handbook of Reference Electrodes*; Inzelt, G., Lewenstam, A., Scholz, F., Eds.; Springer Berlin Heidelberg: Berlin, Heidelberg, 2013.

(17)   Rao, C. N. R.; Nath, M. Inorganic Nanotubes. *Dalt. Trans.* **2003**, No. 1, 1–24.

(18)   Meiron, O. E.; Houben, L.; Bar-Sadan, M. Understanding the Formation Mechanism and the 3D Structure of Mo(S X Se 1−x) 2 Nanoflowers. *RSC Adv.* **2015**, *5* (107), 88108–88114.

(19)   Ye, L.; Guo, W.; Yang, Y.; Du, Y.; Xie, Y. Directing the Architecture of Various MoS$_2$ Hierarchical Hollow Cages through the Controllable Synthesis of Surfactant/molybdate Composite Precursors. *Chem. Mater.* **2007**, *19*, 6331–6337.

(20)   Ye, L.; Wu, C.; Guo, W.; Xie, Y. MoS2 Hierarchical Hollow Cubic Cages Assembled by Bilayers: One-Step Synthesis and Their Electrochemical Hydrogen Storage Properties. *Chem. Commun. (Camb).* **2006**, *2*, 4738–4740.

(21)   Haynes, W. N.; Bruno, T. J.; Lide, D. R. Electrochemical Series. In *CRC Handbook of Chemistry and Physics: Internet Version*; Haynes, W. M., Lide, D. R., Bruno, T. J., Eds.; CRC Press, 2015.

(22)   Morley, T. J.; Penner, L.; Schaffer, P.; Ruth, T. J.; Bénard, F.; Asselin, E. The Deposition of Smooth Metallic Molybdenum from Aqueous Electrolytes Containing Molybdate Ions. *Electrochem. commun.* **2012**, *15* (1), 78–80.

(23)   Eda, G.; Yamaguchi, H.; Voiry, D.; Fujita, T.; Chen, M.; Chhowalla, M. Photoluminescence from Chemically Exfoliated MoS2. *Nano Lett.* **2011**, *11* (12), 5111–5116.

(24)   Jiménez Sandoval, S.; Yang, D.; Frindt, R.; Irwin, J. Raman Study and Lattice Dynamics of Single Molecular Layers of MoS2. *Phys. Rev. B* **1991**, *44* (8), 3955–3962.

(25)   NIST X-Ray Photoelectron Spectroscopy (XPS) Database http://srdata.nist.gov/xps/ (accessed Feb 20, 2016).

(26)   B. Vincent Crist. *Handbook of Monochromatic XPS Spectra*; John Wiley & Sons, Inc.: Chichester ; New York, 2000.

(27)   Wu, S.; Zeng, Z.; He, Q.; Wang, Z.; Wang, S. J.; Du, Y.; Yin, Z.; Sun, X.; Chen, W.; Zhang, H. Electrochemically Reduced Single-Layer MoS$_2$ Nanosheets: Characterization, Properties, and Sensing Applications. *Small* **2012**, *8* (14), 2264–2270.

(28)   Benck, J. D.; Hellstern, T. R.; Kibsgaard, J.; Chakthranont, P.; Jaramillo, T. F. Catalyzing the Hydrogen Evolution Reaction (HER) with Molybdenum Sulfide Nanomaterials. *ACS Catal.* **2014**, *4*, 3957–3971.

(29)   Nørskov, J. K.; Bligaard, T.; Logadottir, A.; Kitchin, J. R.; Chen, J. G.; Pandelov, S.; Stimming, U. Trends in the Exchange Current for Hydrogen Evolution. *J. Electrochem. Soc.* **2005**, *152* (3), J23–J26.

(30)   Kibsgaard, J.; Jaramillo, T. F.; Besenbacher, F. Building an Appropriate Active-Site Motif into a Hydrogen-Evolution Catalyst with Thiomolybdate [Mo3S13]2- Clusters. *Nat. Chem.* **2014**, *6* (3), 248–253.

(31)   Kibsgaard, J.; Chen, Z.; Reinecke, B. N.; Jaramillo, T. F. Engineering the Surface Structure of MoS$_2$ to

Preferentially Expose Active Edge Sites for Electrocatalysis. *Nat. Mater.* **2012**, *11* (11), 963–969.

(32)   Merki, D.; Fierro, S.; Vrubel, H.; Hu, X. Amorphous Molybdenum Sulfide Films as Catalysts for Electrochemical Hydrogen Production in Water. *Chem. Sci.* **2011**, *2* (7), 1262–1267.

(33)   Li, Y.; Wang, H.; Xie, L.; Liang, Y.; Hong, G.; Dai, H. MoS 2 Nanoparticles Grown on Graphene: An Advanced Catalyst for the Hydrogen Evolution Reaction. *J. Am. Chem. Soc.* **2011**, *133* (19), 7296–7299.

(34)   Shin, S.; Jin, Z.; Kwon, D. H.; Bose, R.; Min, Y.-S. High Turnover Frequency of Hydrogen Evolution Reaction on Amorphous MoS 2 Thin Film Directly Grown by Atomic Layer Deposition. *Langmuir* **2015**, *31* (3), 1196–1202.

(35)   Jaramillo, T. F.; Bonde, J.; Zhang, J.; Ooi, B.-L.; Andersson, K.; Ulstrup, J.; Chorkendorff, I. Hydrogen Evolution on Supported Incomplete Cubane-Type [Mo 3 S 4] $^{4+}$ Electrocatalysts. *J. Phys. Chem. C* **2008**, *112* (45), 17492–17498.

(36)   Conway, B. E.; Tilak, B. V. Interfacial Processes Involving Electrocatalytic Evolution and Oxidation of H2, and the Role of Chemisorbed H. *Electrochim. Acta* **2002**, *47* (22–23), 3571–3594.

(37)   Chen, Z.; Cummins, D.; Reinecke, B. N.; Clark, E.; Sunkara, M. K.; Jaramillo, T. F. Core-Shell MoO3-MoS2 Nanowires for Hydrogen Evolution: A Functional Design for Electrocatalytic Materials. *Nano Lett.* **2011**, *11* (10), 4168–4175.

(38)   Wang, T.; Liu, L.; Zhu, Z.; Papakonstantinou, P.; Hu, J.; Liu, H.; Li, M. Enhanced Electrocatalytic Activity for Hydrogen Evolution Reaction from Self-Assembled Monodispersed Molybdenum Sulfide Nanoparticles on an Au Electrode. *Energy Environ. Sci.* **2013**, *6*, 625–633.

(39)   Wu, Z.; Fang, B.; Wang, Z.; Wang, C.; Liu, Z.; Liu, F.; Wang, W.; Alfantazi, A.; Wang, D.; Wilkinson, D. P. MoS2 Nanosheets: A Designed Structure with High Active Site Density for the Hydrogen Evolution Reaction. *ACS Catal.* **2013**, *3* (9), 2101–2107.

(40)   Kodintsev, I. M.; Trasatti, S. Electrocatalysis of H2 Evolution on RuO2 + IrO2 Mixed Oxide Electrodes. *Electrochim. Acta* **1994**, *39* (11–12), 1803–1808.

(41)   Chen, Z.; Cummins, D.; Reinecke, B. N.; Clark, E.; Sunkara, M. K.; Jaramillo, T. F. CoreÀshell MoO 3 ÀMoS 2 Nanowires for Hydrogen Evolution : **2011**, 4168–4175.

(42)   Kong, D.; Wang, H.; Cha, J. J.; Pasta, M.; Koski, K. J.; Yao, J.; Cui, Y. Synthesis of MoS2 and MoSe2 Films with Vertically Aligned Layers. *Nano Lett.* **2013**, *13* (3), 1341–1347.

(43)   Kwak, K. J.; Valincius, G.; Liao, W.-C.; Hu, X.; Wen, X.; Lee, A.; Yu, B.; Vanderah, D. J.; Lu, W.; Lee, L. J. Formation and Finite Element Analysis of Tethered Bilayer Lipid Structures. *Langmuir* **2010**, *26* (23), 18199–18208.

(44)   Bard, A. J.; Faulkner, L. R. *Electrochemical Methods : Fundamentals and Applications*; Wiley, 2001.

(45)   Kavan, L.; Yum, J. H.; Grätzel, M. Optically Transparent Cathode for Dye-Sensitized Solar Cells Based on Graphene Nanoplatelets. *ACS Nano* **2011**, *5* (1), 165–172.

(46)   Domínguez-Crespo, M. A.; Ramírez-Meneses, E.; Torres-Huerta, A. M.; Garibay-Febles, V.; Philippot, K. Kinetics of Hydrogen Evolution Reaction on Stabilized Ni, Pt and Ni–Pt Nanoparticles Obtained by an Organometallic Approach. *Int. J. Hydrogen Energy* **2012**, *37* (6), 4798–4811.

(47)   Holze, R. (Rudolf). *Experimental Electrochemistry : A Laboratory Textbook*; Wiley-VCH, 2009.

(48)   Yu, Y.; Huang, S.-Y.; Li, Y.; Steinmann, S. N.; Yang, W.; Cao, L. Layer-Dependent Electrocatalysis of MoS2 for Hydrogen Evolution. *Nano Lett.* **2014**, *14* (2), 553–558.

(49)   Kappera, R.; Voiry, D.; Yalcin, S. E.; Branch, B.; Gupta, G.; Mohite, A. D.; Chhowalla, M. Phase-Engineered Low-Resistance Contacts for Ultrathin MoS2 Transistors. *Nat. Mater.* **2014**, *13* (12), 1128–1134.

(50)   Maurel, C.; Coratger, R.; Ajustron, F.; Beauvillain, J.; Gerard, P. Electrical Characteristics of

Metal/semiconductor Nanocontacts Using Light Emission in a Scanning Tunneling Microscope. *J. Appl.*

Phys. **2003**, *94* (3), 1979.

(51)   Li, S.-L.; Komatsu, K.; Nakaharai, S.; Lin, Y.-F.; Yamamoto, M.; Duan, X.; Tsukagoshi, K. Thickness

Scaling Effect on Interfacial Barrier and Electrical Contact to Two-Dimensional MoS $_2$ Layers. *ACS*

Nano **2014**, *8* (12), 12836–12842.

(52)   Wang, Q. H.; Kalantar-Zadeh, K.; Kis, A.; Coleman, J. N.; Strano, M. S. Electronics and Optoelectronics

of Two-Dimensional Transition Metal Dichalcogenides. *Nat. Nanotechnol.* **2012**, *7* (11), 699–712.

Evaluation of Petaled MoS$_2$ Electrocatalysts for Use in Lithium-Ion Batteries
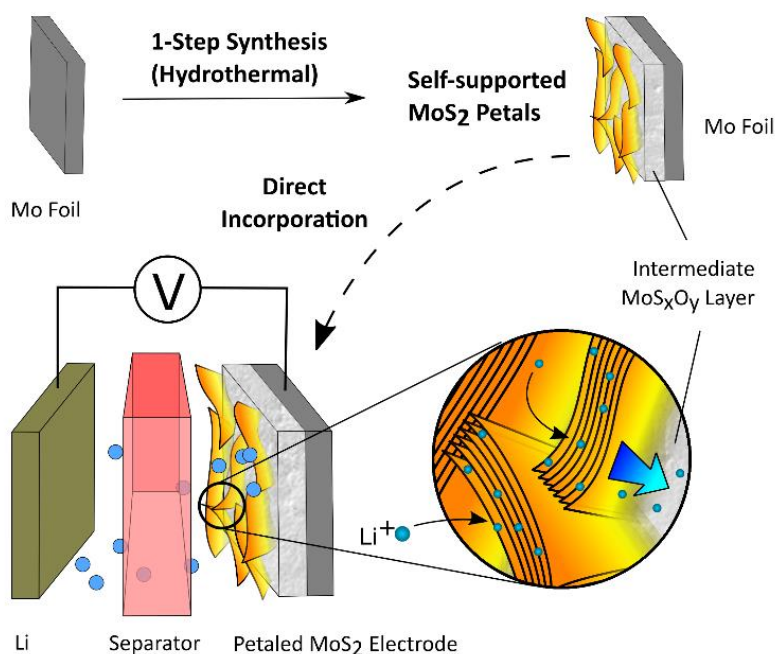
Introduction

Lithium ion batteries (LIBs) are now a commonly used energy storage technology present in electric

vehicles and portable electronics. LIBs are flourishing due to their rechargeability, which results from their

reversible chemistry (*vs* alkaline Zn-MnO$_2$ batteries), light weight, and increased energy and power density per

unit mass over lead-sulfur or nickel-cadmium batteries. The technologies that require portable energy storage

are highly diverse, thus different LIB designs must be developed to meet the varying needs in size, weight, and

energy capacity. For example, the incorporation of LIBs into microelectronics such as microelectromechanical

devices (MEMS), back up storage on hard drives or in circuits, and implantable electronics for use in medicine[1–5] require design considerations that are considerably different from those of bulk battery systems. Typical bulk LIB systems contain a liquid or polymer slurry electrolyte, bulk graphite anode, and a cathode made from a Li metal oxide, carbon black, and binder. Other systems require a solid-state electrolyte and a self-supported anode and/or cathode electrode[6,7] in order to achieve small battery sizes. In general, self-supported electrode materials have the advantages of high surface area for high power energetics and direct electrical contact to their underlying substrates.[8,9]

Self-supported MoS_2 presents itself as a promising candidate for use as a LIB electrode. This and other transition metal dichalcogenides have long attracted attention as a LIB electrode material. As a cathode, MoS_2 has favorable energetics of its intercalation reaction with a reasonably high $E_{1/2}$ of 2.1 V *vs.* Li/Li$^+$ (all voltages reported in this chapter are *vs.* Li/Li$^+$).[10–13] More recently, MoS_2 has been considered as an anode material to be paired with the $LiMO_x$ family of high-voltage cathodes for LIBs due to its large theoretical capacity of 1675 mA h g^{-1} and significant rate capability,[13–18] *i.e.* a high maximum charging rate relative to its nominal capacity. For both anode and cathode roles, the intermediate voltage of MoS_2 is not ideal, but is compensated for by its extended cycling stability and charge storage capacity.[13]

In addition to the advantages of using MoS_2 for LIBs, there has been a renewed interest in MoS_2 over the last several years due to the ability to develop few- and single-layer nanostructures with a myriad of potential uses, which has led to a large body of research directed towards simplifying synthesis of such nanostructures.[19–22] Specifically for LIBs, layered, nanostructured materials offer greater free volume per unit cell for accommodating intercalants and a higher surface area-to-volume ratio than bulk materials. As has been shown in previous chapters, P. MoS_2/Mo electrodes synthesized using a simple, scalable, hydrothermal technique performed excellently as an inexpensive and highly active electrode material towards polysulfide (S_n^{2-}) reduction in liquid-junction QDSSCs.[23] The large, intermediate, MoS_xO_y layer between the Mo substrate

and the MoS_2 petals provides excellent ohmic contact.[24] Thus, this material is promising as an inexpensive, self-supported LIB electrode material.

In the following discussion, I will present the application of this self-supported petaled MoS_2 as an electrode material for LIBs that acts as a high-surface-area structural support for Li_2S-S_n^{2-} and Mo-MoO_3 conversion, but also exhibits high capacity, rate capability, and cyclability as a cathode.

Experimental

Preparation of Petaled MoS_2 and Hydrothermal MoO_x Electrodes for LIB testing

Nanostructured MoS_2 petals were prepared as in Chapter II, but with two $1 \times 1 \times 0.025$ cm^3 Mo foil pieces (99.95%, Strem) instead of one 1.5×1.5 cm^2 Mo foil piece, as was necessary for assembly into a Li coin cell. Hydrothermal MoO_x electrodes were synthesized using the exact same conditions as the petaled MoS_2 electrodes, except that no thiourea was added.

Characterization

Focused Ion Beam (FIB) milling followed by scanning electron microscopy (SEM) imaging and Energy Dispersive X-ray Spectroscopy (EDS) elemental identification was performed on a Tescan Lyra 3 XMU Focused Ion Beam Scanning Electron Microscope, located at Middle Tennessee State University Interdisciplinary Microanalysis and Imaging Center (MIMIC), and operated by Joyce Miller . Due to the high surface roughness of petaled MoS_2, a ~2 µm thick Pt layer was deposited prior to Ga^{3+} ion milling using 49 pA deposition current for 30 min. Rough milling of the material was performed at 857 pA for 25 min to achieve a 5 µm deep trench. Finally, the wall of the trench was polished using 218 pA beam current to remove curtaining.

The EDS spectra were collected at 15.0 keV and quantified using Bruker Quantax 200 software, which was calibrated prior to collection using high-quality Cu tape.

Glancing-Angle X-Ray Diffraction (GAXRD) measurements were taken using a Scintag XGEN-4000 X-ray diffractometer with a Cu Kα (λ = 0.154 nm) radiation source. The X-ray source (ω) was held at 0.1° while the detector (θ) scanned from 20-60° with step size 0.05° and scan rate of 0.002°/s.

Raman spectra of samples were collected using a Renishaw inVia MicroRaman system with 535nm LASER excitation, and at 50x magnification.

Batteries were tested in a half-cell Li ion battery configuration using a 1M $LiPF_6$ in ethylene carbonate and dimethyl carbonate electrolyte, with a Celgard® separator, and a Li metal counter-electrode. Electrochemical testing was performed on an Autolab Multichannel analyzer, and with an MTI 8 channel battery analyzer.

Results & Discussion

Materials Characterization

The petaled MoS_2 structure was synthesized as described previously,[23] and is comprised of a uniform film of MoS_2 petals grown from Mo foil and separated by an intermediate, MoS_xO_y layer. As a full understanding of the chemical composition of both the upper petaled region and the intermediate layer is crucial for determining the chemistry of LIB reactions as well as the active mass, we performed a series of experiments to verify the chemical composition of the intermediate layer. A cross-sectional Raman spectrum (Figure 1) supplements the evidence in previous chapters that the intermediate layer is a material with a combination of crystalline MoS_2 as well as amorphous MoO_2- and MoO_3-like molybdenum centers, all of which have been found to be active species for Li^+ intercalation.[25–27] Although each of the peaks is likely to be some convolution

of several smaller peaks, previous studies by other groups suggest that the peaks at 849 cm^{-1} and 938 cm^{-1} (Fig. 1b) are due to amorphous MoO_3,[26, 27] the peaks 440 cm^{-1} and 744 cm^{-1} are due to amorphous MoO_2,[26, 28] and the peak at 305 cm^{-1} is due to a combination of both MoO_2 and MoO_3. The hydrothermal MoO_x (Fig. 1c), which is described later as a negative control for thiourea, shows less distinctive Raman features that broadly coincide with those peaks observed in P. MoS_2, specifically at 305 cm^{-1}, 440 cm^{-1}, and 740 – 940 cm^{-1}, but without the characteristic MoS_2 peaks. This data suggests that the MoOx is even less crystalline than that found in the intermediate layer of P. MoS_2.
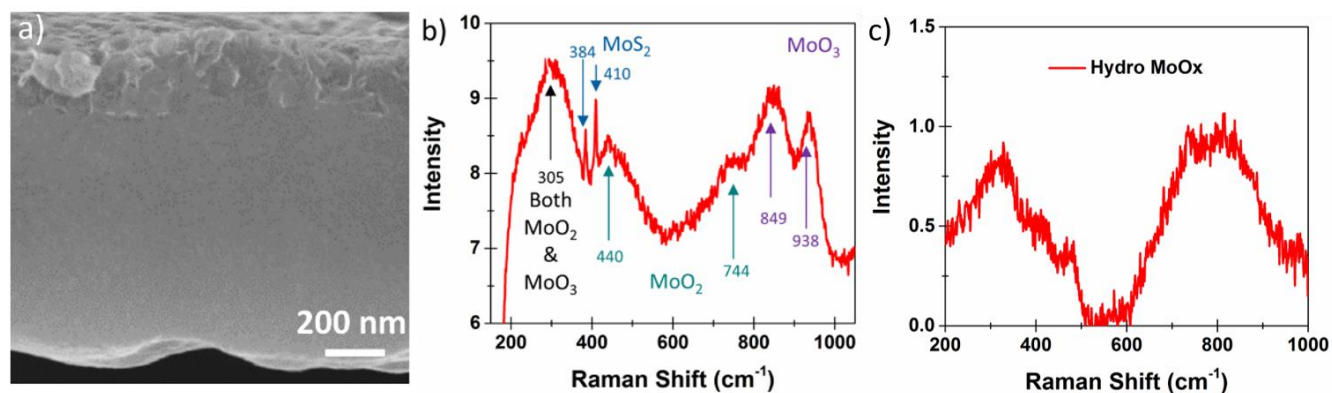
Figure 1. Cross-sectional SEM image of exfoliated P. MoS_2 (a). Raman spectra of the P. MoS_2 cross-section (b) and hydrothermally synthesized MoO_x material (c).

In order to determine the ratios of the different chemical species present in the intermediate layer, we performed focused ion beam (FIB) milling of the material into the Mo substrate followed by energy-dispersive X-ray spectroscopy (EDS, Figure 2). The study revealed that at the deepest interface between the Mo foil and the MoS_xO_y layer, there is little to no S present and a small amount of O (Figure 2 a,c). Towards the middle of the intermediate layer, the amount of S and O increases to reach a Mo:S:O ratio of approximately 1:0.5:2 (Figure 2 a,c,d), which is observed even at the top of the MoS_2 petals (Figure 2 b,f).
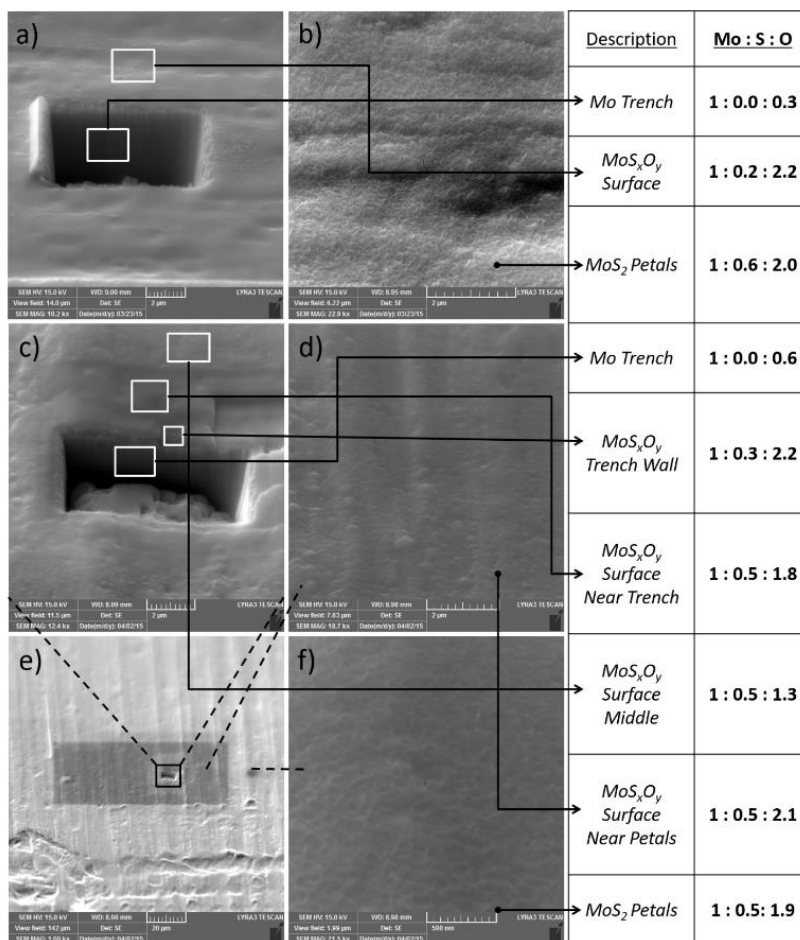
Figure 2. SEM images of petaled MoS$_2$ samples 1 (a, b) and 2 (c-f). The white rectangles correspond to EDS collection areas while in b, d, and f, the entire SEM image area was collected. (e) Low-magnification view of measurement region; note the darker contrast in the area imaged using FIB due to destruction by Ga^{3+} ions. Dashed lines connect zoomed-out view of regions in (e) to corresponding zoomed-in regions (c, d, f); solid arrows are drawn from the numbered collection area to its corresponding label and Mo:S:O ratio.

Estimation of Active Mass

The mass of the petaled region was determined by measuring the petal length density from several top-down SEM images, giving a geometric density of $0.0192 \frac{nm\,petal\,length}{nm^2\,image}$. The petal edge area within each image was then determined by multiplying the petal length density by the average thickness of the petals (6.78 nm) as determined using TEM:

$$Petal\ Edge\ Area: Image\ Area = \frac{Petal\ Length\ (nm)}{Image\ Area\ (nm^2)} * Petal\ width\ (nm)$$

$$\frac{0.0192\ nm}{nm^2} * 6.78\ nm = 0.129\ (or\ 12.9\%)$$

The total mass of the MoS_2 petals was then determined using the height of the petaled region as determined from cross-sectional SEM images and the density (ρ) of MoS_2 (5.06 g mL^{-1}):

$$P.MoS_2\ Mass = Cubic\ Volume\ of\ P.MoS_2 * Petal\ Edge\ Area: Image\ Area * \rho_{MoS_2}$$

$$1\ cm * 1\ cm * 200\ nm * 0.129 * 5.06\ g\ mL^{-1} = 13.05\ \mu g$$

The mass of the intermediate layer was determined by first using the volume measurements from external measurements and cross-sectional SEM images (Figure 1a) with a total volume of 1 cm × 1 cm × 800 nm, which gives a total volume of 0.08 mm³. The density was estimated using the EDS data in Figure 2 where it was shown that the intermediate layer had an approximate elemental ratio of 1 Mo: 0.5 S: 1.9 O. Assuming all of the S is from MoS_2 that would suggest that 25% of the Mo is used to form MoS_2. This leaves the remaining 75% of Mo to be found in MoO_2 and MoO_3 compounds. An O ratio of ~1.9 suggests 37.5% MoO_2 and 37.5% MoO_3. Thus, we estimate that the intermediate layer is composed of approximately 25% MoS_2, 37.5% MoO_2 and 37.5% MoO_3.

The densities of MoS_2, MoO_2 and MoO_3 are 5.06 g cm^{-3}, 6.47 g cm^{-3} and 4.69 g cm^{-3}, respectively. Therefore, the weighted average density of the intermediate MoS_xO_y layer is 5.51 g cm^{-3}, as calculated below:

MoS₂: 0.25*5.06

MoO₂: 0.375*6.47

MoO₃: 0.375*4.69

Total: 5.51 g/cm³

With these two estimates for the volume and density we can derive a mass estimate for the MoS_xO_y layer:

$$0.08mm^3 * 5.51\ g/cm^3 = 440.8\ \mu g\ MoS_xO_y\ (110.2\ \mu g\ MoS_2).$$

The self-supported P. MoS_2 material was then tested it in a half-cell LIB configuration using a $LiPF_6$ electrolyte, a Celgard® separator, and a Li metal counter electrode. Andrew Westover[*] and Landon Oakes, in the research lab of Dr. Cary Pint, performed LIB testing and provided analysis. In order to ensure that the capacity in the petaled MoS_2 was indeed due to the petaled morphology we first compared the cyclic voltammetric (CV) behavior of the petaled MoS_2, a flat Mo foil, and a hydrothermally synthesized MoO_x analog that was made using the same process as the petaled MoS_2 but without thiourea. The comparison of the current density of these three materials clearly shows that the petaled MoS_2 outperforms both the Mo foil and the hydrothermal MoO_x material, highlighting that the sulfur (S) plays a key role in enabling Li^+ storage in the material (**Figure 3a**).
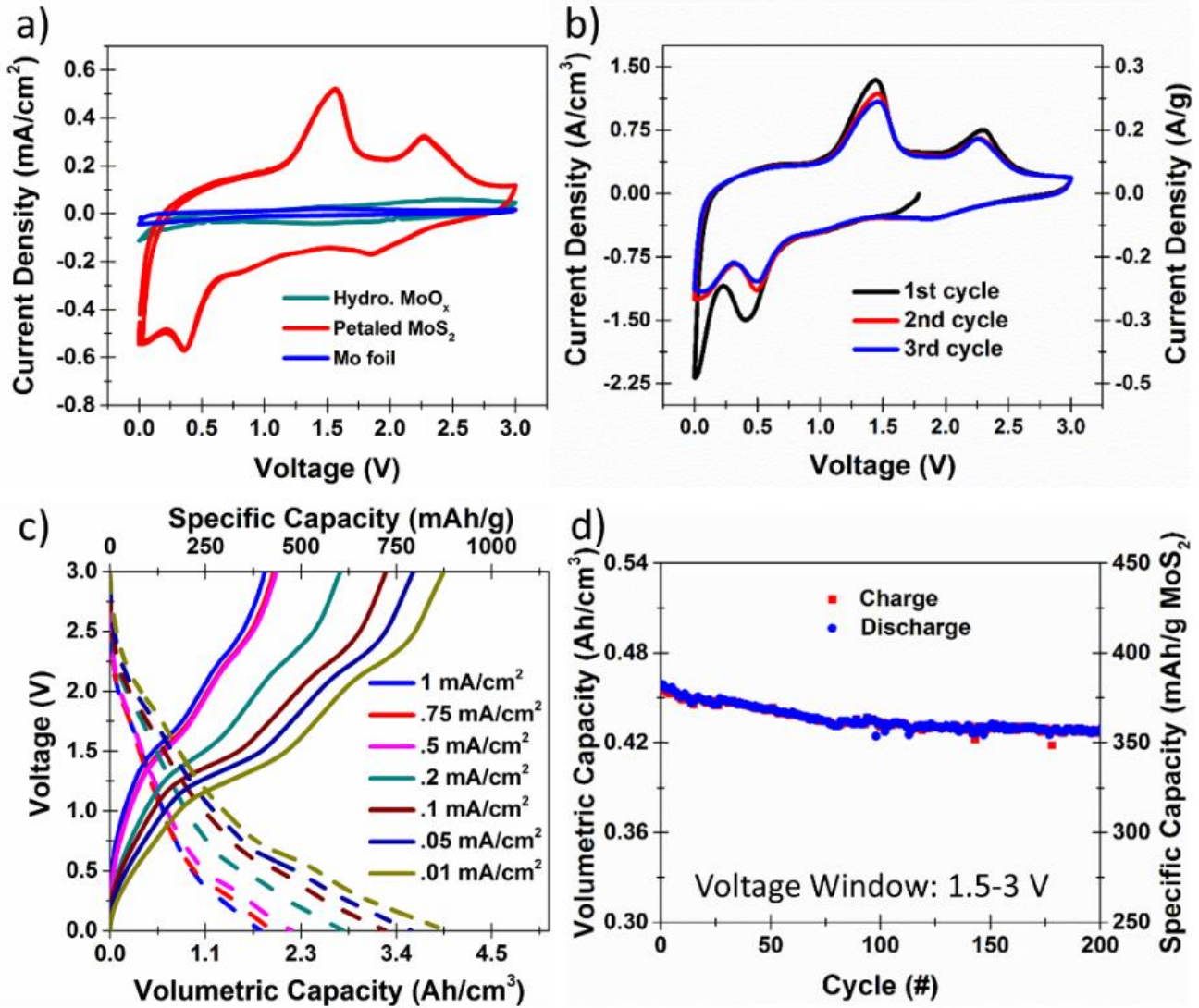
Figure 3. a) CV curves of petaled MoS_2, hydrothermally synthesized MoO_x and Mo foil. b) first three CV curves for Petaled MoS_2. c) Charge/discharge curves at various charging rates for petaled MoS_2. d) High voltage cycling of the petaled MoS_2 at 0.01 mA/cm^2.

Table 1. Prediction of experimental peak positions in Figure 2b and processes of P. MoS_2 electrode based on literature reports.

Scan #	Sweep Direction	Peak Position (V)	Process	Reference
1	cathodic (-)	0.9	$Li^+ + MoS_2 \rightarrow Li_xMoS_2$	13-17, 21
		0.4	$Li_xMoS_2 \rightarrow Li_2S + Mo$	
			$Li^+ + MoO_x \rightarrow Li_xMoO_x$	27
	anodic (+)	1.5	$Li_xMoO_x \rightarrow Li^+ + MoO_x$	27-29
		2.25	$Li_2S \rightarrow Li^+ + S_n^{2-}$	13-17
2	cathodic (-)	1.9	$Li^+ + S_n^{2-} \rightarrow Li_2S$	13-17, 21
		0.9	$Li^+ + MoS_2 \rightarrow Li_xMoS_2$	
		0.5	$Li^+ + MoO_x \rightarrow Li_xMoO_x$	27

83

In Fig. 3b, the first discharge scan in the CV of the petaled MoS_2 material (in the cathodic (-) direction from the open-circuit potential, during which lithiation is expected) shows one small peak at 0.9 V and one intense peak at 0.4 V followed by the onset of Li^0 deposition as 0 V is approached. The peak at 0.9 V is related to Li^+ intercalation into MoS_2 and the peak at 0.4 V is typically understood to be the conversion reaction from MoS_2 to Mo metal and the formation of Li_2S.[13–17,21] In other reports of amorphous MoO_2, a peak at 0.5 V has been observed and corresponds to the intercalation of Li^+ into the defect sites in MoO_2 and MoO_3.[27] As P. MoS_2 electrodes contain a significant amount of O in the intermediate layer, this peak centered on 0.4 V is likely a combination of two reductions: Li^+ intercalation into the defect sites in amorphous MoO_2 and MoO_3 at 0.5 V; and the conversion of Li_xMoS_2 to Mo metal and Li_2S at 0.3 V. These and the following predictions are summarized in Table 1.

On the first charge scan (in the anodic (+) direction from 0 V, during which delithiation is expected) there are peaks at 1.5 V and 2.25 V. The peak at 2.25 V is a commonly observed MoS_2 peak corresponding to the decomposition of Li_2S to S_n^{2-}.[13–17] On the other hand, the peak at 1.5 V is not typical in MoS_2 materials but has been observed in amorphous MoO_2 and MoO_3 materials; it is understood to arise from the removal of the Li^+ from MoO_2 and MoO_3.[27–29] This peak is also observed in low-current CVs of Mo foil in Figure 4, so it is likely due to native MoO_x. Notably missing from the sweeps is a significant peak at 1.7 V corresponding to the deintercalation of Li^+ from MoS_2,[13] which could be due to the almost complete conversion of Li_xMoS_2 to Li_2S and Mo during the first discharge.
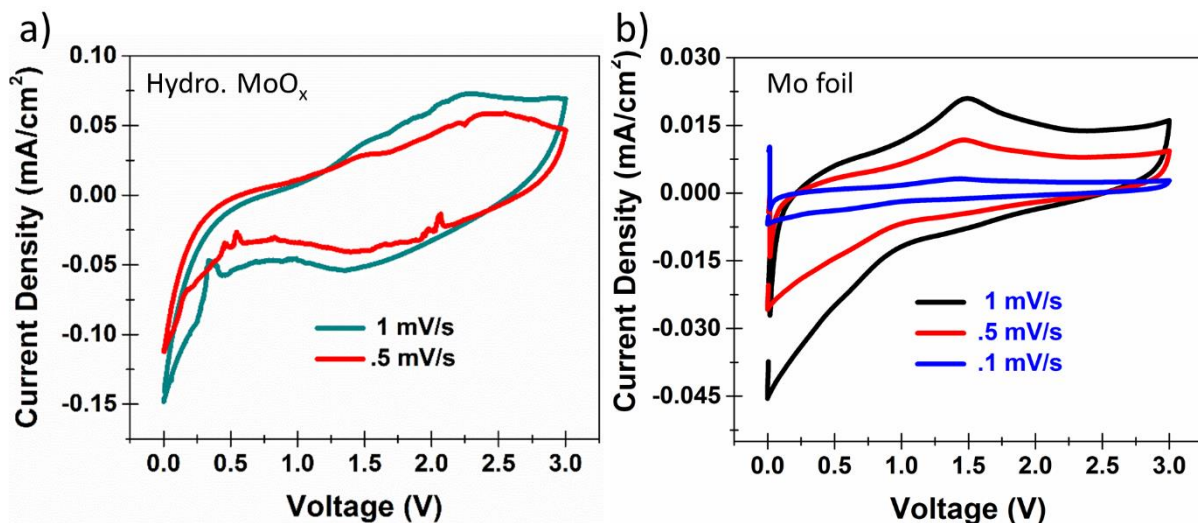
Figure 4. CV measurements of hydrothermally synthesized MoO$_x$ (a) and pure Mo foil (b) at varying scan rates.

On subsequent cathodic scans, the Li$_2$S formation peak at 1.9 V appears, the cathodic intercalation peak at 0.9 V remains unchanged, and the peak at 0.4 V disappears, leaving only the 0.5 V peak. The disappearance of the 0.4 V peak indicates that the solid-electrolyte interphase (SEI) was formed at this potential during the initial discharge.[30] From the discussion above, the SEI is likely comprised of a significant amount of Li$_2$S and Mo metal which is not reversed in the corresponding anodic scan but is instead used in the Li$_2$S/polysulfide redox pair at 1.9 V/2.25 V.

Figure 3c shows the charge/discharge behavior of these petaled MoS$_2$ electrodes. Along the discharge curve there is both a plateau at about 1.9 V and at about 0.5 V consistent with the CV curves in Figure 3b. The charging curve is also consistent with the CV curve in Figure 3b with the conversion plateau at 1.4 V and the polysulfide reduction plateau at 2.2 V. The material shows a maximum capacity of 3.8 mAh/cm^3, which we estimate corresponds to 825 mAh/g at 0.01 mA/cm^2. In addition to the excellent capacity of the material, Figure 5 shows that the material has excellent rate capability maintaining a volumetric capacity greater than 1.5 mAh/cm^3 (> 300mAh/g) even at current densities as high as 1 mA/cm^2.
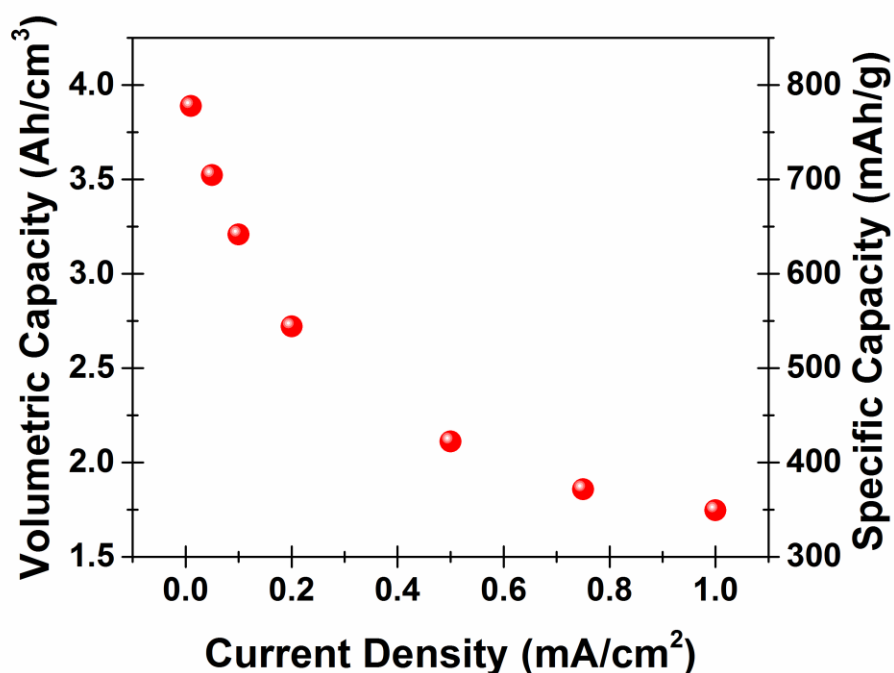
Figure 5. Capacity vs. charging current for a petaled MoS_2 battery, representing the rate capability of the petaled MoS_2 material.

Although the material may be useable as an anode for LIBs, the inefficiency in energy storage evidenced by the large voltage split between the 0.5 V/1.5 V pair suggests that this material is more likely to be useful as a cathode material. Thus, long-term, high-voltage cycling was performed in the potential range around the polysulfide peak (1.5 - 3 V), the relevant voltage regime for a cathode material. When cycled in this region at 0.01 mA/cm^2 (Figure 3d), the material exhibited excellent capacity retention, maintaining over 90% of the original capacity for over 200 cycles. As the high voltage peak only corresponds to the MoS_2, we estimated the capacity based on the approximate mass of the MoS_2, finding that it maintained about 350 mAh/g MoS_2.

To elucidate the processes that occur during cycling, we performed *ex situ* characterization of the P. MoS_2 electrodes. We analyzed pristine, charged and discharged P. MoS_2 electrodes for morphology, chemical content, and crystal phases using TEM-EDS (Figure 6) and glancing-angle X-Ray Diffraction (GAXRD, Figure 7). Two electrodes were cycled at least five times until reversible CVs were obtained, then one was allowed to discharge to 5 mV and removed ("discharged") and the other was charged to 3.0 V and removed ("charged"). The electrodes were exfoliated using a stainless steel razor blade, the material sonicated in solvent, then deposited on TEM grid and allowed to dry.
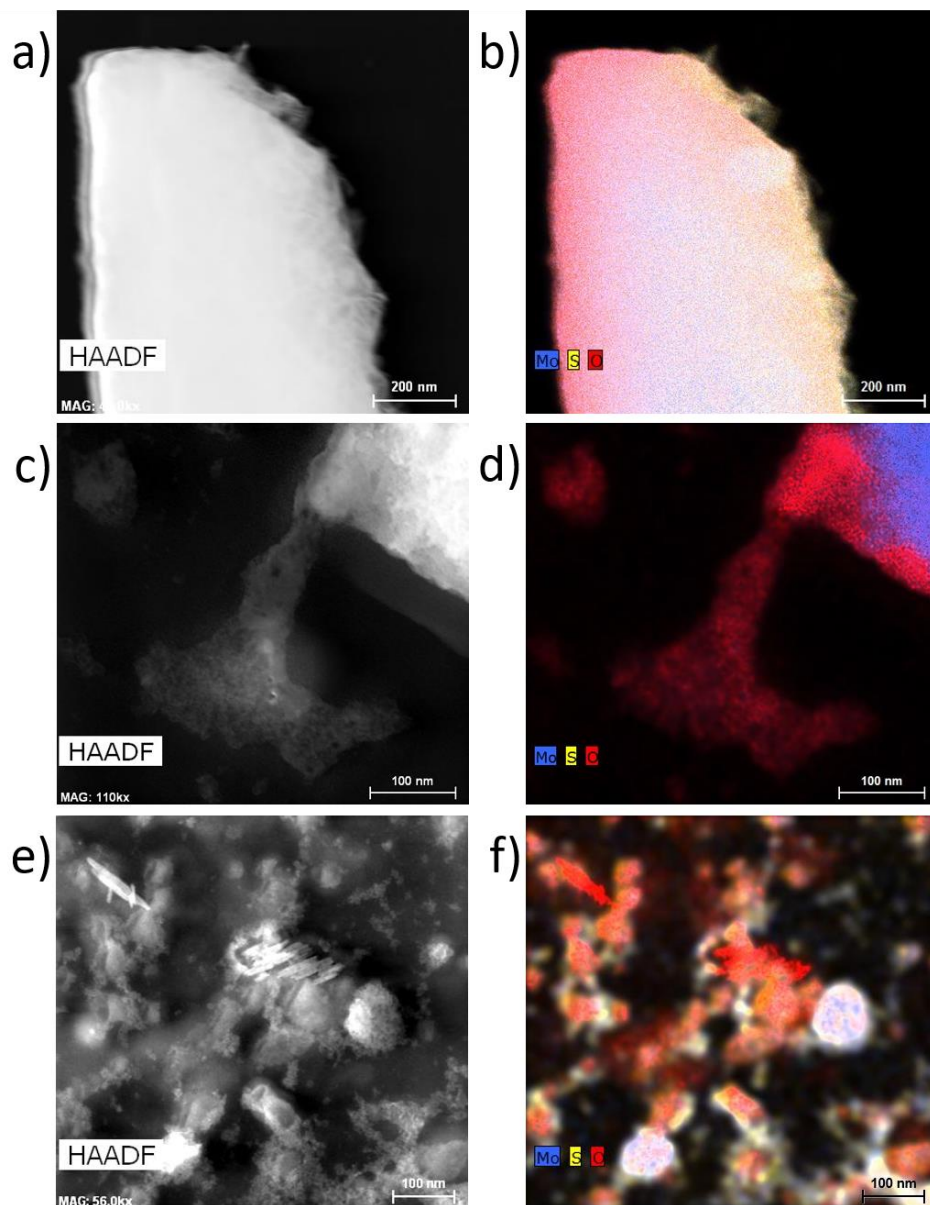
Figure 6. HAADF-TEM images (left) with accompanying EDS maps (right) of P. MoS_2/Mo: (a, b) pristine, (c, d) discharged, and (e, f) charged.

The image of pristine P. MoS_2 in Figure 6a shows a cross-section of P. MoS_2/MoS_xO_y with the top petals on the right side of the image and the MoS_xO_y on the left side of the image. It can be observed that the O (red) content is highest in the intermediate layer on the left side, then rapidly decreases toward the petals, but S (yellow) is most clearly seen in the petals. Mo (blue) is observed throughout the material as evidenced by the purple hue of the O-rich area and the slight green hue of the S-rich area. In the discharged electrode (Fig. 6 c,d),

a combination of large, Mo-rich slabs and curly, O-rich petals can be observed, but no S is measured. The lack

of S is likely due to the formation of Li_2S, which dissolves in the ethylene carbonate solvent and does not

remain immobilized on the electrode. The material is likely a combination of metallic Mo and Li_4MoO_5, as

evidenced in the following GAXRD analysis. In Figure 6 (e,f) , a representative sample of the charged material

can be seen, which is primarily composed of small MoO_3 slabs and Mo and S_n^{2-} clusters. This is not surprising,

as MoS_2, S_n^{2-}, and delithiated MoO_x are expected at this stage.

The GAXRD results (Figure 7) are most illuminating as to the processes occurring as the battery is

cycled. The Mo foil diffractogram is shown in black with two major reflections at 40.5° and 58.6° 2θ and some

minor species with the approximate stoichiometry of MoO_3 (Mo_xO_{3x-y}) noted. Pristine P. MoS_2 is shown in red

where the Mo reflections dominate the measurement. There is a low, broad increase in the intensity from ~32-

38° where reflections from hexagonal (2H-) and rhombohedral (3R-) MoS_2 are expected, as well as Mo_xO_{3x-y}

and monoclinic MoO_2. The low, broad signal in this region indicates that the MoS_2 has low crystallinity. If it

was highly crystalline, one would expect a larger number of distinguishable peaks matching 2H-MoS_2. In the

discharged P. MoS_2 electrode (blue), the relative intensities of 2H-MoS_2 and metallic Mo reflections at 39.65°,

40.5°, and 58.6° are maintained, but new reflections from Mo_xO_{3x-y} and lithiated molybdates ($Li_xMo_yO_z$)

appear. The Mo_xO_{3x-y} reflections are different from those measured in pristine P. MoS_2. The charged P. MoS_2

electrode is shown in green and is the only electrode where metallic Mo reflections are not the highest intensity.

Rather, the Mo reflections are small and have been dwarfed by Mo_xO_{3x-y} ($Mo_{17}O_{47}$ (5 1 0), JCPDS Card No. 13-

0345) as the strongest reflection. Additionally, the MoS_2 reflections have not changed significantly and the

$Li_xMo_yO_z$ reflections are fewer.
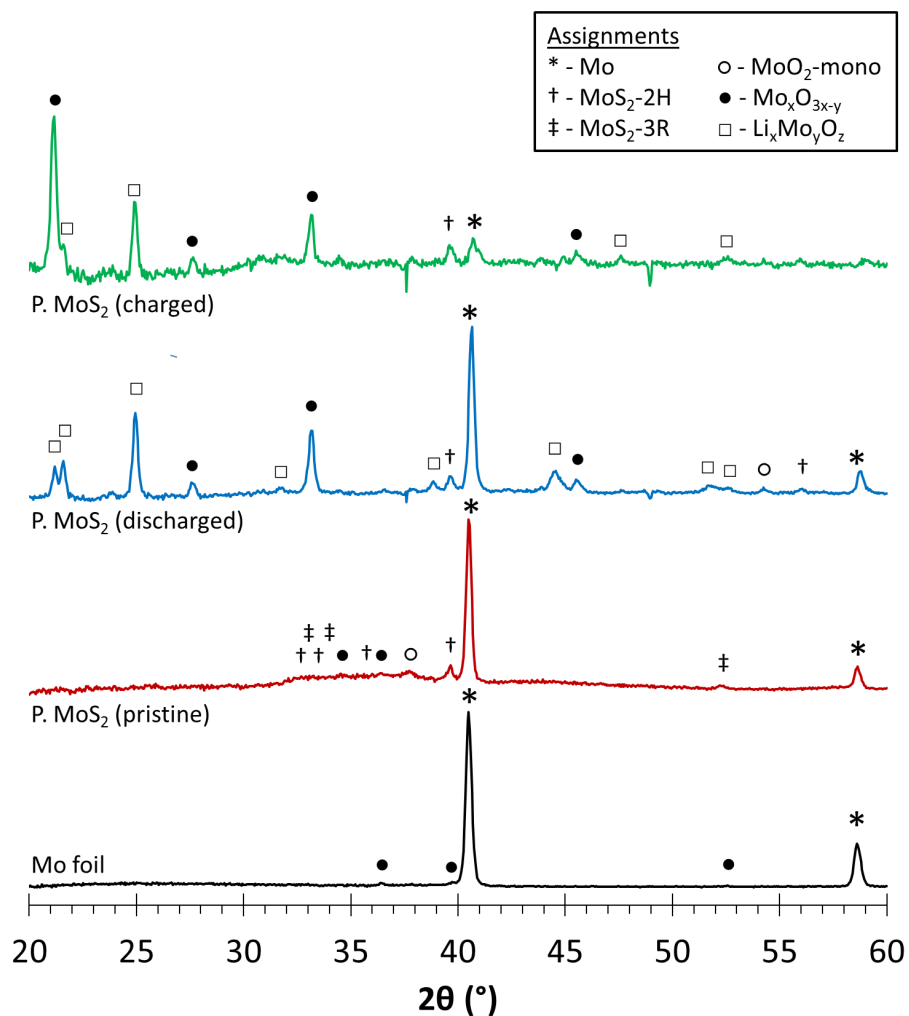
Figure 7. GAXRD comparison of pristine (red), discharged (blue), and charged (green) P. MoS$_2$/Mo electrodes as well as Mo foil (black). Assignments from JCPDS Cards: 42-1120 (Mo), 37-1492 (MoS$_2$-2H), 17-0744 (MoS$_2$-3R), 05-0452 (MoO$_2$-monoclinic); Mo$_x$O$_{3x-y}$ and Li$_x$Mo$_y$O$_z$ are groups of multiple JCPDS cards sharing the same generic formula, exhaustively listed in Table 2.

Table 2. Comprehensive list of categorized JCPDS cards used in GAXRD assignment.

Group (symbol) used in Fig. 7	Formula	JCPDS Card No.	Found in (m, d, c)*
Mo_xO_{3x-y} (●)	$Mo_{17}O_{47}$	13-0345	m, d, c
	MoO_3-orthorhombic	35-0609	m
	MoO_3-hexagonal	21-0569	d, c
$Li_xMo_yO_z$ (□)	$Li_4Mo_5O_{17}$	25-0492	d, c
	$Li_{0.62}MoO_{2.87}$	37-1450	d, c
	$Li_2Mo_4O_{13}$	25-0494	d, c
	$Li_{0.1}Mo_4O_7$	38-0071	d
	β-Li_4MoO_5	21-0511	d, c
	γ-Li_4MoO_5	21-0509	d
	$Li_{0.042}MoO_3$	38-0645	d
	$LiMo_8O_{10}$	42-0322	d
	β-Li_2MoO_3	21-0515	c
	Li_2MoO_4	12-0763	d, c
	$Li_{1.3}Mo_3O_8$	37-0249	d

m – Mo foil, d – Discharged P. MoS2, c – Charged P. MoS2

It is apparent from these data that the primary electrochemistry occurring during charge-discharge is the conversion between MoO_3 and Mo metal and is detected in CVs by the 1.5 V/0.5 V peak pair, contrary to initial assumptions that this peak pair arose from lithiation/delithiation of MoO_x defects. The secondary electrochemical reaction is the S_n^{2-}/Li_2S conversion at 2.25 V/1.9 V, but these products are either soluble in the electrolyte solution or amorphous, so they are not observed in GAXRD. Lithiation and delithiation of Mo_xO_{3x-y} and MoS_2 are minor or nonexistent, respectively, as evidenced from the small or negligible change in these crystalline materials between discharged and charged states. From the TEM-EDS and GAXRD data, it appears that while the petal morphology is somewhat maintained during cycling, it only acts as a structural support for reversible Mo-MoO_3 conversion. The results of this analysis are summarized in Figure 8.
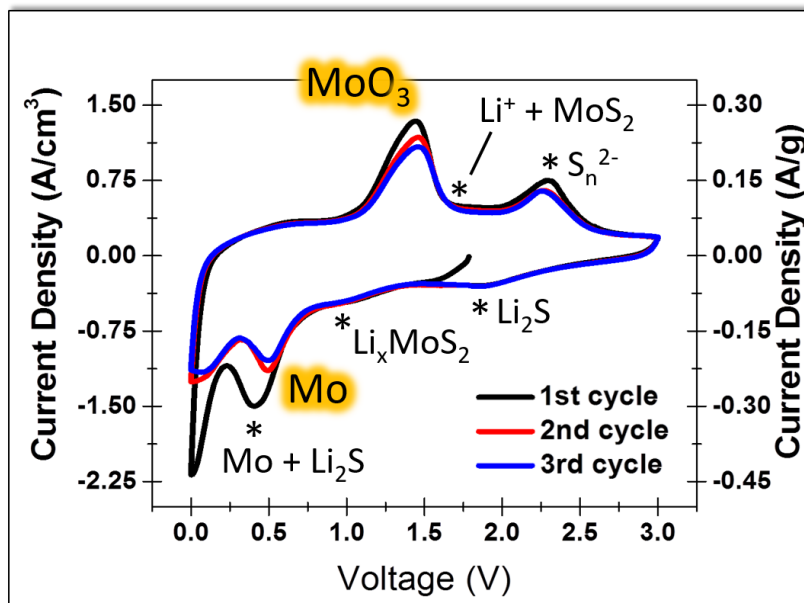
Figure 8. CV of P. MoS$_2$ with assignments of species formed at each voltage. From reference 13, with highlighted assignment from this work.

Conclusions

In summary, we have studied the use of a one-step hydrothermal synthesis to develop self-supported electrodes for LIB applications. We observe that the material exhibits three energy storage mechanisms: first, the conversion of MoS$_2$ and MoO$_x$ to Mo metal, Li$_x$Mo$_y$O$_z$, and Li$_2$S; second, the oxidation of Mo to MoO$_3$ and partial delithiation of Li$_x$Mo$_y$O$_z$; and third, the formation/reduction of polysulfides. The dominant, reversible reaction is the conversion between Mo and MoO$_3$. The unique petaled structure and large, intermediate, MoS$_x$O$_y$ layer provide high surface area and O to support the Mo-MoO$_3$ and Li$_2$S-S$_n^{2-}$ conversion reactions. The material exhibits a maximum capacity of 3.8 mAh/cm^3 (~825 mAh/g). Isolating the polysulfide formation/reduction mechanism by cycling from 1.5 - 3.0 V results in a high voltage capacity of 0.42 mAh/cm^3 (350 mAh/g MoS$_2$). The material also shows high rate capability and excellent cycle stability for the high voltage polysulfide reactions. This material presents itself as a self-supported structure for LIBs where the O supplied by the intermediate layer leads to intermediate-voltage conversion reactions. In the future, research

efforts should be dedicated to adapting this hydrothermal synthetic technique to prepare other, layered, self-supported electrode materials such as $LiCoO_2$ for energy storage platforms.

References

(1)   Dudney, N. J. Solid-State Thin-Film Rechargeable Batteries. In *Materials Science and Engineering B: Solid-State Materials for Advanced Technology*; 2005; Vol. 116, pp 245–249.

(2)   Golodnitsky, D.; Nathan, M.; Yufit, V.; Strauss, E.; Freedman, K.; Burstein, L.; Gladkich, A.; Peled, E. Progress in Three-Dimensional (3D) Li-Ion Microbatteries. *Solid State Ionics* **2006**, *177* (26–32 SPEC. ISS.), 2811–2819.

(3)   Long, J. W.; Dunn, B.; Rolison, D. R.; White, H. S. Three-Dimensional Battery Architectures. **2004**.

(4)   Nathan, M.; Golodnitsky, D.; Yufit, V.; Strauss, E.; Ripenbein, T.; Shechtman, I.; Menkin, S.; Peled, E. Three-Dimensional Thin-Film Li-Ion Microbatteries for Autonomous MEMS. *J. Microelectromechanical Syst.* **2005**, *14* (5), 879–885.

(5)   Roberts, M.; Johns, P.; Owen, J.; Brandell, D.; Edstrom, K.; El Enany, G.; Guery, C.; Golodnitsky, D.; Lacey, M.; Lecoeur, C.; Mazor, H.; Peled, E.; Perre, E.; Shaijumon, M. M.; Simon, P.; Taberna, P.-L. 3D Lithium Ion Batteries—from Fundamentals to Fabrication. *J. Mater. Chem.* **2011**, *21* (27), 9876.

(6)   Ellis, B. L.; Knauth, P.; Djenizian, T. Three-Dimensional Self-Supported Metal Oxides for Advanced Energy Storage. *Adv. Mater.* **2014**, *26* (21), 3368–3397.

(7)   Cheah, S. K.; Perre, E.; Rooth, M.; Fondell, M.; Hårsta, A.; Nyholm, L.; Boman, M.; Gustafsson, T.; Lu, J.; Simon, P.; Edström, K. Self-Supported Three-Dimensional Nanoelectrodes for Microbattery Applications. *Nano Lett.* **2009**, *9* (9), 3230–3233.

(8)   Taberna, P. L.; Mitra, S.; Poizot, P.; Simon, P.; Tarascon, J.-M. High Rate Capabilities Fe_3O_4-Based Cu Nano-Architectured Electrodes for Lithium-Ion Battery Applications. *Nat. Mater.* **2006**, *5* (7), 567–573.

(9)   Ko, Y.-D.; Kang, J.-G.; Park, J.-G.; Lee, S.; Kim, D.-W. Self-Supported SnO_2 Nanowire Electrodes for High-Power Lithium-Ion Batteries. *Nanotechnology* **2009**, *20* (45), 455701.

(10)   Yoffe, A. D. No Title. In *Physics and Chemistry of Electrons and Ions in Condensed Matter*; Springer, 1984; pp 437–458.

(11)   Haering, R. R.; Stiles, J. A.; Brandt, K. Lithium Molybdenum Disulphide Battery Cathode, 1979.

(12)   Whittingham, M. S. Lithium Batteries and Cathode Materials. **2004**.

(13)   Stephenson, T.; Li, Z.; Olsen, B.; Mitlin, D. Lithium Ion Battery Applications of Molybdenum Disulfide (MoS_2) Nanocomposites. *Energy Environ. Sci.* **2014**, *7* (1), 209–231.

(14)   Chang, K.; Chen, W. L -Cysteine-Assisted Synthesis of Layered MoS_2/Graphene Composites with Excellent Electrochemical Performances for Lithium Ion Batteries. *ACS Nano* **2011**, *5* (6), 4720–4728.

(15)   Chang, K.; Chen, W. In Situ Synthesis of MoS_2/graphene Nanosheet Composites with Extraordinarily High Electrochemical Performance for Lithium Ion Batteries. *Chem. Commun.* **2011**, *47* (14), 4252.

(16)   Hwang, H.; Kim, H.; Cho, J. MoS_2 Nanoplates Consisting of Disordered Graphene-like Layers for High Rate Lithium Battery Anode Materials. *Nano Lett.* **2011**, *11* (11), 4826–4830.

(17)   Xiao, J.; Choi, D.; Cosimbescu, L.; Koech, P.; Liu, J.; Lemmon, J. P. Exfoliated MoS_2 Nanocomposite as an Anode Material for Lithium Ion Batteries. *Chem. Mater.* **2010**, *22* (16), 4522–4524.

(18)   Sen, U. K.; Mitra, S. High-Rate and High-Energy-Density Lithium-Ion Battery Anode Containing 2D MoS_2 Nanowall and Cellulose Binder. *ACS Appl. Mater. Interfaces* **2013**, *5* (4), 1240–1247.

(19)   Albiter, M. A.; Huirache-Acuña, R.; Paraguay-Delgado, F.; Rico, J. L.; Alonso-Nuñez, G. Synthesis of MoS_2 Nanorods and Their Catalytic Test in the HDS of Dibenzothiophene. *Nanotechnology* **2006**, *17* (14), 3473–3481.

(20)   Berntsen, N.; Gutjahr, T.; Loeffler, L.; Gomm, J. R.; Seshadri, R.; Tremel, W. A Solvothermal Route to High-Surface-Area Nanostructured MoS_2. **2003**.

(21)   Zhang, C.; Wang, Z.; Guo, Z.; Lou, X. W. (David). Synthesis of MoS_2–C One-Dimensional Nanostructures with Improved Lithium Storage Properties. *ACS Appl. Mater. Interfaces* **2012**, *4* (7),

3765–3768.

(22) Mdleleni, M. M.; Hyeon, T.; Suslick, K. S. Sonochemical Synthesis of Nanostructured Molybdenum Sulfide. **1998**.

(23) Finn, S. T.; Macdonald, J. E. Petaled Molybdenum Disulfide Surfaces: Facile Synthesis of a Superior Cathode for QDSSCs. *Adv. Energy Mater.* **2014**, *4*.

(24) Finn, S. T.; Macdonald, J. E. Contact and Support Considerations in the Hydrogen Evolution Reaction Activity of Petaled MoS_2 Electrodes. *ACS Appl. Mater. Interfaces* **2016**, *8* (38), 25185–25192.

(25) Yang, L.; Liu, L.; Zhu, Y.; Wang, X.; Wu, Y. Preparation of Carbon Coated MoO_2 Nanobelts and Their High Performance as Anode Materials for Lithium Ion Batteries. *J. Mater. Chem.* **2012**, *22* (26), 13148.

(26) Li, W.; Cheng, F.; Tao, Z.; Chen, J. Vapor-Transportation Preparation and Reversible Lithium Intercalation/deintercalation of α-MoO_3 Microrods. *J. Phys. Chem. B* **2006**, *110*, 119–124.

(27) Jang, J.; Kim, S.-M.; Kim, Y.; Park, K. H.; Ku, J. H.; Ryu, J. H.; Oh, S. M. Electrode Performances of Amorphous Molybdenum Oxides of Different Molybdenum Valence for Lithium-Ion Batteries. *Isr. J. Chem.* **2015**, *55* (5), 604–610.

(28) Ju, X.; Ning, P.; Tong, X.; Lin, X.; Pan, X.; Li, Q.; Duan, X.; Wang, T. H_xMoO_3 Nanobelts with Better Performance as Anode in Lithium-Ion Batteries. *Electrochim. Acta* **2016**, *213*, 641–647.

(29) Lu, K.; Xu, J.; Zhang, J.; Song, B.; Ma, H. General Preparation of Three-Dimensional Porous Metal Oxide Foams Coated with Nitrogen-Doped Carbon for Enhanced Lithium Storage. *ACS Appl. Mater. Interfaces* **2016**, *8* (27), 17402–17408.

(30) Verma, P.; Maire, P.; Novák, P. A Review of the Features and Analyses of the Solid Electrolyte Interphase in Li-Ion Batteries. *Electrochim. Acta* **2010**, *55* (22), 6332–6341.

A Cu_2S@SnS Core@Shell Structure via SnS@Cu_2S Cation Exchange and its Photovoltaic Performance.[*]

Introduction

Synthesis of nanoscale materials has made great strides and a wide variety of nanoscale materials with variable shape, size, morphology, phase, and composition have been reported in the literature.[1–7] Cation exchange has emerged as a rational synthetic approach for achieving nanomaterials with complex architectures[8–10] such as dot-in-rods of ZnSe/ZnS and Cu_2Se/Cu_2S,[11] as well as PbSe/PbS,[12] that are almost inaccessible by using conventional colloidal synthetic techniques with either a bottom-up or top-down approach.[13–16] Cation exchange can substantially influence the physical and optoelectronic properties of the nanomaterials,[17–20] as well as produce metastable phases of materials in the nanoscale size regime.[21,22] Further, Manna *et al.* have shown that cation exchange can allow the selective chemical transformation of the nanostructures based on the reactivity of the foreign ions towards the different domains present in the pristine lattice.[23] Cation exchange is typically a post-synthetic modification in which foreign cations are introduced into pre-synthesized nanocrystals, and the extent of exchange is externally tuned, mainly by foreign cation concentration. Depending on the extent of exchange, doped,[18,24,25] alloyed,[16,26,27] core@shell,[28–30] heterostructured[12,15,31] or completely exchanged[12,21,32] nanocrystals can be obtained while retaining shape, size and often crystal structure. This retention of desired properties is based upon the reactivity of the foreign cation(s) as well as the miscibility of the product phase in the pristine lattice.[11,12,16,33] Cation exchange with

---

[*] This chapter has been adapted from a manuscript in preparation by Sarkar, S., Finn, S., & Macdonald, J., Vanderbilt University, 2017.

different types of nanostructures having variable size, morphology, and phase has already been investigated.[8–10,13–16] Mechanistic details such as the accommodation of a foreign ion into a high-mismatch lattice and the crystallographic orientation of the product phase in the pristine lattice have been elucidated in other work.[22,34,35]

When a foreign cation experiences high lattice mismatch in the pristine lattice during the exchange process, it forms a separate domain with a distinct phase boundary, sharing the rigid anion sublattice of the pristine nanocrystals.[36–39] Nevertheless, the reactant and product phases share a common interface with high lattice strain, making a crystallographically complex nanostructure. However, the formation of a distinct boundary between different materials offers the opportunity for integrating multiple functionalities into a single building block for a variety of applications and is fundamentally important for investigating the electronic coupling between the two nanoscale components. A limited number of such cation exchange processes are also reported to form a void in the structure due to the large difference in the inward and outward diffusion flux of the selected cations.[40,41] Nanocrystals with voids, owing to the large surface area and low material density, are of immense interest due to their potential application in nanoreactors,[42] drug delivery,[43] energy storage,[44] catalysis,[45] gas sensing,[46] etc. Hence, investigating a cation exchange process in such a system with high lattice mismatch is not only fundamentally challenging, but also highly important for producing desirable nanomaterials for many applications in current demand.

A classic example of cation exchange, $Cu_2X \rightarrow SnX$ (X= S, Se or Te), with high lattice mismatch has been reported previously.[27,28,37] Here, we investigated the reverse cation exchange process employing Cu^+ as foreign ion and SnS as the pristine lattice. We investigated the process with variable sizes of SnS nanocubes, and found that the Cu^+ can only exchange with the surface Sn^{2+} at lower temperature at the initial stage of the reaction, resulting in a shell of Cu_2S around the SnS. However, on increasing the temperature, Cu^+ infiltrates the lattice extremely fast, thrusting Sn^{2+} out of the core of the SnS nanocube, transforming the $SnS@Cu_2S$ to a $Cu_2S@SnS$ nanocube. Also, comparative photovoltaic tests have been conducted with the pristine SnS and both types of core@shell nanocubes as both the $SnS@Cu_2S$ and $Cu_2S@SnS$ nanocubes absorb light in the visible

region of the solar spectrum. Mechanistic details of the SnS→Cu$_2$S@SnS chemical process and its tunability will be discussed in a forthcoming publication.

Experimental

Tin(II) chloride (SnCl$_2$, 99.99%), thiourea ($\geq$ 99.0%), hexadecylamine (HDA, tech., 97%) oleylamine (OlAm, Aldrich, 70%), tri-butylphosphine (TBP, tech., 97%), Copper (I) chloride (CuCl, 97%) were purchased from Sigma Aldrich. All chemicals were used as received without further purification.

Cu$^+$ Exchange of SnS Nanocubes

The first step of this process is a synthesis of SnS nanocube, and the second step is Cu$^+$ treatment to the nanocubes *in situ*.

Synthesis of 53 ± 5 nm SnS nanocubes: nanocubes of SnS have been synthesized following a modified literature method.[1] In a round bottom three neck flask, 38 mg (0.2 mmol) SnCl$_2$ and 2 gm HDA were loaded. The mixture was placed under vacuum for 30 min at 100°C. It turned turbid light brown solution. Then, 1 ml TBP (kept under N$_2$ atmosphere) was injected into the solution, and the temperature of the reaction mixture was further raised to 190°C with a heating rate of 15°C/min to get a transparent solution. Then, the reaction mixture was allowed to cool down to 175°C, and a hot solution of thiourea (12 mg) dissolved in HDA (1 g) (through gentle heating under inert atmosphere) was injected in to the reaction mixture at 175°C. The reaction solution turned deep brown immediately after the injection, indicating the formation of SnS nanocubes. After 1 min the

solution was slowly (15°C/min) cooled down to 155°C and annealed for a total time of 20 min. It was further cooled down to 100°C for injection of the Cu$^+$ solution.

Cu$^+$ addition to the 53 ± 5 nm SnS nanocubes: After cooling down the reaction solution to 100°C, 2.6 mL of crude solution was removed, and a solution of CuCl (45 mg) dissolved in 2 ml of oleylamine under inert atmosphere was injected into the reaction mixture. Then the temperature of the reaction solution was raised to 170°C (20°C/min). Aliquots were collected at the different time points, while raising the temperature to 170°C.

Synthesis of 22 ± 3 nm SnS nanocubes: In a round bottom three neck flask, 38 mg (0.2 mmol) SnCl$_2$ and 2 gm HDA were loaded. The mixture was placed under vacuum for 30 min at 100°C. It also turned a turbid, light brown color. Then, 1 mL TBP (kept under N$_2$ atmosphere) was injected into the solution, and the temperature of the reaction mixture was further raised to 190°C with a heating rate of 15°C/min until the solution turned transparent. The reaction mixture was then allowed to cool down to 160°C, and a hot solution of thiourea (39 mg) dissolved in HDA (1.4 g) (through gentle heating under inert atmosphere) was injected in to the reaction mixture at 160°C. The solution turned deep brown immediately after the injection. It was annealed at the same temperature for a min, after that, it was slowly (15°C/min) cooled down to 155°C, and annealed for a total time of 20 min to get the desired size of SnS nanocube. It was further cooled down to 100°C for Cu$^+$ treatment.

Cu$^+$ addition to the 23 ± 3 nm SnS nanocubes: After cooling down the reaction solution to 100°C, 3.2 ml of crude solution was taken out, and a solution of CuCl (45 mg) dissolved in 2 ml of oleylamine under inert atmosphere was injected into the reaction mixture. Then the temperature of the reaction solution was raised to 170°C (20°C/min). Aliquots were collected at the different time points, while raising the temperature to 170°C.

Optical Spectroscopy

Absorbance spectra of the purified samples were collected using a UV-visible spectrophotometer (Jasco V-670). Photoluminescence spectra were collected using a spectrofluorometer (Jasco FP-8300) with 348 nm excitation wavelength.

TEM

Transmission electron microscopy (TEM) images were collected and energy dispersive X-ray spectroscopy (EDS) was carried out using a FEI Tecnai Osiris digital 200 kV S/TEM system. TEM samples were prepared by drop-casting a dilute solution of the nanostructures dispersed in hexanes onto a carbon coated nickel grid and drying in air at room temperature.

QDSSC Preparation and Testing

Preparation, assembly, and testing of quantum dot sensitized solar cell (QDSSC) components including TiO_2/FTO photoanodes, polysulfide electrolyte, and P. MoS_2/Mo counter electrodes were carried out exactly as previously described[47,48] with some changes. These changes include deposition of the photoabsorber quantum dots, successive ionic layer adsorption and reaction (SILAR) of the protective ZnS layer (no CdS), and linear sweep voltammetric (LSV) scan rate of photovoltaic measurements was 50 mV/s.

The nanocubes were deposited onto TiO_2/FTO via electrophoretic deposition (EPD). A ~50 mg dry sample of nanocubes was suspended in 5 mL chloroform with 1 drop of oleylamine, then sonicated for several

minutes until dispersed. A TiO$_2$/FTO electrode and bare FTO electrode were attached to (-) and (+) leads, respectively, then suspended in the nanocube solution. A Keithley 2400 SourceMeter was used to apply 200 V to the system for 20 min. Once nanocubes were deposited onto TiO$_2$/FTO, the photoanode was rinsed with toluene, then the surface excluding the TiO$_2$ area was wiped with a Kimwipe. Typical loading of nanoparticles was 0.46 mg cm^{-2} Cu$_2$S@SnS and 1.2 mg cm^{-2} SnS@Cu$_2$S.

After nanocube deposition, a protective ZnS layer was applied via SILAR: photoanodes were dipped in 0.1 M Zn(NO$_3$)$_2$ (Strem) in methanol, rinsed with methanol, dried, dipped in 0.1 M Na$_2$S·9H$_2$O in 1:1 methanol:water, rinsed, and dried; 2 of these cycles were repeated per photoanode, then photoanodes were stored in the dark.

Results & Discussion

SnS nanocubes have been synthesized following a modified literature method.[49] Typically, thiourea dissolved in HDA (hexadecylamine) was injected at a particular temperature in a solution of SnCl$_2$ in HDA and TBP, and annealed for 20 min at an optimized temperature to synthesize the SnS nanostructures, the schematic representation of which is shown in Scheme 1. In order to carry out the exchange process, various sizes of pristine nanostructures ranging from 25-50 nm were synthesized by varying the injection temperature, amount of anion precursor, and HDA.

Scheme 1. Reaction scheme of cation exchange process.
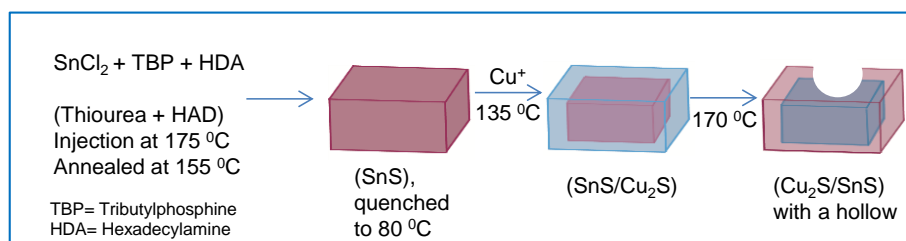
Specifically, the injection of the room-temperature liquid into the 175°C solution caused the reaction temperature to drop and the solution was maintained at 155°C for 20 min. SnS nanocubes could be isolated at this step (Figure 1a, nanocube length = 52 ± 5 nm, n = 120). XRD confirmed the phase to be the newly described cubic π-SnS[50,51] with a small amount of orthorhombic α-SnS (JCPDS# 39-0354) as an impurity (Figure 2). The π-SnS can be described as NaCl-type with ordered defects, and so has an FCC anion sub-lattice. High resolution TEM (Figure 1) shows that the nanocubes are single-crystalline. The lattice fringes indicate that the faces of the cuboids are the [400].
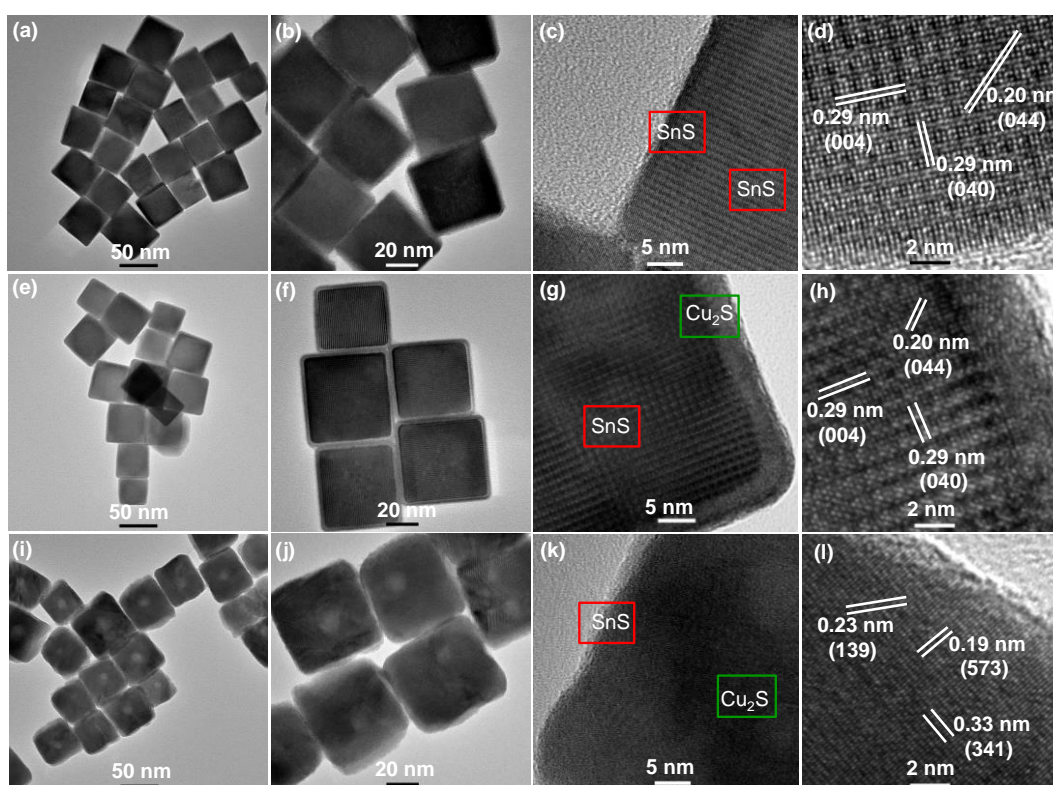
Figure 1. TEM and HR-TEM images of SnS nanocubes (a-d), SnS@Cu_2S nanocubes collected at 135 °C (e-h) and Cu_2S@SnS nanocubes collected at 175°C (i-l).

Cation exchange was performed without purification of the SnS nanocubes. The temperature of the reaction solution was reduced to 90°C, and a Cu^+ solution in oleylamine was injected into the reaction flask.

The temperature was then ramped to 170°C, and aliquots were collected at several temperatures to observe the exchange processes.

The TEM image of the early stage aliquot (Figure 1f) collected at 135°C after the copper injection shows a similar morphology to the pristine SnS nanocubes (Figure 1c) and the particles have a similar size (52 ± 5 nm, n = 120). HR-TEM paired with energy dispersive X-ray spectroscopy (EDS) indicate that the particles are composed of a SnS core with a copper-rich, 4-nm thick, mixed Cu-Sn-S shell (Figure 3). In some isolated areas of the shell, < 5nm crystallites could be observed with d = 0.3 nm, corresponding to the (101)-like reflections of a hexagonal $Cu_{2-x}S$ phase. The XRD pattern (Figure 2b) does not show additional reflections due to copper sulfide as these tiny crystallites are likely dwarfed by the more intense reflections of the π-SnS.
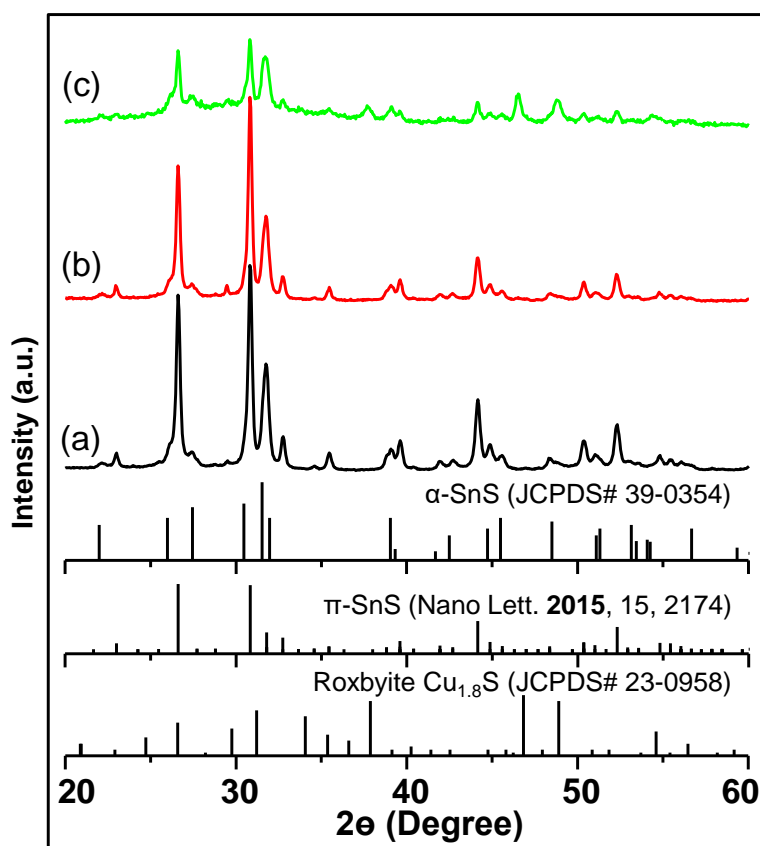
Fig 2. XRD at the different stages of the cation exchange reaction. (a, b, c) are the XRD for the pristine SnS, SnS@Cu$_2$S and Cu$_2$S@SnS, respectively.

XRD of the final $Cu_2S@SnS$ product shows additional reflections at 37.7°, 46.5° and 48.9°, characteristic of one of the hexagonal-like copper sulfides ($Cu_{2-x}S$). While there are several very similar phases of copper sulfide, we found the additional reflections are well-matched with roxbyite $Cu_{1.8}S$. Roxbyite features a distorted hcp anion lattice, indicating that there is a major structural transformation from cubic to hexagonal anion lattice upon cation exchange from Sn^{2+} to Cu^+. For ease of discussion, we will approximate the lattice assignments of the Cu_2S to that of a simple hexagonal structure. The reflections were accordingly assigned; 37.7° is the (102)-like planes, 46.5° (110)-like planes, and the 48.9° (103)-like planes. HR-TEM (Figure 1i-l) showed that the particles were single-crystalline. The crystallite size (40.7 nm) determined by Scherrer calculation (considering the peak at 46.5°) is closely matched with the HR-TEM. A pair of perpendicular lattice fringes were assigned to d = 0.33 nm as (100)-like planes, and d = 0.19 nm as (110)-like planes. A third set of fringes, d = 0.23 nm, was assigned to (102)-like planes. The aliquot of the ~23-nm nanocubes (this size was optimal for EPD) collected at 170°C after copper injection shows that the cubes have developed Cu_2S cores. EDS mapping indicates that the core is Cu_2S and the shell is SnS (Figure 4).
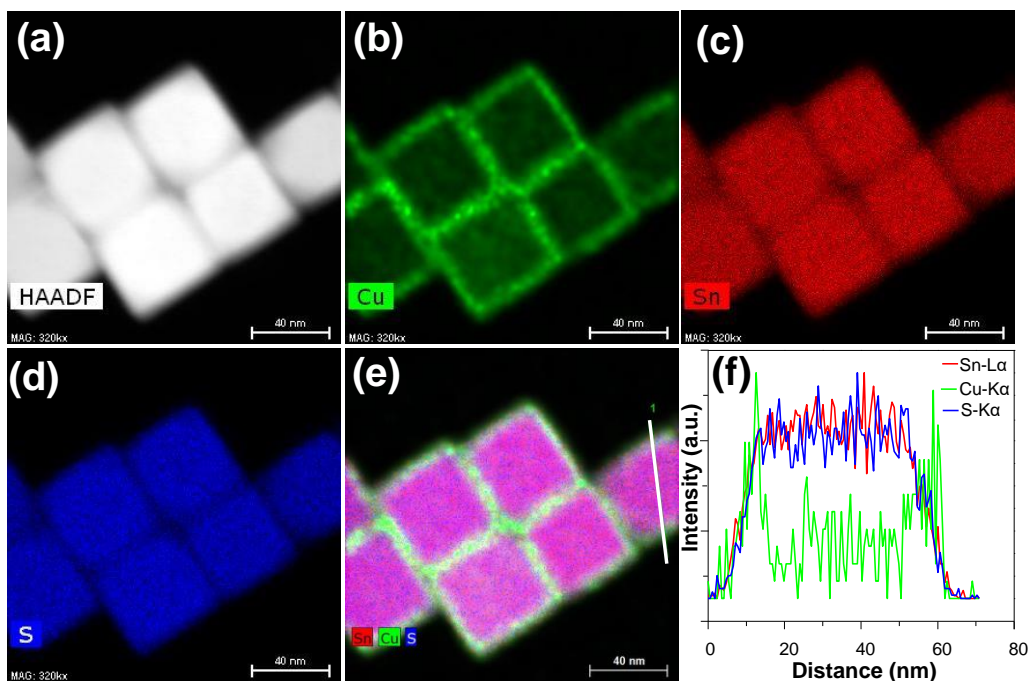
Figure 3. A) High Angle Annular Dark Field- Scanning Transmission Electron Microcopy (HAADF-STEM) image of the nanocubes collected at 135°C (b-e) EDS elemental mapping (f) relative EDS signal of Sn, Cu and S along the line noted in (e).
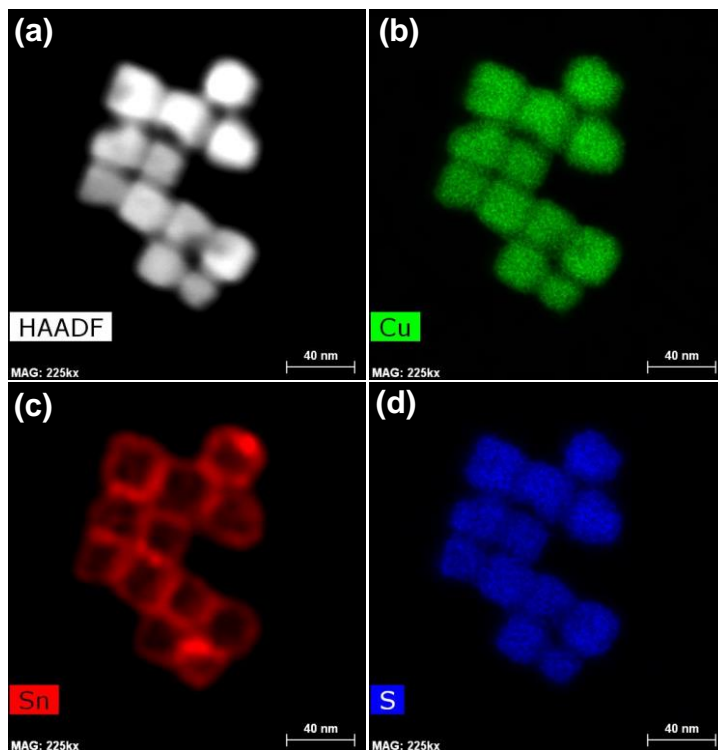
Fig 4. High Angle Annular Dark Field- Scanning Transmission Electron Microcopy (HAADF-STEM) image of the nanocubes (23 ± 2 nm, n = 120) collected at 170°C (b-d) EDS elemental mapping

What is most interesting about this reaction is that once multiple, very specific conditions are met (temperature, concentration of Cu^+ and coordinating ligands), Cu^+ rapidly moves into the SnS lattice, forcing Sn^{2+} out to form a SnS shell around a Cu_2S core. Performing this rapid Cu^+ exchange on roughly 25 nm, 50 nm, and 75 nm SnS nanocubes produces $Cu_2S@SnS$, $Sn@Cu_2S@SnS$, and $Void@Cu_2S@SnS$ heterostructures, respectively. More precise tuning of the SnS precursor nanocube size could result in a high level of control over the number, size, and composition of phases present. The coordinating ligands TBP and oleylamine are also found to play a pivotal role in the reaction based on their stabilizing interaction with Sn^{2+} and Cu^+, respectively, suggesting that other ligand chemistries may be explored to achieve high monodispersity and alternate product morphologies. These initial results are very exciting and present the field with a novel approach to synthesize heterostructured nanoparticles.

Photovoltaic Performance

Bulk SnS and Cu_2S have small band gaps (E_g) of 1.1 and 1.4 eV, respectively,[52,53] making them attractive photoabsorbers for solar photovoltaics. Furthermore, UV-Visible absorbance spectra of the synthesized nanocubes (Figure 5) indicate an absorbance onset in the near-IR with a first exciton peak around 500 nm and a broad absorbance over the visible range. Therefore, we conducted a comparative photovoltaic performance of the small pristine SnS, $SnS@Cu_2S$ and $Cu_2S@SnS$ core@shell nanocubes.
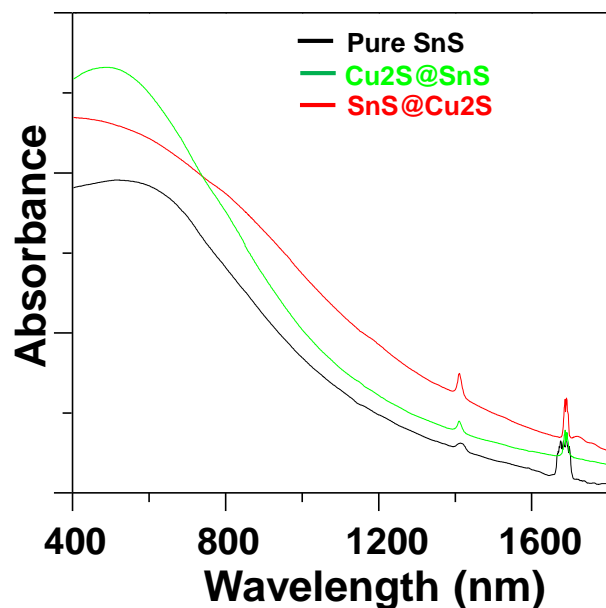
Figure 5. UV-vis of the aliquots collected at the different stages of the cation exchange reaction.

The various nanocube samples were tested as photoabsorbers in QDSSCs prepared according to previous work[47] and the results are presented in Figure 6a and Table 1. $Cu_2S@SnS$ nanocubes exhibit the highest short-circuit current density (J_{sc}), open-circuit potential (V_{oc}) and external power conversion efficiency (η), but the lowest fill factor (FF). While the performance of SnS and $SnS@Cu_2S$ are approximately the same, it is apparent that J_{sc}, V_{oc}, and η decrease when a Cu_2S shell is added to the SnS nanocubes.
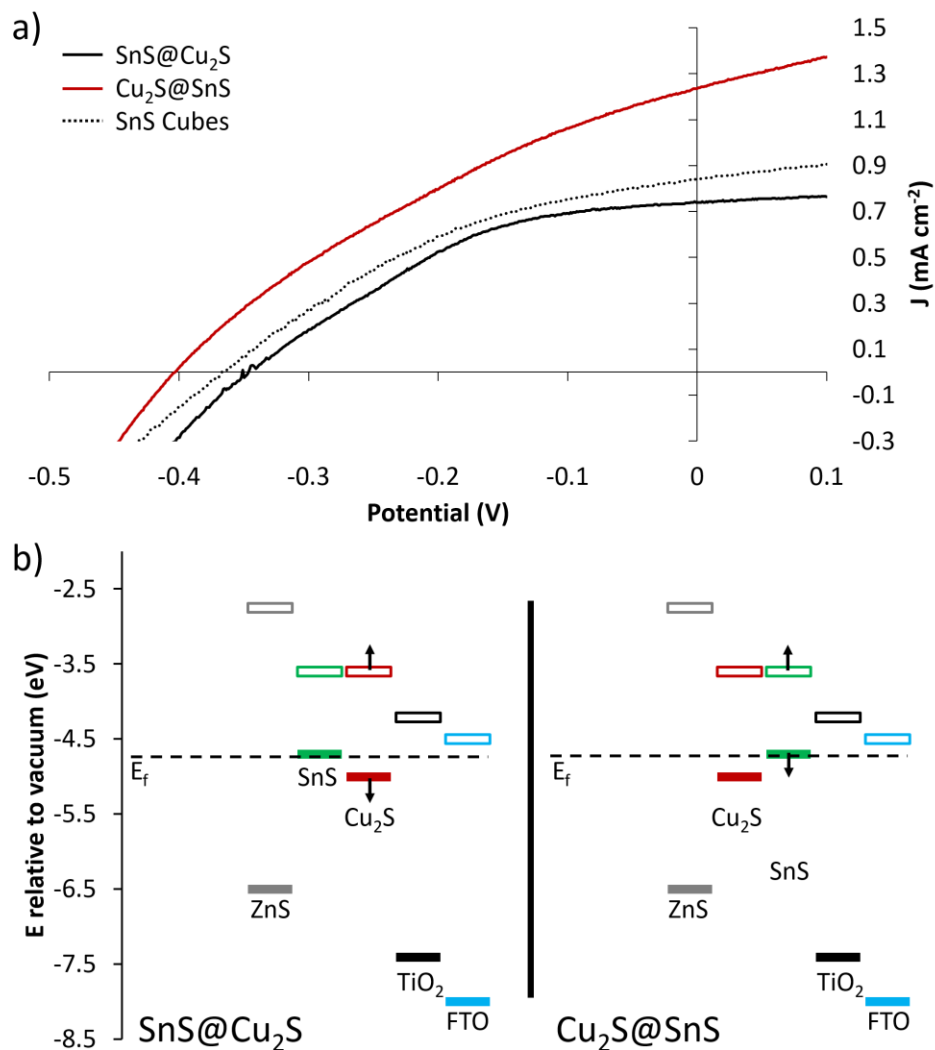
Figure 6. a) J-V curve of devices prepared using SnS@Cu₂S (black), Cu₂S@SnS (red), and SnS (black dashed) nanoparticles under 1 Sun illumination (AM 1.5). b) band alignment of total device using bulk values of CB (red) and VB (blue) and polysulfide reduction potential (orange). Small black arrows show expected direction of shell band movement due to quantum confinement effects. Green arrows show direction of photoexcited electron transfer.

Table 1. Solar Cell Characteristics.

Photoabsorber	V_{oc} (mV)	J_{sc} (mA cm^{-2})	FF	η (%)
SnS@Cu₂S	346	0.74	0.41	0.105
Cu₂S@SnS	403	1.24	0.33	0.164
SnS cubes	367	0.84	0.39	0.119

Considering the type II SnS-Cu$_2$S band alignment (Figure 6b) with approximately equal conduction band (CB) positions, either core@shell configuration should allow for the flow of excited electrons (e$^-$) from higher CBs to lower. However, devices employing Cu$_2$S@SnS nanocubes are expected to have increased J_{sc} compared to SnS@Cu$_2$S, as the valence band (VB) alignment allows for the electron hole (h$^+$) left in the VB to be removed from the core by the electrolyte. From Figure 6b, it is expected that SnS@Cu$_2$S particles will exhibit higher resistance to conduction than SnS because the h$^+$ experience a larger energy barrier due to the Cu$_2$S shell. Slight modulation of the shell CB is expected due to quantum confinement effects, as the 2-3 nm shells are smaller than the Bohr exciton radius of both SnS (7 nm)[52] and Cu$_2$S (5 nm).[53] A higher shell CB position likely limits the J_{sc} and FF of these devices.

Increased η of Cu$_2$S@SnS $vs.$ SnS@Cu$_2$S is observed, even with lower average loading: Cu$_2$S@SnS = 2.9 µmol cm^{-2} $vs.$ SnS@Cu$_2$S = 8.3 µmol cm^{-2}. However, an unexpected deficiency in the Cu$_2$S@SnS particles is the fill factor (FF), which indicates higher resistive response overall. Since these nanoparticles are much larger than the Cu$_2$S Bohr exciton radius of 5 nm, it is expected that bulk-like transport phenomena contribute to a decrease in intra-particle conductance.[53] Further, if there are defects present as Cu$_x$S (x = 1.8 - 2), the synthesized particles can give rise to a plurality of phases with associated band-bending at interfaces and changing absorption coefficients, which tend to increase the sheet resistance of the material. This correspondingly increases J$_{sc}$,[54] but causes the cell to respond to applied potential more like a resistor than an ideal photodiode.[55] This is a demonstration of Ohm's law, in which an ideal resistor has a linear I-V relationship and a FF of 0.25, in contrast to an ideal photodiode having a FF of 1.

Conclusions

We have observed a chemical switching of core and shell materials in the cation exchange of SnS nanocubes with the foreign ion Cu^+. On addition of Cu^+ in to the crude solution of SnS nanocubes, Cu^+ only exchanges a few monolayers of the surface Sn^{2+} at relatively lower temperature, producing $SnS@Cu_2S$ core@shell nanocubes. However at an elevated temperature, Cu^+ acquires additional potential and proceeds extremely fast to occupy the core of the nanocubes, concomitantly moving the core SnS out to become a few-monolayer-thick shell and producing $Cu_2S@SnS$ core-shell nanocubes. The transformation process of $SnS \rightarrow SnS@Cu_2S \rightarrow Cu_2S@SnS$ can be rationalized as a unique chemical exertion by the diffusion couple, and is a product of the specific reaction conditions. Further, the comparative photovoltaics studies reveal that the $Cu_2S@SnS$ is overall a better photovoltaic material than the pristine SnS and $SnS@Cu_2S$ nanocubes, but it demonstrates resistive behavior.

References

(1)   Alivisatos, A. P.; Peng, X.; Manna, L.; Yang, W.; Wickham, J.; Scher, E.; Kadavanich, A. Shape Control of CdSe Nanocrystals. *Nature* **2000**, *404* (6773), 59–61.

(2)   Joo, J.; Na, H. Bin; Yu, T.; Yu, J. H.; Kim, Y. W.; Wu, F.; Zhang, J. Z.; Hyeon, T. Generalized and Facile Synthesis of Semiconducting Metal Sulfide Nanocrystals. *J. Am. Chem. Soc.* **2003**, *125* (36), 11100–11105.

(3)   Kruszynska, M.; Borchert, H.; Bachmatiuk, A.; Rümmeli, M. H.; Büchner, B.; Parisi, J.; Kolny-Olesiak, J. Size and Shape Control of Colloidal Copper(I) Sulfide Nanorods. *ACS Nano* **2012**, *6* (7), 5889–5896.

(4)   Hines, M. A.; Scholes, G. D. Colloidal PbS Nanocrystals with Size-Tunable Near-Infrared Emission: Observation of Post-Synthesis Self-Narrowing of the Particle Size Distribution. *Adv. Mater.* **2003**, *15*

(21), 1844–1849.

(5) Talapin, D. V.; Nelson, J. H.; Shevchenko, E. V.; Aloni, S.; Sadtler, B.; Alivisatos, A. P. Seeded Growth of Highly Luminescent CdSe/CdS Nanoheterostructures with Rod and Tetrapod Morphologies. *Nano Lett.* **2007**, *7* (10), 2951–2959.

(6) Leach, A. D. P.; Mast, L. G.; Hernández-Pagán, E. A.; Macdonald, J. E. Phase Dependent Visible to near-Infrared Photoluminescence of $CuInS_2$ Nanocrystals. *J. Mater. Chem. C* **2015**, *3* (14), 3258–3265.

(7) Sarkar, S.; Guria, A. K.; Patra, B. K.; Pradhan, N. Chemical Sealing of Nanotubes: A Case Study on Sb_2S_3. *Angew. Chemie* **2014**, *126* (46), 12774–12778.

(8) Miszta, K.; Dorfs, D.; Genovese, A.; Kim, M. R.; Manna, L. Cation Exchange Reactions in Colloidal Branched Nanocrystals. *ACS Nano* **2011**, *5* (9), 7176–7183.

(9) Miszta, K.; Brescia, R.; Prato, M.; Bertoni, G.; Marras, S.; Xie, Y.; Ghosh, S.; Kim, M. R.; Manna, L. Hollow and Concave Nanoparticles via Preferential Oxidation of the Core in Colloidal Core/Shell Nanocrystals. *J. Am. Chem. Soc.* **2014**, *136* (25), 9061–9069.

(10) Zhang, B.; Jung, Y.; Chung, H.-S.; Vugt, L. Van; Agarwal, R. Nanowire Transformation by Size-Dependent Cation Exchange Reactions. *Nano Lett.* **2010**, *10* (1), 149–155.

(11) Li, H.; Brescia, R.; Krahne, R.; Bertoni, G.; Alcocer, M. J. P.; D'Andrea, C.; Scotognella, F.; Tassone, F.; Zanella, M.; De Giorgi, M.; Manna, L. Blue-UV-Emitting ZnSe(Dot)/ZnS(Rod) Core/Shell Nanocrystals Prepared from CdSe/CdS Nanocrystals by Sequential Cation Exchange. *ACS Nano* **2012**, *6* (2), 1637–1647.

(12) Jain, P. K.; Amirav, L.; Aloni, S.; Alivisatos, A. P. Nanoheterostructure Cation Exchange: Anionic Framework Conservation. *J. Am. Chem. Soc.* **2010**, *132* (29), 9997–9999.

(13) Beberwyck, B. J.; Surendranath, Y.; Alivisatos, A. P. Cation Exchange: A Versatile Tool for Nanomaterials Synthesis. *J. Phys. Chem. C* **2013**, *117* (39), 19759–19770.

(14) Son, D. H.; Hughes, S. M.; Yin, Y.; Paul Alivisatos, A. Cation Exchange Reactions in Ionic Nanocrystals. *Science* **2004**, *306* (5698), 1009–1012.

(15) Robinson, R. D.; Sadtler, B.; Demchenko, D. O.; Erdonmez, C. K.; Wang, L.-W.; Alivisatos, A. P. Spontaneous Superlattice Formation in Nanorods through Partial Cation Exchange. *Science* **2007**, *317* (5836), 355–358.

(16)   Choi, D.; Pyo, J.-Y.; Kim, Y.; Jang, D.-J. Facile Synthesis of Composition-Gradient $Cd_{1-x}Zn_xS$ Quantum Dots by Cation Exchange for Controlled Optical Properties. *J. Mater. Chem. C* **2015**, *3* (14), 3286–3293.

(17)   Ramasamy, P.; Kim, M.; Ra, H.-S.; Kim, J.; Lee, J.-S. Bandgap Tunable Colloidal Cu-Based Ternary and Quaternary Chalcogenide Nanosheets via Partial Cation Exchange. *Nanoscale* **2016**, *8* (15), 7906–7913.

(18)   Kang, M. S.; Sahu, A.; Frisbie, C. D.; Norris, D. J. Influence of Silver Doping on Electron Transport in Thin Films of PbSe Nanocrystals. *Adv. Mater.* **2013**, *25* (5), 725–731.

(19)   Sarkar, S.; Karan, N. S.; Pradhan, N. Ultrasmall Color-Tunable Copper-Doped Ternary Semiconductor Nanocrystal Emitters. *Angew. Chemie Int. Ed.* **2011**, *50* (27), 6065–6069.

(20)   Jain, P. K.; Beberwyck, B. J.; Fong, L.-K.; Polking, M. J.; Alivisatos, A. P. Highly Luminescent Nanocrystals From Removal of Impurity Atoms Residual From Ion-Exchange Synthesis. *Angew. Chemie Int. Ed.* **2012**, *51* (10), 2387–2390.

(21)   Li, H.; Zanella, M.; Genovese, A.; Povia, M.; Falqui, A.; Giannini, C.; Manna, L. Sequential Cation Exchange in Nanocrystals: Preservation of Crystal Phase and Formation of Metastable Phases. *Nano Lett.* **2011**, *11* (11), 4964–4970.

(22)   Rivest, J. B.; Jain, P. K. Cation Exchange on the Nanoscale: An Emerging Technique for New Material Synthesis, Device Fabrication, and Chemical Sensing. *Chem. Soc. Rev.* **2013**, *42* (1), 89–96.

(23)   Miszta, K.; Gariano, G.; Brescia, R.; Marras, S.; De Donato, F.; Ghosh, S.; De Trizio, L.; Manna, L. Selective Cation Exchange in the Core Region of $Cu_{2-X}Se/Cu_{2-x}S$ Core/Shell Nanocrystals. *J. Am. Chem. Soc.* **2015**, *137* (38), 12195–12198.

(24)   Acharya, S.; Pradhan, N. Insertion/Ejection of Dopant Ions in Composition Tunable Semiconductor Nanocrystals. *J. Phys. Chem. C* **2011**, *115* (40), 19513–19519.

(25)   Shao, H.; Wang, C.; Xu, S.; Jiang, Y.; Shao, Y.; Bo, F.; Wang, Z.; Cui, Y. Hydrazine-Promoted Sequential Cation Exchange: A Novel Synthesis Method for Doped Ternary Semiconductor Nanocrystals with Tunable Emission. *Nanotechnology* **2014**, *25* (2), 25603.

(26)   Mao, B.; Chuang, C. H.; Lu, F.; Sang, L.; Zhu, J.; Burda, C. Study of the Partial Ag-to-Zn Cation Exchange in $AgInS_2$/ZnS Nanocrystals. *J. Phys. Chem. C* **2013**, *117* (1), 648–656.

(27)   Lesnyak, V.; George, C.; Genovese, A.; Prato, M.; Casu, A.; Ayyappan, S.; Scarpellini, A.; Manna, L. Alloyed Copper Chalcogenide Nanoplatelets *via* Partial Cation Exchange Reactions. *ACS Nano* **2014**, *8*

(8), 8407–8418.

(28)   Tu, R.; Xie, Y.; Bertoni, G.; Lak, A.; Gaspari, R.; Rapallo, A.; Cavalli, A.; Trizio, L. De; Manna, L. Influence of the Ion Coordination Number on Cation Exchange Reactions with Copper Telluride Nanocrystals. *J. Am. Chem. Soc.* **2016**, *138* (22), 7082–7090.

(29)   Casavola, M.; van Huis, M. A.; Bals, S.; Lambert, K.; Hens, Z.; Vanmaekelbergh, D. Anisotropic Cation Exchange in PbSe/CdSe Core/Shell Nanocrystals of Different Geometry. *Chem. Mater.* **2012**, *24* (2), 294–302.

(30)   Lambert, K.; Geyter, B. De; Moreels, I.; Hens, Z. PbTe|CdTe Core|Shell Particles by Cation Exchange, a HR-TEM Study. *Chem. Mater.* **2009**, *21* (5), 778–780.

(31)   Zhang, J.; Chernomordik, B. D.; Crisp, R. W.; Kroupa, D. M.; Luther, J. M.; Miller, E. M.; Gao, J.; Beard, M. C. Preparation of Cd/Pb Chalcogenide Heterostructured Janus Particles *via* Controllable Cation Exchange. *ACS Nano* **2015**, *9* (7), 7151–7163.

(32)   Wang, X.; Liu, X.; Zhu, D.; Swihart, M. T. Controllable Conversion of Plasmonic $Cu_{2-x}S$ Nanoparticles to Au_2S by Cation Exchange and Electron Beam Induced Transformation of $Cu_{2-x}S$-Au_2S Core/shell Nanostructures. *Nanoscale* **2014**, *6* (15), 8852–8857.

(33)   Hodges, J. M.; Kletetschka, K.; Fenton, J. L.; Read, C. G.; Schaak, R. E. Sequential Anion and Cation Exchange Reactions for Complete Material Transformations of Nanoparticles with Morphological Retention. *Angew. Chemie Int. Ed.* **2015**, *54* (30), 8669–8672.

(34)   De Trizio, L.; Manna, L. Forging Colloidal Nanostructures via Cation Exchange Reactions. *Chem. Rev.* **2016**, *116* (18), 10852–10887.

(35)   Gupta, S.; Kershaw, S. V.; Rogach, A. L. 25th Anniversary Article: Ion Exchange in Colloidal Nanocrystals. *Adv. Mater.* **2013**, *25* (48), 6923–6944.

(36)   Sadtler, B.; Demchenko, D. O.; Zheng, H.; Hughes, S. M.; Merkle, M. G.; Dahmen, U.; Wang, L.-W.; Alivisatos, A. P. Selective Facet Reactivity during Cation Exchange in Cadmium Sulfide Nanorods. *J. Am. Chem. Soc.* **2009**, *131* (14), 5285–5293.

(37)   De Trizio, L.; Li, H.; Casu, A.; Genovese, A.; Sathya, A.; Messina, G. C.; Manna, L. Sn Cation Valency Dependence in Cation Exchange Reactions Involving $Cu_{2-x}Se$ Nanocrystals. *J. Am. Chem. Soc.* **2014**, *136* (46), 16277–16284.

(38)   Lesnyak, V.; Brescia, R.; Messina, G. C.; Manna, L. Cu Vacancies Boost Cation Exchange Reactions in Copper Selenide Nanocrystals. *J. Am. Chem. Soc.* **2015**, *137* (29), 9315–9323.

(39)   Ha, D.-H.; Caldwell, A. H.; Ward, M. J.; Honrao, S.; Mathew, K.; Hovden, R.; Koker, M. K. A.; Muller, D. A.; Hennig, R. G.; Robinson, R. D. Solid–Solid Phase Transformations Induced through Cation Exchange and Strain in 2D Heterostructured Copper Sulfide Nanocrystals. *Nano Lett.* **2014**, *14* (12), 7090–7099.

(40)   Mu, L.; Wang, F.; Sadtler, B.; Loomis, R. A.; Buhro, W. E. Influence of the Nanoscale Kirkendall Effect on the Morphology of Copper Indium Disulfide Nanoplatelets Synthesized by Ion Exchange. *ACS Nano* **2015**, *9* (7), 7419–7428.

(41)   Lee, S.; Baek, S.; Park, J. P.; Park, J. H.; Hwang, D. Y.; Kwak, S. K.; Kim, S. W. Transformation from $Cu_{2-x}S$ Nanodisks to $Cu_{2-x}S@CuInS_2$ Heteronanodisks via Cation Exchange. *Chem. Mater.* **2016**, *28* (10), 3337–3344.

(42)   Yu, Y.; Cao, C. Y.; Chen, Z.; Liu, H.; Li, P.; Dou, Z. F.; Song, W. G. Au Nanoparticles Embedded into the Inner Wall of TiO_2 Hollow Spheres as a Nanoreactor with Superb Thermal Stability. *Chem. Commun.* **2013**, *49* (30), 3116–3118.

(43)   Zhang, Y.; Ang, C. Y.; Li, M.; Tan, S. Y.; Qu, Q.; Luo, Z.; Zhao, Y. Polymer-Coated Hollow Mesoporous Silica Nanoparticles for Triple-Responsive Drug Delivery. *ACS Appl. Mater. Interfaces* **2015**, *7* (32), 18179–18187.

(44)   Deng, D.; Lee, J. Y. Hollow Core–Shell Mesospheres of Crystalline SnO_2 Nanoparticle Aggregates for High Capacity Li + Ion Storage. *Chem. Mater.* **2008**, *20* (5), 1841–1846.

(45)   Xie, Q.; Zhao, Y.; Guo, H.; Lu, A.; Zhang, X.; Wang, L.; Chen, M. S.; Peng, D. L. Facile Preparation of Well-Dispersed CeO_2-ZnO Composite Hollow Microspheres with Enhanced Catalytic Activity for CO Oxidation. *ACS Appl. Mater. Interfaces* **2014**, *6* (1), 421–428.

(46)   Sun, L.; Han, X.; Liu, K.; Yin, S.; Chen, Q.; Kuang, Q.; Han, X.; Xie, Z.; Wang, C. Template-Free Construction of Hollow α-Fe_2O_3 Hexagonal Nanocolumn Particles with an Exposed Special Surface for Advanced Gas Sensing Properties. *Nanoscale* **2015**, *7* (21), 9416–9420.

(47)   Finn, S. T.; Macdonald, J. E. Petaled Molybdenum Disulfide Surfaces: Facile Synthesis of a Superior Cathode for QDSSCs. *Adv. Energy Mater.* **2014**, *4*.

(48) Finn, S. T.; Macdonald, J. E. Contact and Support Considerations in the Hydrogen Evolution Reaction Activity of Petaled MoS$_2$ Electrodes. *ACS Appl. Mater. Interfaces* **2016**, *8* (38), 25185–25192.

(49) Patra, B. K.; Sarkar, S.; Guria, A. K.; Pradhan, N. Monodisperse SnS Nanocrystals: In Just 5 Seconds. *J. Phys. Chem. Lett.* **2013**, *4* (22), 3929–3934.

(50) Rabkin, A.; Samuha, S.; Abutbul, R. E.; Ezersky, V.; Meshi, L.; Golan, Y. New Nanocrystalline Materials: A Previously Unknown Simple Cubic Phase in the SnS Binary System. *Nano Lett.* **2015**, *15* (3), 2174–2179.

(51) Abutbul, Rg. E.; Segev, E.; Zeiri, L.; Ezersky, V.; Makov, G.; Golan, Y. Synthesis and Properties of Nanocrystalline π-SnS – a New Cubic Phase of Tin Sulphide. *RSC Adv.* **2016**, *6* (7), 5848–5855.

(52) Huang, P.-C.; Huang, J.-L.; Wang, S.-C.; Shaikh, M. O.; Lin, C.-Y. Photoelectrochemical Properties of Orthorhombic and Metastable Phase SnS Nanocrystals Synthesized by a Facile Colloidal Method. *Thin Solid Films* **2015**, *596*, 135–139.

(53) Bekenstein, Y.; Elimelech, O.; Vinokurov, K.; Millo, O.; Banin, U. Charge Transport in Cu$_2$S Nanocrystals Arrays: Effects of Crystallite Size and Ligand Length. *Zeitschrift für Phys. Chemie* **2015**, *229* (1–2), 179–190.

(54) Rothwarf, a.; Windawi, H. The Controlling Influence of the Cu$_2$S Optical Absorption Coefficient on the Short-Circuit Currents of Cu$_2$S/CdS Solar Cells. *IEEE Trans. Electron. Devices* **1981**, *1* (1), 64–69.

(55) Ashok, S.; Pande, K. P. Photovoltaic Measurements. *Sol. Cells* **1985**, *14*, 61–81.

Conclusion

Scheme 1. Flowchart outlining sequential steps in development of an idea into a technology.

Summary of Completed Work and Future Directions

Throughout the course of this dissertation work, my approach has always been to minimize steps, cost, and harshness of synthesis conditions (*e.g.*, by using low temperature, ambient air, etc.) for the sake of facile incorporation into end products. In the timeline from idea inception to final application (**Scheme 1**), I firmly believe that simplifying experiments on the research side (toward the blue) only makes for easier translation to the manufacturing side. After all, the aim of my work is to benefit mankind by providing affordable, alternative solutions to the global energy crisis.

First, I have adapted a hydrothermal synthesis of flowerlike MoS_2 spheres[1] into a uniform film of MoS_2 petals grown from a planar Mo foil.[2] Using a stainless-steel acid digestion vessel, only three ingredients are required: Mo foil, thiourea, and water. The simplicity and frugality of this synthesis are not to be understated, as they smooth the path for scale-up of this and potentially myriad other materials into larger devices. Also, I developed a method for growing P. MoS_2 from a non-native, Au substrate following Mo electrodeposition while maintaining its unique morphology and chemistry. Although Au and Mo are not the most earth-abundant

materials, Mo is currently very inexpensive, and the synthetic principles of this work may be applied to more earth-abundant materials in the future. Next, I comprehensively characterized P. MoS_2 using modern as well as time-tested techniques and technologies, including Raman spectroscopy, Stylus Profilometry, SEM, EDS, FIB, TEM, XPS, and XRD.

I have evaluated the use of P. MoS_2 in three different alternative energy technologies: QDSSCs, HER, and LIBs. Simply learning how to assemble a QDSSC with $\eta \geq 1\%$ took 1.5 years, which is a testament to the state of the field *vis-à-vis* literature reporting practices. Ultimately, device testing may be best left to engineers and corporate labs, but it is very useful for chemists to be able to test their novel materials in model devices. Additionally, because I took the time to assemble and test devices, I learned a great deal about the role that each component plays. Also, I learned about the need to develop devices that minimize the number of interfaces and materials, as each new material adds at least one more interface for increasing resistance, lattice strain, degree of consideration for compatibility, etc. to the device.

The HER studies escorted my project into the field of electrocatalysis proper. Most researchers who investigate MoS_2 do so for final application to HER. We showed that P. MoS_2 is a good HER catalyst, although it certainly is not the best, especially in comparison to NiP, NiMo, etc. catalysts by Lewis et al.[3] However, considering the cost of the alternative (Pt), MoS_2 is still a viable HER material, as the best MoS_2 HER catalysts exhibit η to 10 mA cm^{-2} of 110 mV *vs.* RHE.[4] This study also illuminated other challenges in the design of self-supported electrode materials. It seems that materials produced from aqueous, low-cost syntheses can concomitantly produce tradeoffs such as complicated intermediate layers and unforeseen catalyst-support interactions. As was discovered, a rough support (Mo foil) which produces MoS_2 catalytic sites with lower intrinsic activity (TOF) can be compensated for by providing a higher geometric density of active sites, compared to a flat support (*e.g.* Au) which provides catalytic sites with intrinsically higher HER activity.

In contrast to the HER activity, I found that the intermediate MoS_xO_y layer which forms naturally from the hydrothermal process is, in fact, detrimental to performance of P. MoS_2 in LIBs because the amorphous

oxysulfides cycle between Mo-MoO_3. It is well known at this point that if any S is introduced in the device, it forms Li_2S upon discharge, S_n^{2-} upon charge, then cycles between the two. Therefore, irrespective of the design of the nanostructured metal sulfide (except for exposing edge vs. terrace sites in layered TMDCs), it only serves as a S source and structural support for S_n^{2-} cycling. However, the petaled architecture may be beneficial in this case because it exposes the MoS_2 basal plane, providing access to the van der Waals gaps while allowing horizontal swelling during intercalation. Also, in regards to designing cathodes for Li-S batteries, much attention has been paid to developing electrodes which interact strongly with S_n^{2-} species, preventing dissolution and migration to the anode.[5] Future P. MoS_2-based LIB electrodes could benefit from growth on an alternate substrate which prevents formation of the intermediate MoS_xO_y layer, such as the P. MoS_2/Au electrodes demonstrated in Chapter IV. Alternatively, the P. MoS_2 electrode could be modified with a conformal coating that preserves the petal morphology and S, but allows Li^+ to move in and out during discharge and charge, respectively.

Handling collaborations well will be increasingly important as grant funding becomes more scarce and therefore more selective. In this climate of government frugality towards research spending, collaborations will become necessary for all researchers to not only have a share in the funds, but address global concerns in an interdisciplinary way.

Finally, core@shell nanocubes were synthesized by Suresh Sarkar, and I deposited them onto TiO_2 anodes *via* electrophoretic deposition, then tested their performance as photoabsorbers in QDSSCs. We found that the interesting band alignment strongly affected the photovoltaic properties of the device. Of course, P. MoS_2 was used once again as the counter electrode for S_n^{2-} reduction. We showed a proof-of-concept measurement of the deposition and overall device characteristics. It would have been ideal to obtain a functioning device over 1% power conversion efficiency, but that was not the goal of the paper.

Outlook and Broader Impacts

This specialized field of catalytic nanomaterials sits between nanochemistry synthesis and materials engineering. I foresee the field continuing to address energy-related problems by working together effectively. Thankfully, HER has been well-optimized for solar water splitting and fuel cells, but now our community needs to develop acid-stable oxygen-evolution reaction (OER) catalysts,[6] as well as catalysts for the reverse reactions – hydrogen oxidation reaction and oxygen reduction reaction (HOR and ORR, respectively) – used in fuel cells.[7,8] In general, it is still very difficult to find highly active Pt-free catalysts, so much so that a large body of research in this field is directed toward simply minimizing Pt content instead of removing it entirely.[9] Photocatalysis plays a role here as well as in SCs and – although it is absolutely necessary for solar energy conversion – direct solar-to-water-splitting photocatalytic systems suffer from low current densities and efficiencies.[10–12] Perovskite materials have certainly made a large impact in the field of SCs as thin films,[13] providing evidence that focusing solely on the "nano" regime may not always provide the best solutions to some of these larger-scale energy problems.

Relative to the broad discipline of chemistry, I have incorporated study of chemical interfacial processes between support and intermediate layer, intermediate layer and surface (crystallography, epitaxy, impedance) and those between surface and liquid (heterogeneous catalysis: S_n^{2-} reduction, HER, electrochemistry, intercalation). This work affects chemistry principally by simultaneously focusing on larger- and smaller-scale interactions and combining chemistry with engineering. I am not the only person working in this interdisciplinary melting pot of chemistry, physics, and engineering to solve global problems, and I am not even the only one at Vanderbilt University! Chemists like myself will bring the intuition of chemistry and others will bring the precise, physical relations and larger-scale, real-world considerations to this work. It requires the whole of STEM to solve the world's energy crisis.

For science – which is the increasing of knowledge by asking and answering questions through observation, hypothesis, experiment, revision, and theory development – this work has incorporated sustainable practices at even the smallest steps. We have asked and attempted to answer questions which deal with the nature of things, and are fundamental in and of themselves but also serve to develop new technologies, in keeping with Aristotle's pursuit of the highest good for all.[14]

At minimum, this work has impacted society by increasing knowledge about the problem. Three scientific papers, a patent, and a dissertation have been produced, which serve to aid other researchers working on this problem as well as equip companies with chemical technologies that can be scaled up and incorporated into devices. Devices produced can hopefully be sold inexpensively to individuals, organizations, and governments for the sake of providing clean energy to all, improving their quality of life and reducing the burden of burning fossil fuels on our natural world.

References

(1)   Huang, W.; Xu, Z.; Liu, R.; Ye, X.; Zheng, Y. Tungstenic Acid Induced Assembly of Hierarchical Flower-like MoS_2 Spheres. *Mater. Res. Bull.* **2008**, *43* (10), 2799–2805.

(2)   Finn, S. T.; Macdonald, J. E. Petaled Molybdenum Disulfide Surfaces: Facile Synthesis of a Superior Cathode for QDSSCs. *Adv. Energy Mater.* **2014**, *4*.

(3)   Saadi, F. H.; Carim, A. I.; Verlage, E.; Hemminger, J. C.; Lewis, N. S.; Soriaga, M. P. CoP as an Acid-Stable Active Electrocatalyst for the Hydrogen-Evolution Reaction: Electrochemical Synthesis, Interfacial Characterization and Performance Evaluation. *J. Phys. Chem. C* **2014**, *118* (50), 29294–29300.

(4)   Benck, J. D.; Hellstern, T. R.; Kibsgaard, J.; Chakthranont, P.; Jaramillo, T. F. Catalyzing the Hydrogen Evolution Reaction (HER) with Molybdenum Sulfide Nanomaterials. *ACS Catal.* **2014**, *4*, 3957–3971.

(5)   Li, Z.; Huang, Y.; Yuan, L.; Hao, Z.; Huang, Y. Status and Prospects in Sulfur-Carbon Composites as Cathode Materials for Rechargeable Lithium-Sulfur Batteries. *Carbon N. Y.* **2015**, *92*, 41–63.

(6)   Jin, J.; Walczak, K.; Singh, M. R.; Karp, C.; Lewis, N. S.; Xiang, C. An Experimental and Modeling/simulation-Based Evaluation of the Efficiency and Operational Performance Characteristics of an Integrated, Membrane-Free, Neutral pH Solar-Driven Water-Splitting System. *Energy Environ. Sci. Energy Environ. Sci* **2014**, *7* (7), 3371–3371.

(7)   Arico. A. S Scorosati. B, Tarascon. J. M, Schalkwijk. W. V, B. P. Nanostructured Materials for Advanced Energy Conversion and Storage Devices. *Nat. Mater.* **2005**, *4* (5), 366–377.

(8)   Steele, B. C.; Heinzel, A. Materials for Fuel-Cell Technologies. *Nature* **2001**, *414* (November), 345–352.

(9)   Wang, Y.-J.; Fang, B.; Li, H.; Bi, X. T.; Wang, H. Progress in Modified Carbon Support Materials for Pt and Pt-Alloy Cathode Catalysts in Polymer Electrolyte Membrane Fuel Cells. *Prog. Mater. Sci.* **2016**, *82*, 445–498.

(10)   McCool, N. S.; Swierk, J. R.; Nemes, C. T.; Schmuttenmaer, C. A.; Mallouk, T. E. Dynamics of Electron Injection in SnO_2/TiO_2 Core/Shell Electrodes for Water-Splitting Dye-Sensitized Photoelectrochemical Cells. *J. Phys. Chem. Lett.* **2016**, *7*, 2930–2934.

(11)   Sivula, K.; Le Formal, F.; Grätzel, M. Solar Water Splitting: Progress Using Hematite (α-Fe_2O_3) Photoelectrodes. *ChemSusChem* **2011**, *4* (4), 432–449.

(12)   Xiang, C.; Weber, A. Z.; Ardo, S.; Berger, A.; Chen, Y.; Coridan, R.; Fountaine, K. T.; Haussener, S.; Hu, S.; Liu, R.; Lewis, N. S.; Modestino, M. A.; Shaner, M. M.; Singh, M. R.; Stevens, J. C.; Sun, K.; Walczak, K. Modeling, Simulation, and Implementation of Solar-Driven Water-Splitting Devices.

Angew. Chemie Int. Ed. **2016**, *55* (42), 12974–12988.

(13)   Stoumpos, C. C.; Kanatzidis, M. G. The Renaissance of Halide Perovskites and Their Evolution as Emerging Semiconductors. *Acc. Chem. Res.* **2015**, *48* (10), 2791–2802.

(14)   Kraut, R. Aristotle's Ethics. *The Stanford Encyclopedia of Philosophy*; 2016.

Additional SEM Images

Figure A1. Additional SEM images of petaled MoS_2 electrodes reveal a) - c) consistent film morphology amongst multiple preparations and d) uniform morphology across a larger area of the electrode (compare with Figure 3a in Chapter I text).

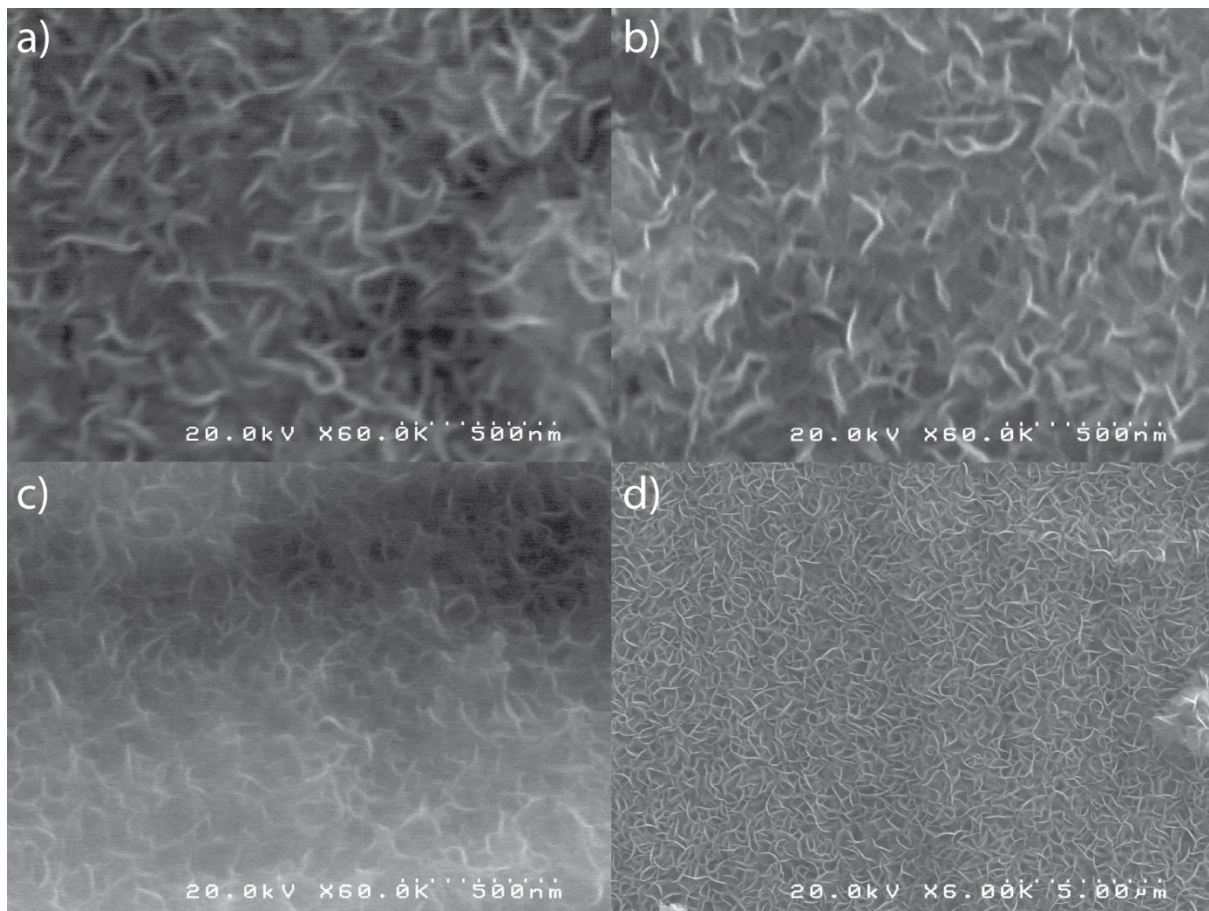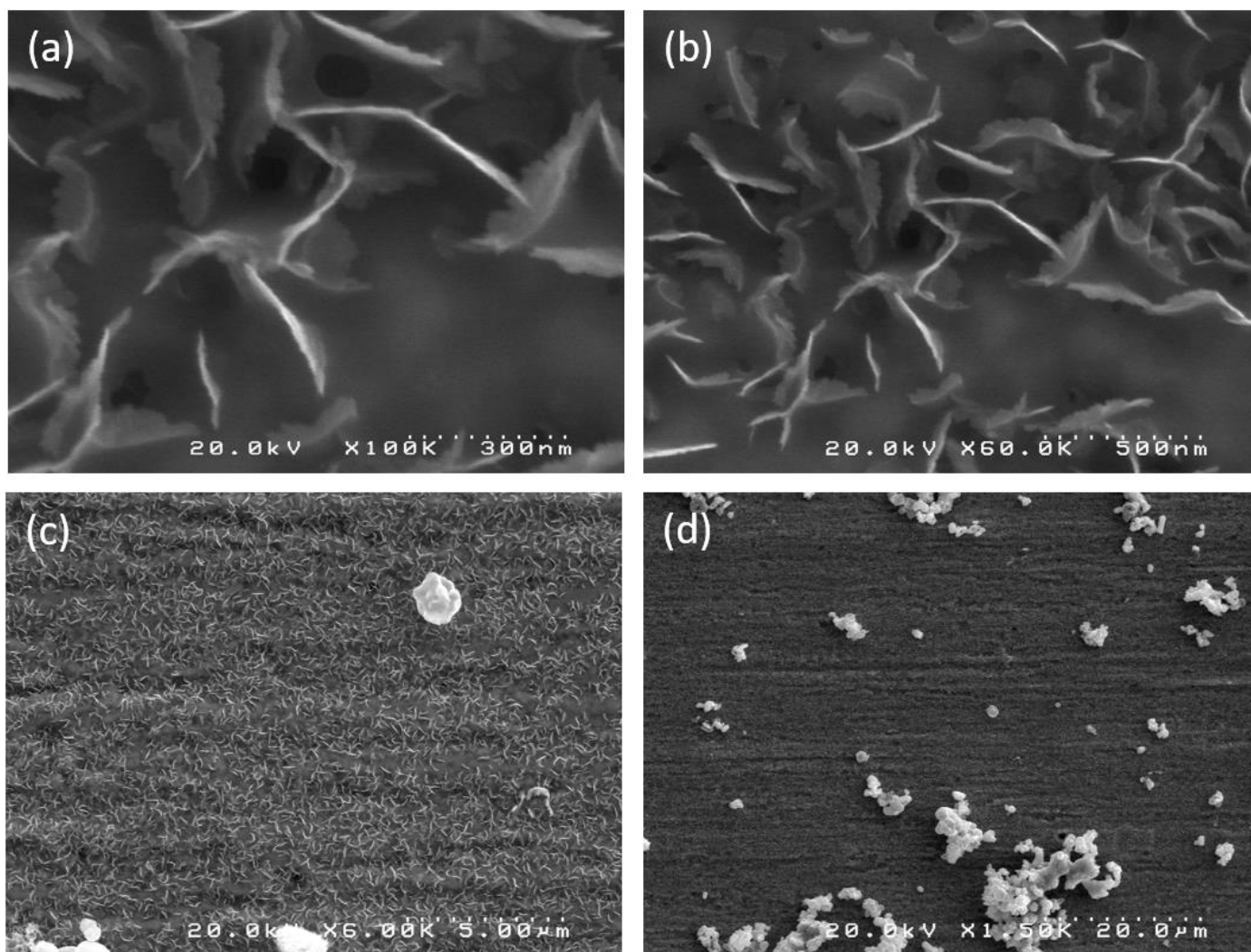**Figure A2.** Additional SEM images of petaled MoSe$_2$ electrodes reveal (a) – (c) consistent film morphology amongst multiple preparations. Clumps in (c, d) are Se particles.

Shane Thomas Finn

6501 Harding Pike Apt.L55
Nashville, TN 37205
Cell: (239) 290-9675
Office: (615) 343-2658
shane.t.finn@Vanderbilt.Edu

Curriculum Vitae

Education

05/2017   **Doctor of Philosophy, Chemistry**
Vanderbilt University, Nashville, TN

05/2011   **Bachelor of Arts, Chemistry**
Florida Gulf Coast University, Fort Myers, FL
Minors: Interdisciplinary Studies

Work and Research Experience

06/2011 – Present   **Ph.D. Student**
Vanderbilt University
Department of Chemistry
Advisor: Janet E. Macdonald, Ph.D.

- Developed an inexpensive, one-step, three-ingredient, hydrothermal synthesis for the uniform growth of a nanostructured semiconductor, MoS_2, from a Mo foil: "petaled MoS_2."
- Optimized petaled MoS_2 to achieve 6x higher current density for polysulfide reduction *vs.* common electrode materials, resulting in 42% efficiency increase for quantum dot sensitized solar cells.
- Identified and characterized intermediate layer of petaled MoS_2 using FIB, cross-sectional SEM-EDS, and XPS. Further, performed *ex situ* analysis of petaled MoS_2 used in lithium ion batteries with glancing-angle XRD to identify primary redox reactions occurring during cycling.
- Adapted synthesis to enable petaled MoS_2 growth from alternate substrates without intermediate MoS_xO_y layer via electrodeposition of Mo, followed by hydrothermal reaction. This resulted in 4x improved exchange current for HER.

Teaching Fellow

01/2013 – Present	Vanderbilt University Department of Chemistry • Teaching Advanced Integrated Laboratory for seniors in the Chemistry program. First semester: preparing and giving lectures on a higher-level synthetic inorganic chemistry project with in-depth analytical methods. Second semester: guiding students in carrying out individual research projects, preparing them for autonomous research beyond undergraduate studies.
08/2011 – 07/2013	**Teaching Assistant** Vanderbilt University Department of Chemistry • Teaching General Chemistry Lab which includes teaching basic chemistry concepts and experimental techniques, assigning and grading work, overall emphasizing working knowledge of chemistry and understanding experimental undertakings.
06/2011-12/2011	**Rotation Student** Vanderbilt University Department of Chemistry • Rotation Advisor #3: Sandra J. Rosenthal, Ph.D. Shadowed various graduate students, observing the synthesis of CdSe quantum dots, electrochemical testing of new nanoparticles, and construction and testing of solar devices. • Rotation Advisor #2: Janet E. Macdonald, Ph.D. Aided in setting lab up to run experiments. Synthesized and characterized Fe and FePt nanoparticles. • Rotation Advisor #1: David E. Cliffel, Ph.D. Investigated pH dependence of Langmuir-Blodgett deposition and electrochemical characterization of Photosystem I molecules onto gold electrodes for use in photoelectrochemical cells.
12/2009 – 05/2011	**Student Research Assistant** Florida Gulf Coast University Department of Chemistry and Mathematics Principal Investigator: Jose Barreto, Ph.D. • Developed TiO_2-based photocatalysts used in model toxin destruction and chemical sensors; characterized compounds using Raman spectroscopy. • Developed screening technique which utilizes an airbrush to coat TiO_2, then model toxin(s), onto a glass substrate for facile photocatalytic experimentation and characterization.

Supplemental Instruction Leader/Walk-in Lab Tutor
Florida Gulf Coast University
Center for Academic Achievement
Director: Lori Smith

05/2009 – 12/2009
- Led tutoring sessions for large groups of students in Algebra, General Chemistry and Organic Chemistry by facilitating discussion, explaining concepts in-depth, and teaching good study habits.

Tutor
Florida Gulf Coast University
Office of Adaptive Services
Director: Cori Bright

05/2009 – 12/2009
- Tutored students with learning disabilities in Chemistry, Algebra, and Physics.

Teaching Assistant
Florida Gulf Coast University
College of Arts and Sciences
Supervisor: David Deiros

01/2009 – 04/2009
- Assisted the instructor in teaching General Chemistry I: helped students with questions on practice problems, graded tests, prepared experiments and demonstrations.

Acquired Research Techniques

- Inorganic Synthesis:
  - Hydrothermal - acid digestion vessel
  - Electrodeposition
  - E-beam/Thermal Vacuum Deposition
  - Solvothermal/Colloidal
  - Successive Ionic Layer Adsorption and Reaction
  - Chemical Bath Deposition
  - Airless techniques using Schlenk line and glovebox
  - Preparation and construction of liquid-junction solar cells
  - Langmuir-Blodgett monolayer deposition and characterization

- Characterization, Analytical:
  - *Ex Situ* Lithium-ion Battery Characterization
  - Scanning Electron Microscopy (SEM)
    - Zeiss Merlin
    - FEI Q650
    - Hitachi S4200
  - Transmission Electron Microscopy (TEM)
    - FEI Tecnai Osiris
    - Philips CM 20
  - Energy Dispersive X-Ray Spectroscopy (EDS, paired with SEM/TEM instruments)

- Oxford INCA & AZTEC
- Bruker Quantax
  o X-Ray Diffraction (XRD)
    - Glancing Angle
    - GSAS/EXPGUI Refinement
  o Electrochemical characterization of electrodes, photoelectrochemical cells and solar cell devices:
    - Cyclic Voltammetry
    - Linear Sweep Voltammetry
    - Chronoamperometry
    - Electrochemical Impedance Spectroscopy
  o X-Ray Photoelectron Spectroscopy (XPS)
    - Fitting of spectra using CasaXPS software and interpreting results
  o Raman spectroscopy
    - Thermo Scientific DXR Raman Microscope
  o Profilometry
    - Bruker Dektak 150
  o UV-Visible and fluorescence spectroscopy
  o Procedure development for evaluating semiconductor materials properties

Publications

Sarkar, S., **Finn, S.** & Macdonald, J. (2016). A hollow $Cu_2S@SnS$ core-shell via $SnS@Cu_2S$ through cation exchange: An observation of Kirkendall effect (in preparation).

Finn, Shane T. & Macdonald, Janet E. (2016). Contact and Support Considerations in the Hydrogen Evolution Reaction Activity of Petaled MoS_2 Electrodes. *Applied Materials & Interfaces, 8* (38), *25185-25192*. DOI: 10.1021/acsami.6b05101

Finn, Shane T. & Macdonald, Janet E. (2014). Petaled Molybdenum Disulfide Surfaces: Facile Synthesis of a Superior Cathode for QDSSCs. *Advanced Energy Materials, 4 (14).* DOI: 10.1002/aenm.201400495

Finn, S.T., Strnad, J. A., Barreto, P. D., Fox, M. E., Torres, J., Sweeney, J. D., & Barreto, J. C. (2011). A screening technique useful for testing the effectiveness of novel 'self-cleaning' photocatalytic surfaces. *Photochemistry and Photobiology*, *87* (5), *1184-1188.* DOI: 10.1111/j.1751-1097.2011.00953.x

Patents
2014: Janet Macdonald and Shane Thomas Finn, Vanderbilt University (Nov. 15, 2016). Nanostructured electrodes, methods of making electrodes, and methods of using electrodes. Appl. No.:14/187,371; Filed: Feb. 24, 2014; Pub. No.: US9496094 B2. (*Granted*)

Awards and Scholarships

Fall 2012	Warren Graduate Fellowship Grant providing service-free pay for one semester
2011-2012	Teaching Assistantship to attend Vanderbilt University
2011	David M. Hercules Fellowship Award for well-qualified, first-year graduate students at Vanderbilt University

2008-2011	Florida Medallion Merit Award scholarship to attend Florida Gulf Coast University
Spring 2010	FGCU Dean's List: 3.5 or better Semester GPA
Fall 2008	FGCU Dean's List: 3.5 or better Semester GPA
Spring and Fall 2008	FGCU President's List: 4.00 Semester GPA
2006-2007	Florida Medallion Merit Award scholarship to attend Florida Gulf Coast University

Meetings and Symposia

2015	Materials Research Society Fall Meeting & Exhibit Seminar: The Sustainable Development of Petaled MoS_2 as a Versatile, Highly Active, and Self-Supported Electrocatalyst
	Gordon Research Conference, Seminar: Nanomaterials for Applications in Energy Technology Poster presented: "Petaled MoS_2: Synthetic Strategies and Challenges in Developing a Versatile Electrocatalyst for Use in Energy Conversion & Storage"
2014	Southeastern Regional Meeting of the American Chemical Society (SERMACS) Presented seminar entitled: "Petaled MoS_2: Investigating the Structure & Improving the Synthesis of a Versatile Electrocatalyst for Use in Energy Conversion & Storage"
	VINSE Summer Nanoseminar Series Presented seminar entitled: "Understanding and Improving Petaled MoS_2 as a Versatile Electrocatalyst"
	TN-SCORE Annual Conference, Nashville, TN Poster Presented: "Nanostructured MoS_2 electrodes for polysulfide reduction" Shane Finn, Aaron Daniel, Janet Macdonald
	ACS National Meeting Seminar presented by Janet Macdonald: "Petaled MoS_2 films as cathodes for polysulfide reduction"
2013	TN-SCORE Annual Conference, Nashville, TN Poster Presented: "Nanostructured MoS_2 electrodes for polysulfide reduction" Shane Finn, Aaron Daniel, Janet Macdonald

2012	Materials Research Society Fall Meeting and Exhibit, Boston, MA Poster Presented: "Nanostructured MoS_2 electrodes for polysulfide reduction" Shane Finn, Aaron Daniel, Janet Macdonald *Nominated for Best Poster Award Southeastern Regional Meeting of the American Chemical Society (SERMACS) Seminar given in my stead by Janet E. Macdonald entitled: "Nanostructured MoS_2 electrodes for polysulfide reduction in QDSSCs" TN-SCORE Annual Conference, Nashville, TN Poster Presented: "Nanostructured MoS_2 electrodes for polysulfide reduction" Shane T. Finn, Janet E. Macdonald Also presented at Nanoday, Vanderbilt Institute for Nanoscale Science and Engineering (VINSE), Nashville, TN
2011	American Chemical Society Florida Annual Meeting and Exposition (FAME), Innisbrook, FL. Poster Presented: "Titanium oxide-mediated photocatalysis of Sudan Red IV using visible light." Shane Thomas Finn, Jonathan Shute, Jorge Torres, James Sweeney, Jessica A. Strnad, Vincent Rosa, Patricia Barreto, Jose C. Barreto. Pittcon Conference and Expo 2011, Atlanta, GA. Poster Presented: "Developing dye bleaching assays for quantifying the photocatalytic production of destructive hydrophobic radicals, oxidants and reductants (ROR): Sudan red (IV), and Nile red dyes encapsulated in micelles and liposomes as molecular targets." Patricia D. Barreto, Jessica A. Strnad, Shane T. Finn, and Jose C. Barreto.
2010	American Chemical Society Florida Annual Meeting and Exposition (FAME), Innisbrook, FL. Posters Presented: "High calcination temperatures (800 °C) enhance the photocatalytic effects of TiO_2 after Si doping." Shane Thomas Finn, Patricia D. Barreto, Megan E. Herscher, Anastasia Kostrubala, Marisa Schreiber, Sergio Ferrante, Jose C. Barreto. "Doping titanium oxide (TiO_2) with metal, or non-metal atoms, can enhance (or disable) photocatalytic mediated

decontamination: Si is one of the most effective enhancing agents." Marisa Schreiber, Patricia D. Barreto, Anastasia Kostrubala, Sergio Ferrante, Megan E. Herscher, Shane T. Finn, Aprile Jordan, Jose C. Barreto.

Volunteering

2013	Volunteered at Adventure Science Center with the Materials Research Society, Vanderbilt University Chapter. Operated an interactive activity for visitors, teaching concepts of self-assembly on the molecular level.
2012	Reviewed a submission to *Young Scientist Journal*, published by Vanderbilt University to recognize the work of High School scientists.
2010	"Girls + Math + Science = Success" Conference, aimed at inspiring 5th grade girls to pursue the fields of math, science, and engineering. I was a host to speaker and author Dr. Ellen Prager.
2009	Tutoring at the Office of Adaptive Services, Florida Gulf Coast University from January to April. I tutored students with learning disabilities in Chemistry, Algebra and Physics.
2005	Volunteering at Summit Church in Rio de Janeiro, Brazil. For one week, I taught basic English and computer skills to children living in slums.